STARS

University of Central Florida
STARS

Electronic Theses and Dissertations, 2004-2019

2013

Mode-division Multiplexed Transmission In Few-mode Fibers

Neng Bai
University of Central Florida

Part of the Electromagnetics and Photonics Commons, and the Optics Commons
Find similar works at: https://stars.library.ucf.edu/etd
University of Central Florida Libraries http://library.ucf.edu

This Doctoral Dissertation (Open Access) is brought to you for free and open access by STARS. It has been accepted for inclusion in Electronic Theses and Dissertations, 2004-2019 by an authorized administrator of STARS. For more information, please contact STARS@ucf.edu.

STARS Citation
Bai, Neng, "Mode-division Multiplexed Transmission In Few-mode Fibers" (2013). *Electronic Theses and Dissertations, 2004-2019*. 2600.
https://stars.library.ucf.edu/etd/2600

MODE-DIVISION MULTIPLEXED TRANSMISSION IN FEW-MODE FIBERS

by

NENG BAI
B.E. Tianjin University, CHINA, 2008
M.S. University of Central Florida, 2013

A dissertation submitted in partial fulfillment of the requirements
for the degree of Doctor of Philosophy in Optics
in the College of Optics and Photonics
at the University of Central Florida
Orlando, Florida

Summer Term
2013

Major Professor: Guifang Li

© 2013 Neng Bai

ABSTRACT

As a promising candidate to break the single-mode fiber capacity limit, mode-division multiplexing (MDM) explores the spatial dimension to increase transmission capacity in fiber-optic communication. Two linear impairments, namely loss and multimode interference, present fundamental challenges to implementing MDM. In this dissertation, techniques to resolve these two issues are presented.

To de-multiplex signals subject to multimode interference in MDM, Multiple-Input-Multiple-Output (MIMO) processing using adaptive frequency-domain equalization (FDE) is proposed and investigated. Both simulations and experiments validate that FDE can reduce the algorithmic complexity significantly in comparison with the conventional time-domain equalization (TDE) while achieving similar performance as TDE. To further improve the performance of FDE, two modifications on traditional FDE algorithm are demonstrated. i) normalized adaptive FDE is applied to increase the convergence speed by 5 times; ii) master-slave carrier recovery is proposed to reduce the algorithmic complexity of phase estimation by number of modes.

Although FDE can reduce the computational complexity of the MIMO processing, due to large mode group delay (MGD) of FMF link and block processing, the algorithm still requires enormous memory and high hardware complexity. In order to reduce the required tap length (RTL) of the equalizer, differential mode group delay compensated fiber (DMGDC) has been proposed. In this dissertation, the analytical expression for RTL is derived for DMGDC systems under the weak mode coupling assumption. Instead of depending on the overall MGD of the link

in DMGD uncompensated (DMGDUC) systems, the RTL of DMGDC systems depend on the MGD of a single DMGDC fiber section. The theoretical and numerical results suggest that by using small compensation step-size, the RTL of DMGDC link can be reduced by 2 orders of magnitude compared to DMGDUC link.

To compensate the loss of different modes, multimode EDFAs are presented with re-configurable multimode pumps. By tuning the mode content of the multimode pump, mode-dependent gain (MDG) can be controlled and equalized. A proto-type FM-EDFA which could support 2 LP modes was constructed. The experimental results show that by using high order mode pumps, the modal gain difference can be reduced. By applying both multimode EDFA and equalization techniques, 26.4Tb/s MDM-WDM transmission was successfully demonstrated.

A brief summary and several possible future research directions conclude this dissertation.

To my family

ACHKNOWLEDGMENTS

First of all, I would like to express my deepest appreciation to my doctoral advisor Professor Guifang Li who guides me to the fascinating field. He taught me how to think and approach a research topic systematically. Without his guidance and persistent support, I can never achieve the accomplishment so far.

Secondly, I would like to send my great thanks to the mentor of my internship, Dr. Ezra Ip. Without his advice and help, the internship in NEC Labs, America can never be that productive and rewarding.

Thirdly, I would like to appreciate all the members of my dissertation committee: Prof. Ayman Abourady, Prof. Axel Schülzgen, Prof. Demetrios Christodoulides and Prof. Ronald L. Phillips for their valuable suggestions and discussions.

Furthermore, I would like to thank the current and previous members of Optical Fiber Communication Group: Fatih Yaman, Likai Zhu, Xiaobo Xie, Eduardo Mateo, Cen Xia, Bing Huang, Yu Xie, Professor Dagong Jia and Jing Zhang. I feel so lucky and proud to work in the team. Besides, I would like to thank Prof. Rodrigo Amezcua for helpful discussions. I am also grateful to members of NEC Labs: Yuekai Huang, Mingfang Huang, Dayou Qian, Phillip Ji, Ying Shao, Shaoliang Zhang and Ting Wang for their lasting support and assistance.

Last but not least, I would like to acknowledge my parents and my fiancée Yuheng Wang who made the dissertation possible by their constant support in all kinds of situation and gave me their blessing to this undertaking.

TABLE OF CONTENTS

LIST OF FIGURES xi

LIST OF TABLES xvi

LIST OF COMMON ACRONYMS AND ABBREVIATIONS xvii

CHAPTER 1 INTRODUCTION 1

1.1 Limit of Single-Mode Fiber Transmission 1

1.2 Mode-division Multiplexed Transmission 3

1.2.1 Fiber Modes 3

1.2.2 Mode-division Multiplexed Transmission 5

1.3 Dissertation Outline 6

CHAPTER 2 EFFICIENT DIGITAL SIGNAL PROCESSING FOR FEW-MODE FIBER TRANSMISSION 9

2.1 Introduction 9

2.2 Time Domain Equalization 12

2.2.1 Algorithm Description 12

2.2.2 Complexity Requirement 15

2.3 Frequency Domain Equalization 15

2.3.1 Algorithm Description 15

2.3.2 Complexity Requirement 20

2.4 FDE for mode-division multiplexed transmission in FMF 21

2.4.1 Simulation 21

2.4.2 Single Span Transmission Experiment 28

2.4.3 Long Distance Transmission Experiment 32

2.5 FDE for fundamental mode transmission in FMF 37

2.5.1 Simulation 38

2.5.2 Transmission Experiment 42

2.6 Conclusion 46

CHAPTER 3 MODE-DIVISION MULTIPLEXED TRANSMISSION IN DIFFERENCIAL GROUP DELAY COMPENSATED FIBER LINK 47

3.1 Introduction 47

3.2 Theory 48

3.2.1 DMGD compensated fiber link 48

3.2.2 Impulse Response of DMGD uncompensated link 49

3.2.3 Impulse Response of single DMGD compensated pair 51

3.2.4 Impulse Response of DMGD compensated link 53

3.3 Simulation 54

3.3.1 Fiber Design and Simulation Setup 54

3.3.2 Results 55

3.4 Conclusion 58

CHAPTER 4 MULTIMODE ERBIUM DOPED FIBER AMPLIFIER FOR MODE-DIVISION MULTIPLEXED TRANSMISSION 59

4.1 Introduction 59

4.2 Theory and Model 60

4.3 Simulation Setup 65

4.4 Modal Gain Control using Reconfigurable Multimode Pump 66

4.4.1 Modal gain control for non-degenerate mode 66

4.4.2 Modal gain control for degenerate mode 70

4.4.3 Impact on performance due to inexact excitation and mode coupling 72

4.4.4 Impact on performance due to macro-bending loss 74

4.5 Conclusion 76

CHAPTER 5 WAVELENGTH-DIVISION MULTIPLEXED – MODE-DIVISION MULTIPLEXED TRANSMISSION USING ONLINE FEW-MODE EDFA 78

5.1 Introduction 78

5.2 Few-mode EDFA 78

5.3 Phase Plate 83

5.4 WDM-MDM Transmission Experiment 84

5.4.1 Experiment Setup 84

5.4.2 Results 87

5.4.3 Fiber Characterization 92

5.5 Conclusion 95

CHAPTER 6 SUMMARY AND FUTURE RESEARCH DIRECTION 96

REFERENCE 101

LIST OF FIGURES

Figure 1: Field distributions of fiber modes 4

Figure 2: Schematic diagram of an MDM transmission system 5

Figure 3 Schematic diagram of mode coupling between non-degenerate modes 9

Figure 4 DSP structure of adaptive TDE for 2-mode transmission 12

Figure 5 Block diagram of MIMO TDE for one mode channel 13

Figure 6 Block diagram of MIMO FDE for one mode channel 16

Figure 7 Block diagram of FDE for *D* modes system operating on two samples per symbol..... 18

Figure 8 Complex multiplies per symbol vs. filter tap length 21

Figure 9 Configuration of simulated system 22

Figure 10 Q^2 factor Vs. Link distance (OSNR=16dB) 23

Figure 11 Complexity Vs. Distance 24

Figure 12 Magnitude of the even FDE sub-filter coefficients in the time-domain for a 2-span transmission 25

Figure 13 Q^2 factor vs training symbol length for the proposed FDE algorithm 26

Figure 14 Q^2 Vs. rotational angular frequency (OSNR=19dB) 27

Figure 15 Experimental setup 28

Figure 16 (a) BER vs. OSNR; (b) Complexity as a function of filter tap length 29

Figure 17 (a) Q^2 factor vs. training sequence length when using the FDE; (b) recovered signal constellations at a training length of 30,000 30

Figure 18 Phase traces independently estimated from six spatial channels 30

Figure 19 DSP architecture using master-slave carrier recovery scheme 31

Figure 20 BER vs. OSNR compared between MS-CR and conventional CR 32

Figure 21 Experiment setup for a FMF loop experiment. Inset A: Few-mode erbium-doped fiber amplifier 32

Figure 22 (a) MSE vs. symbol index for 600km FMF transmission (b) Q^2 Vs. length of training sequence for NA-FDE after 1,000-km FMF transmission 34

Figure 23 Comparison between FDE and TDE: (a) Q^2 vs. Distance (b) Complexity vs. Distance 35

Figure 24 Comparison between C-PE and MS-PE: Q^2 vs. Distance 36

Figure 25 (a) Q^2 factor Vs. the number of total filter taps (b) Magnitude of sub-filter tap weights for 30×100km FMF transmission link at OSNR of 17dB 39

Figure 26 Q^2 factor Vs. OSNR for 30×100km transmission 41

Figure 27 Q^2 factor Vs. distance and the constellation diagrams for two Q^2 values are also shown on the right hand side 42

Figure 28 Pulse waveform measured at the output of the FMF at 1550nm 42

Figure 29 Transmission experiment setup 44

Figure 30 Q^2 Vs OSNR and the constellation diagrams for two Q^2 values are also shown on the right hand side 45

Figure 31 Typical sub-filter (odd) tap weights for FDE 46

Figure 32 A single span of DMGDC fiber 48

Figure 33 A single span of DMGD uncompensated fiber 50

Figure 34 A single span with one DMGD compensation pair with mode coupling in (a) P type section (Case I), (b) N type section (Case II) 51

Figure 35 Trench assisted graded index profile of P type (α = 2.079) or N type (α = 2.196) 54

Figure 36 Magnitude of impulse response Vs. number of tap periods for (a) h_{21} of 10×128km P-type fiber link; (b) h_{21}, (c) h_{12} and (d) h_{11} of 10× (64km(P)+64km(N)) DMGDC fiber link..... 56

Figure 37 Q^2(dB) Vs. Tap number used in LMS equalizer when MSC equals to -35dB/km..... 56

Figure 38 Required tap number Vs. compensation step-size for various MSCs 57

Figure 39: Schematic diagram of an MM-EDFA 60

Figure 40: Multimode Erbium-doped fiber amplifier 61

Figure 41: (a) Intensity profile of pump and signal modes, (b) normalized intensity profiles viewed along x-axis 65

Figure 42: Modal gain of signal at 1530 nm assuming 0.05 mW power in each degenerate modes of $LP_{01,s}$ and $LP_{11,s}$, when 980-nm pump is entirely confined in (a) $LP_{01,p}$, (b) $LP_{11,p}$ and (c) $LP_{21,p}$ 66

Figure 43： Modal gain and required $LP_{01,p}$ power vs. $LP_{21,p}$ power, to maintain MDG ($\Delta G_{11s-01s}$) at (a) 1 dB and (b) 2 dB; (c) Modal gain and MDG vs. $LP_{01,p}$ power for fixed $LP_{21,p}$ power at 150 mW..... 68

Figure 44: Modal gain and MDG difference vs. EDF length, when $LP_{01,p}$ and $LP_{21,p}$ have powers of: (a) $P_{p,21}$ = 150 mW, $P_{p,01}$ = 0 mW,and (b) $P_{p,21}$ = 150 mW, $P_{p,01}$ = 8 mW..... 69

Figure 45: Rotated pump modes 70

Figure 46: Modal gain vs. relative rotation angle (θ) of the pump mode when pump powers are: (a) $P_{p,11\theta}$ = 150 mW, (b) $P_{p,21\theta}$ = 150 mW, and (c) $P_{p,21}$ = 150 mW, $P_{p,01}$ = 2 mW, $P_{p,11\theta}$ = 15 mW..... 71

Figure 47: Modal gain vs. power leakage, (a) $LP_{21,p}$ to $LP_{01,p}$, (b) $LP_{21,p}$ to $LP_{11,p}$, (c) $LP_{21,p}$ to $LP_{02,p}$ 73

Figure 48 Modal gain vs. mode coupling strength from $LP_{21,p}$ to $LP_{01,p}$ ($d_{p,21\leftrightarrow 02}$) 74

Figure 49: Macro-bending loss vs. bending radius 75

Figure 50: Modal gain vs. mode dependent loss of LP_{11s} 75

Figure 51 (a) Refractive index of MM-EDF, (b) Normalized radial intensity profiles of signal and pump modes 78

Figure 52 Experiment setup 79

Figure 53 Modal gain vs. Pump power when pumping forward in: (a) $LP_{01,p}$, (b) $LP_{21,p}$, and backward in(c) $LP_{01,p}$ (d) $LP_{11,p}$ 81

Figure 54 (a) Modal gain vs. signal wavelength, using $LP_{21,p}$ (forward) and $LP_{11,p}$ (backward) and (b) MDG vs. signal wavelength using forward pumps in $LP_{01,p}$, $LP_{21,p}$ and backward pumps in $LP_{01,p}$, $LP_{11,p}$ 82

Figure 55 Experimental Setup 84

Figure 56 (a) Intensity patterns at transmitter, (b) intensity patterns after 50-km FMF 85

Figure 57 BER vs. OSNR 87

Figure 58 Time-domain equalizer taps after convergence 88

Figure 59 Training characteristic: Mean square error vs. adaptation period 90

Figure 60 Q vs. Launch Power after transmission 90

Figure 61 Measured BER for all WDM channels after transmission. Insets: Constellation diagrams of best and worst modes 91

Figure 62 Q penalty vs. No. of taps per tributary of 6×6 equalizer 92

Figure 63 Predicted (a) differential mode group delay and (b) chromatic dispersion 93

Figure 64 Measured (a) differential MGD and (b) dispersion characteristic for experimental FMF 94

Figure 65 Measured OTDR traces at different offset launch positions 94

LIST OF TABLES

Table 1: List of variables used in the coupled equations 64

Table 2: Parameters of a MM-EDFA 66

Table 3： Overlap Integrals of normalized intensity profile 67

LIST OF COMMON ACRONYMS AND ABBREVIATIONS

ASE	Amplified Spontaneous Emission
BER	Bit Error Rate
BPSK	Binary Phase Shift Keying
CD	Chromatic Dispersion
CIRS	Channel Impulse Response Spread
CR	Carrier Recovery
CW	Continuous Wave
DA	Data Aided
DD	Decision Directed
DFB	Distributed Feedback
DEMUX	De-multiplexer
DMGD	Differential mode group delay
ECL	External Cavity Laser
EDFA	Erbium Doped Fiber Amplifier
FDE	Frequency Domain Equalizer
FFT	Fast Fourier Transform
FMT	Fundamental Mode Transmission
FMF	Few-mode Fiber
FIR	Finite Impulse Response

LMS	Least Mean Square
LO	Local Oscillator
MCF	Multicore Fiber
MDG	Mode Dependent Gain
MDM	Mode-Division Multiplexing
MGD	Mode Group Delay
MMF	Multimode Fiber
MPI	Multi-path Interference
OSNR	Optical Signal-to-Noise Ratio
PBS	Polarization Beam Splitter
PD	Photo-diode
PDM	Polarization-Division Multiplexing
PRBS	Pseudo Random Binary Sequence
QPSK	Quadrature Phase Shift Keying
RTL	Required Tap Length
RTO	Real Time Oscilloscope
SMF	Single-Mode Fiber
SNR	Signal-to-Noise Ratio
TDE	Time Domain Equalizer
WDM	Wavelength-Division Multiplexing

CHAPTER 1 INTRODUCTION

1.1 Limit of Single-Mode Fiber Transmission

Fueled by emerging bandwidth-hungry applications and the increase in computer processing power that follows Moore's Law, the internet traffic is growing exponentially and the trend is expected to continue for the foreseeable future[1]. So far, the technology of optical fiber communication can provide capacity which always exceeds the increasing demand by orders of magnitude. However, the margin between them starts to shrink in recent years. It is well known that the capacity of a transmission channel is up-bounded by Shannon's limit which can be expressed as $C = W\log(1+SNR)$ where W denotes the bandwidth of the channel and SNR represents the signal-to-noise ratio. In past two decades, wavelength-division multiplexing (WDM) has been widely used in optical fiber communication system to expand the transmission bandwidth by a factor of as much as 100 or more. By exploiting the low loss transmission window beyond the C and L band, the transmission bandwidth could be further increased[2]. However, the expansion is limited to below one order of magnitude. Moreover, lack of an integrated amplification platform makes such system unattractive from technical and economic perspectives.

Recently, advances in coherent detection have led to tremendous capacity growth in optical fiber by using high spectral efficiency modulation format [3]. Furthermore, digital coherent optical communication enables polarization-division multiplexing (PDM) which doubles the channel capacity [4]. In 2011, 100-Tb/s transmission at a spectral efficiency of 11 b/s/Hz was reported in a single-mode fiber [5]. Owing to the nonlinear refractive index of silica,

it is impossible to continue increasing spectral efficiency infinitely by merely increasing the launched power. One method to reduce fiber nonlinearity is to increase the effective area of the propagating mode, thus reducing the optical intensity and the resulting nonlinear effects [6]. However, mode effective area is limited by bending loss and by the requirement of the waveguide to be single-mode. Recently, fundamental mode transmission (FMT) is proposed to transmit data in the fundamental mode of a “few-mode fiber” (FMF) [7, 8]. Provided mode coupling is low, the signal will remain single-mode during propagation. The larger effective area of the fundamental mode in FMF in comparison with that achievable in SMF can further reduce nonlinearity. However, a nonlinear capacity limit will always exist. Even if the transmission medium is linear, the Shannon limit formula shows that the capacity scales only logarithmically with signal-to-noise ratio. The logarithmical channel capacity scaling ultimately cannot meet the demand of exponential traffic growth from a technical perspective as well as the perspective of power consumption per bit. To achieve a cost-effective scaling in system capacity, new paradigms in optical transmission are required.

Although it seems to be impossible to provide exponential single-channel capacity growth, multiplicative growth in optical communication capacity, for example using WDM, has satisfied traffic demand in the past. As current WDM coherent optical communication system has already exhausted all degrees of freedom, namely quadrature, frequency and polarization in single-mode fiber, space is the only new dimension that can be considered in next generation of optical fiber communication system. To utilize the degree of freedom, space-division multiplexing has been proposed. In SDM system, independent data streams can be transmitted in parallel spatial channels. Indeed, transmission over parallel orthogonal channels has been well

established in wireless systems, where the achievable capacity using multiple-input multiple-output (MIMO) antennas increases with the number of independent "eigen-channels," which under the assumption of rich multipath, scales as the minimum of the number of antenna deployed at the transmitter and receiver [9].

In optical fiber transmission, three SDM schemes have been proposed. These are (i) core multiplexing using multicore fibers (MCF), where a single strand of glass fiber contains a number of independent single- (or multi-) mode cores each capable of communicating optical signals [10, 11]; and (ii) mode-division multiplexing (MDM) using multimode fibers (MMF) or few-mode fibers (FMF), where a single strand of fiber has one core with sufficiently large cross-section area to support a number of independent guiding modes [12]; (iii) hybrid approach using MCF with few mode core, where MDM transmission is performed through each core while all the cores are multiplexed in a single strand of fiber [13]. Both multiplexing schemes have attracted intensive interests in the last 3 years for the next multiplicative capacity growth for optical communication.

1.2 Mode-division Multiplexed Transmission

1.2.1 Fiber Modes

Optical fibers are cylindrical waveguides compromising a high refractive index (n_1) core surrounding by low index (n_2) cladding as shown in Figure 1. A guided mode is a solution of wave equation describing an electro-magnetic field distribution which propagates invariant along the fiber except for the change in its over-all scaling and phase. The number of guided modes in

an optical fiber is determined by normalized frequency V [14], $V = \frac{2\pi}{\lambda} a \sqrt{n_1^2 - n_2^2}$ where a denotes radius of the core and λ represents wavelength of the field. When V is small, only fundamental mode LP_{01} is guided as in single-mode fiber. As V exceeds 2.405, the fiber can support LP_{11} mode group which consists two degenerate modes $LP_{11,e}$ (even) and $LP_{11,o}$ (odd), illustrated in Figure 1.

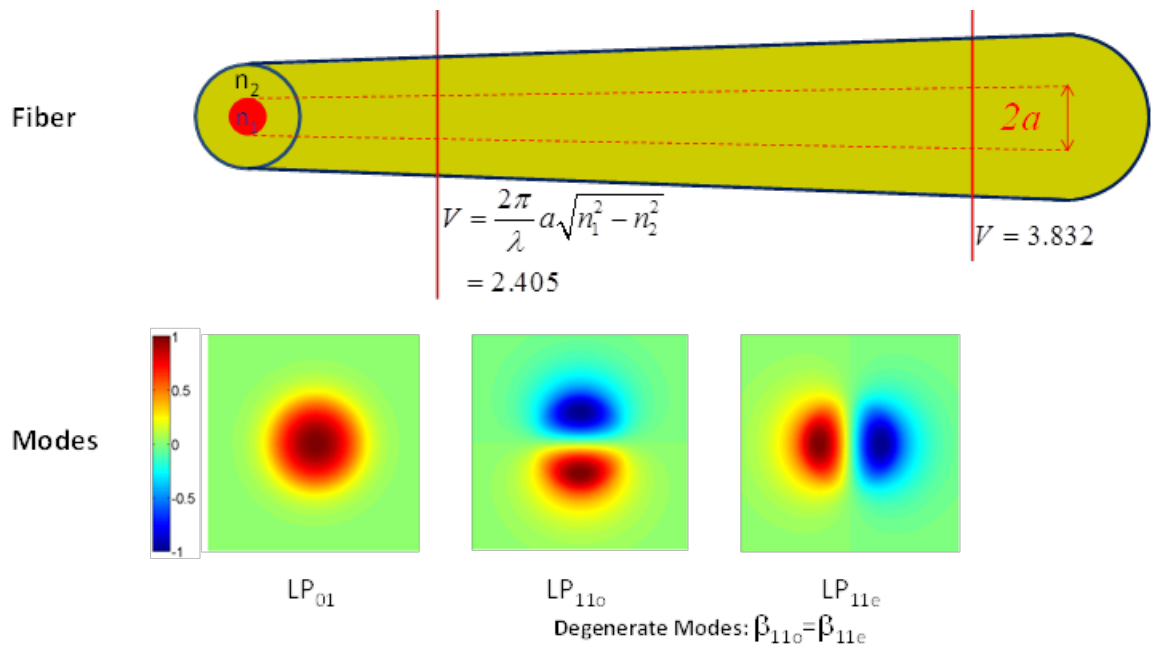

Figure 1: Field distributions of fiber modes

Let ψ_{01} and ψ_{11} represent the normalized mode profiles for LP_{01} and LP_{11}. By definition, guided modes are orthonormal, i.e.

$$\iint \psi_{01} \cdot \psi_{01} dr d\theta = \iint \psi_{11} \cdot \psi_{11} dr d\theta = 1 \qquad (1)$$

$$\iint \psi_{01} \cdot \psi_{11} dr d\theta = 0 \qquad (2)$$

which forms the basis of mode-division multiplexing where independent data streams are transmitted and received simultaneously in each fiber mode.

1.2.2 Mode-division Multiplexed Transmission

An MDM transmission system basically compromises few/multi-mode fiber, transmitter and receiver array, and mode MUX/DEMUX as shown in Figure 2.

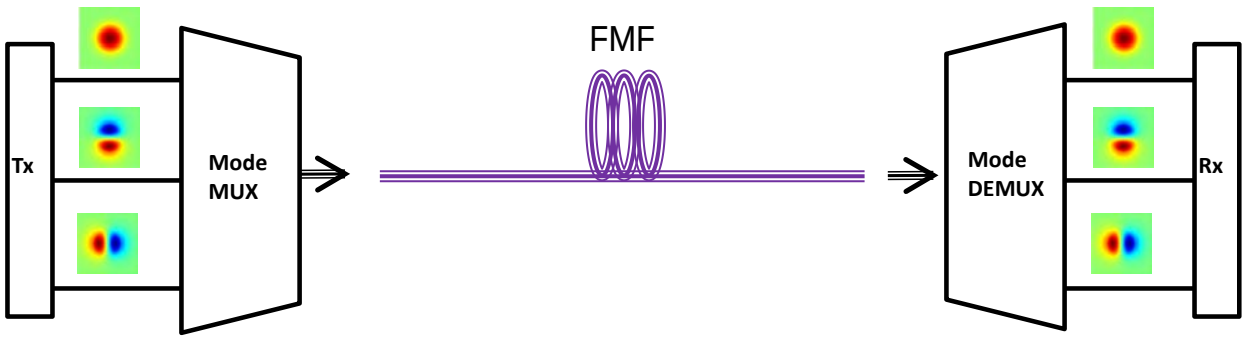

Figure 2: Schematic diagram of an MDM transmission system

Optical fibers supporting several or more modes serve the transmission media of MDM system. Although traditional multimode could provide hundreds of guiding modes, the properties such as mode dispersion and mode dependent loss are hard to manage nowadays. As a result, currently most of MDM systems with transmission distance longer than 10km are demonstrated in FMFs. Recently, several low mode loss (<0.2dB/km) and low differential mode group delay (DMGD) FMFs are realized and tested in experiments [15].

To enable MDM transmission, mode MUX and DEMUX are critical components to transform signals from parallel single-mode fibers to MDM signals which contain superposition of modes in FMF. One widely used mode MUX compromises 2 components: mode converters and combiner. Fundamental signals from single-mode fibers are first converting to desired

modes and then combined and coupled to FMF. The mode converter can be realized using phase plate [16] and spatial phase modulator [17] in free space setup or using fiber based device such as long period fiber Bragg grating [18] or structured direction coupler [19]. A mode DEMUX is just a reverse setup of mode MUX. It should be noted that the insertion losses of aforementioned methods are high (9-10dB for phase plate method) due to using beam splitters (BS) as the beam combiner. Recently, low loss mode MUX/DEMUXs based on 3 spot coupler [20] or photonic lantern [21] are demonstrated. The new approaches do not directly excite particular modes of the fiber, but excite a set of orthonormal mode mixtures in a way that coupling matrix between single-mode fibers and few-mode fibers is unitary. The 3 spot coupler has demonstrated 4 dB insertion loss as mode DEMUX.

After mode DEMUX, parallel signals are launched into the receiver. Ideally, signals from different mode channels propagate independent on each other. Thus, coherent receiver array can be used to detect each spatial channel separately. However, in practical, due to mode coupling in fibers as well as in components such as mode MUX/DEMUX, signals are affected by multimode interference. To recover the signal, MIMO equalization has to be implemented in the digital receiver. The details regarding to mode coupling and MIMO process are described in Chapter 2.

1.3 Dissertation Outline

The outline of the dissertation is laid out as follows

Chapter 1 presents the motivation, background and organization of the dissertation. The concept of fiber modes is reviewed and basic principles of mode-division multiplexing are introduced.

In MDM system, the first challenge is the multimode interference. Chapter 2 is dedicated to explain the challenge and discuss how to use MIMO processing to efficiently overcome it. After a brief introduction of mode coupling effect in FMF, two approaches of adaptive MIMO processing are discussed: i) Time domain equalization (TDE), ii) Frequency domain equalization (FDE). Compared to the conventional TDE, the proposed adaptive FDE reduces the algorithmic complexity by orders of magnitude while maintaining similar performance. Moreover, master-slave carrier recovery is proposed for further reduction on algorithmic complexity. The principles of methods are described and validated in simulations as well as experiments. The first experiment is demonstrated in single span (50 km) [22] while the second experiment extends the distance to multiple spans (1000km) [23]. The performances for FDE and TDE are measured for various distances. The results verify that FDE shows similar performance as TDE and master-slave phase estimation can be used to reduce carrier recovery complexity with less than 1 dB Q^2-penalty. To increase the converge speed of the adaptive algorithm, normalized adaptive FDE (NA-FDE) is applied and compared to conventional adaptive FDE (CA-FDE). It is observed that NA-FDE converges six times faster compared with CA-FDE at a mean square error (MSE) of 10^{-5}. As a simplified case of MDM transmission, fundamental mode transmission (FMT) is also investigated and discussed in the chapter. FMT can utilize the larger effective area of fundamental mode in FMF to increase nonlinearity tolerance. By using FDE, multipath interference in FMT can be efficiently mitigated [24].

Although FDE can reduce algorithmic complexity significantly, the hardware complexity is still high due to large FFT size determined by the channel impulse response spread (CIRS). To reduce CIRS, DMGD compensated (DMGDC) link has been proposed and demonstrated. In chapter 3, the equalizer size requirement is investigated analytically and numerically for DMGDC link with weakly random mode coupling. Each span of the DMGDC link comprises multiple pairs of sections of fibers which have opposite sign of DMGD. The result reveals that under weakly random mode coupling, the required length of the equalizer is proportional to MGD of a single DMGD compensated section instead of the total MGD in DMGD uncompensated link. By using small compensation step-size, the required equalizer length can be potentially reduced by 2 orders of magnitude compared to DMGD uncompensated link.

The second challenge of MDM transmission is how to compensate the losses of different mode channels. To resolve the challenge, multimode Erbium doped fiber amplifier (EDFA) is proposed. Chapter 4 presents theoretical and numerical analysis of a multimode EDFA with modal gain control by tuning mode contents of the pump. By adjusting the powers and orientation of input pump modes, modal dependent gain can be tuned over a large dynamic range. Performance impacts due to excitation of undesired pump modes, mode coupling and macro-bending loss within the erbium-doped fiber are also investigated.

In chapter 5, a mode-division multiplexed WDM transmission experiment is demonstrated over 50-km of FMF using a few-mode EDFA. The experimental setup of system components such as phase plate based mode MUX/DEMUX and few-mode EDFA are discussed. The transmission results and characterization of FM-EDFA and FMF are also presented.

Summary and discussion about future research direction are included in chapter 6.

CHAPTER 2 EFFICIENT DIGITAL SIGNAL PROCESSING FOR FEW-MODE FIBER TRANSMISSION

2.1 Introduction

In ideal FMF, signal can be transmitted in a particular mode without affecting other mode channels. Nevertheless, in reality, signals among different modes can be cross coupled to each other. There are two main types of mode coupling effects [25]: i) mode coupling between degenerate modes. This kind of coupling is due to deviations on the ideal transverse index profile of the fiber. ii) mode coupling between non-degenerate modes induced by index perturbation along the fiber. Mode coupling leads to crosstalk between mode channels. As degenerate modes share the same propagation constant, they travel at the similar group velocity. In the absence of chromatic dispersion, crosstalk between degenerate mode pair only involves two symbols from each mode. With chromatic dispersion, this crosstalk will impact as many symbols as the dispersive spreading of each symbol. Regarding to the non-degenerate modes, due to the interplay between mode coupling and modal dispersion, the crosstalk further involves a block of symbols with total duration equaling to mode group delay (MGD).

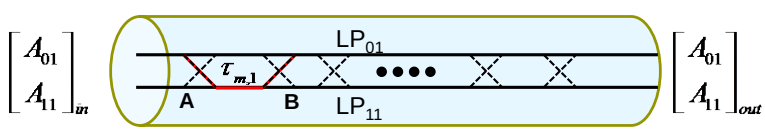

Figure 3 Schematic diagram of mode coupling between non-degenerate modes

The coupling between non-degenerate modes in a two-mode fiber can be schematically plot in Figure 3. Two parallel straight lines symbolize non-interacting trajectories of two modes. A_{01} and A_{11} denote complex amplitudes of mode channels in LP_{01} and LP_{11}. The doted crosses

represent mode coupling events. As mode coupling is due to random longitudinal index fluctuation induced by manufacturing process and micro-bending in the cable, the coupling location and strength are random distributed along the fiber. For simplicity, let us first consider two coupling events A and B in the fiber. Signal from LP_{11} can travel from A to B via two paths: i) straight path in LP_{11}. ii) couple to LP_{01} at A, propagate in LP_{01} for a distance and coupled back to LP_{11} at B. Because of modal dispersion, the signal arriving via the multiple-coupled path will accumulate a MGD. In practice, coupling events are much more than 2 and distributed everywhere in the fiber. To describe overall coupling effect, mathematically, for a two-mode fiber, an input-output relationship can be constructed as

$$\begin{bmatrix} A_{01}(t) \\ A_{11}(t) \end{bmatrix}_{out} = \begin{bmatrix} h_{11} & h_{21} \\ h_{21} & h_{22} \end{bmatrix} * \begin{bmatrix} A_{01}(t) \\ A_{11}(t) \end{bmatrix}_{in} \tag{3}$$

where each entry of the coupling matrix $\overline{\overline{H(t)}}$ is in the form of

$$h_{11}(t) = \alpha\delta + \Sigma\varepsilon_i\delta\left(t - \tau_{m,i}\right),\ \ \tau_{m,i} \le \tau_{MGD} \tag{4}$$

where α represents loss due to mode coupling and the summation represents all possible combinations of the discrete coupling events along the fiber that allow the input signal in the the LP_{01} mode to remain in the same mode at the receiver, ε_i and $\tau_{m,i}$ represent the strength and time delay associated with the ith coupling combination, which is no greater than the total modal group delay of the entire link.

$$\Delta\tau_{MGD} = \Delta\tau_{DMGD} L \tag{5}$$

where $\Delta\tau_{DMGD}$ is the differential modal group delay and L is the length of the fiber. Therefore, each element of the coupling matrix is essentially a tapped-delay line filter.

For a MDM system using D spatial modes (included polarizations, the input-output relationship can be expressed as follows.

$$\overline{y(t)} = \overline{\overline{H(t)}} * \overline{x(t)} \tag{6}$$

where coupling matrix $\overline{\overline{H(t)}}$ is a $D \times D$ matrix of tapped-delay line filters with full rank, $\overline{x(t)}$ and $\overline{y(t)}$ denote transmitted and received signals respectively.

Although mode coupling causes multimode interference which greatly impacts the MDM signal quality, the mode coupling matrix is linear and unitary in the most of the time. Therefore, it is possible to invert $\overline{\overline{H(t)}}$ to recover the signal. Based on nature of coupling between the spatial degrees of freedom, it is highly unlikely that the coupling matrix can be inverted using optical techniques. To invert the coupling matrix in the electronic domain, the signals in all spatial degrees of freedom arriving at the receiver must be coherently and synchronously detected because the coupling and propagation in the fiber is sensitive to the phase of the signals. The detected signals are first digitized and then processed using digital signal processing (DSP). In the rest of the chapter, two DSP algorithms: conventional time domain equalization (TDE) [26] and efficient frequency domain equalization (FDE) are discussed and compared. Additionally, a master-slave carrier recovery method is also proposed to further reduce the algorithmic complexity of a MDM coherent receiver.

2.2 Time Domain Equalization

2.2.1 Algorithm Description

To recover signals from different mode channels at the receiver, an ideal linear equalizer implements inverted channel matrix $\overline{\overline{W(t)}}$ and applies it on the received signals.

$$\overline{x(t)} = \overline{\overline{W(t)}} * \overline{y(t)} \tag{7}$$

According to above equation, the equalization can be intuitively implemented in time domain. Figure 4 shows a canonical structure of an adaptive time domain equalizer for 2 mode transmission.

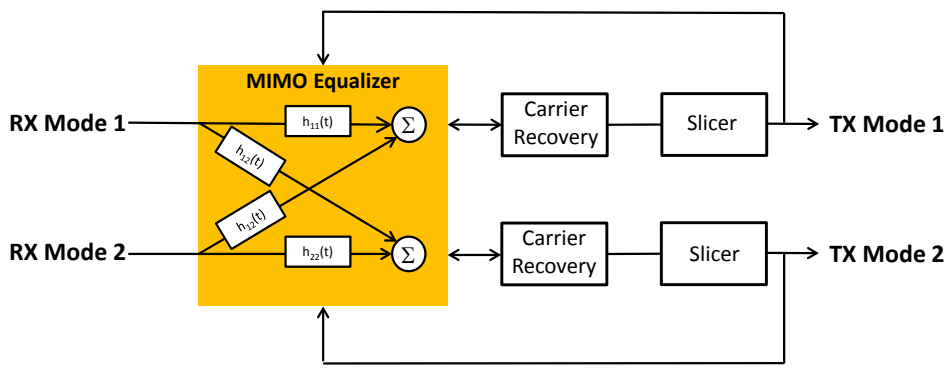

Figure 4 DSP structure of adaptive TDE for 2-mode transmission

In the digital coherent receiver, both in-phase (I) and quadrature (Q) components of optical signals from different mode channels are detected and digitized. The electric fields of the signals $\overline{y_{1,2}}(k)$ are then reconstructed and resampled. The channel inversion process is performed by a filter matrix which contains 4 taped-delay line filters. The input and output signals of the 2×2 filter bank can be related by

$$\begin{bmatrix} \overline{\hat{x}_1}(k) \\ \overline{\hat{x}_2}(k) \end{bmatrix} = \begin{bmatrix} \overline{w_{11}}(k) & \overline{w_{12}}(k) \\ \overline{w_{21}}(k) & \overline{w_{22}}(k) \end{bmatrix} * \begin{bmatrix} \overline{\hat{y}_1}(k) \\ \overline{\hat{y}_2}(k) \end{bmatrix} = \overline{\overline{W}}(k) * \begin{bmatrix} \overline{\hat{y}_1}(k) \\ \overline{\hat{y}_2}(k) \end{bmatrix} \tag{8}$$

where $\overline{\hat{x}_{1,2}}(k)$ denotes equalized symbols, $\{\overline{\overline{w_{ij}}}(k)\}$ $(i, j = 1,2)$ represent inverse channel filters and * denotes element-wise convolution. Figure 5 shows detailed block diagram of MIMO time domain equalizer for one mode channel.

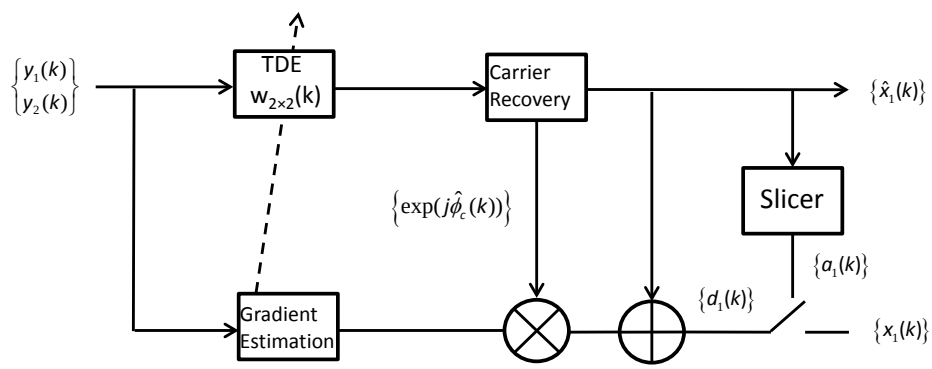

Figure 5 Block diagram of MIMO TDE for one mode channel

In order to further recover the symbols, laser phase noises have to be estimated and mitigated. The symbols after carrier recovery can be written as

$$\hat{x}_{1,2}^{'}(k) = \hat{x}_{1,2}(k)\exp\left(-j\hat{\phi}_{1,2}(k)\right) \tag{9}$$

where $\hat{\phi}_{1,2}$ denotes estimated laser phase fluctuations which can be computed using Viterbi-Viterbi approach [27] or maximum likelihood estimation method [28]. The estimation of filter coefficients generally can be acquired in blind or data-aided approach. The blind estimation approach can determine the filter coefficients by using information of receiving signal itself. However, the blind method normally exhibits slower convergence rate, worse performance for low SNR and more instability compared to data-aided one [29]. In the dissertation, I focus on

data-aided estimation methods. In the preamble of each data frame, a pre-known training sequence is inserted. Considering the high data rate used in optical fiber communication, least–mean-square (LMS) method is used to estimate the filter coefficients in following iterative algorithm:

$$\overline{\overline{W^{(m)}}} = \overline{\overline{W^{(m-1)}}} + \mu \begin{bmatrix} \varepsilon_1^{(m)} \overline{y_1^*}(k) & \varepsilon_1^{(m)} \overline{y_2^*}(k) \\ \varepsilon_2^{(m)} \overline{y_1^*}(k) & \varepsilon_2^{(m)} \overline{y_2^*}(k) \end{bmatrix} \tag{10}$$

where the error signals are calculated as

$$\varepsilon_{(1,2)}^{(m)} = \left(d_{1,2}(k)\Big|_m - \hat{x}_{1,2}^{'}(k)\Big|_m \right) \exp\left(j\hat{\phi}_{1,2}(k) \right) \tag{11}$$

where m is the symbol index label. $d_{1,2}(k)$ represents desired symbol sequence and μ denotes convergence step-size. In practical implementation, μ has to be optimized with respect to speed of convergence, stability and mis-adjustment of the adaptive process. It is noted that the phase noise is multiplied in equation (11). By doing so, phase fluctuations of $y_{1,2}^*(k)$ can be cancelled in equation (10).

The equalizer can work in two operational modes. They are data-aided (DA) mode when $d_{1,2}(k)\Big|_m = x_{1,2}(k)\Big|_m$ and decision directed (DD) mode when $d_{1,2}(k)\Big|_m = a_{1,2}(k)\Big|_m$ where $a_{1,2}(k)$ are symbols after hard-decision. At the starting training session, the equalizer works in DA mode to rapidly acquire the estimation of inverse channel filter coefficients. Then the equalizer will be switched to DD mode to further tune the equalizer and track the slowly varying channels.

2.2.2 Complexity Requirement

The total complexity of the algorithm can be measured by the number of complex multiplications per symbol per mode. TDE is assumed to use an FIR filter matrix adapted by the LMS algorithm. To compensate MGD and mode crosstalk completely, the equalization filter length should be equal or larger than the impulse response spread. The tap delay length of the filter is half symbol period and tap length is chosen to be the same as the total MGD of the FMF. Thus, N_f equals to $2\Delta\tau LR_s$ where $\Delta\tau$ is the DMGD of the fiber, L is the link distance, R_s is the symbol rate. The factor of 2 is due to the fact that half of the symbol period is commonly used for the tap delay of the equalizer. To compute each output symbol from one mode channel, DN_f multiplications are needed where D is the number of modes used for transmission. Updating the filter coefficients requires $DN_f/2$ multiplications. Therefore, the complexity for TDE without carrier recovery can be expressed as

$$C_{TDE} = 3D\Delta\tau LR_s \tag{12}$$

Consequently, the complexity of TDE scales linearly with mode group delay of the link, the number of used modes and the symbol rate.

2.3 Frequency Domain Equalization

2.3.1 Algorithm Description

According to section 2.2.2, the computational complexity of TDE depends linearly on the total DMGD of the link which makes TDE unfeasible for long-haul MDM transmission. To reduce computational cost, adaptive frequency-domain equalization (FDE) is proposed. A frequency-domain equalizer can be implemented by inserting FFTs and IFFTs into Figure 5. This

is shown in Figure 6 where the filter coefficients are frequency domain values. However, both the receiving signal and the error are in time-domain as the later are obtained by subtracting the receiving signal from desired symbols. To adjust the equalizer coefficients, the error has to be transformed to frequency domain.

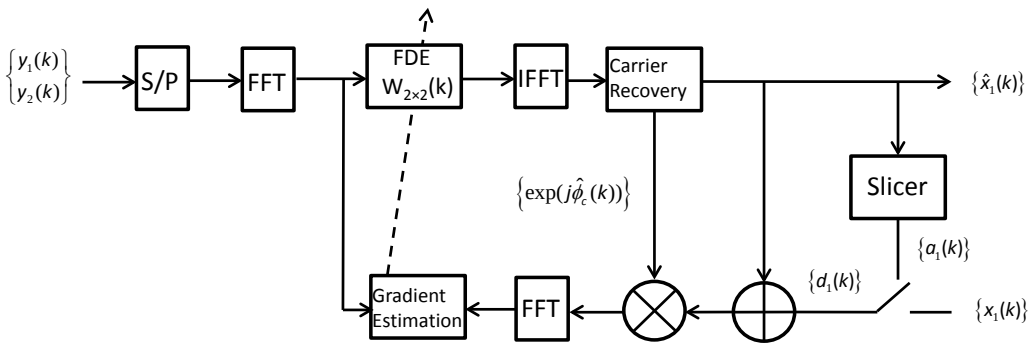

Figure 6 Block diagram of MIMO FDE for one mode channel

In real-time implementation, the received signals are parallelized and processed in blocks to facilitate FFTs/IFFTs. Overlap-and-save method is normally used to compute convolutions between received signals and the equalizer. The received signal is partitioned into overlapping blocks $\overline{y_{i,m}} = \left\{\overline{y_i}\left(k\right)\right\}\Big|_{mB-N_f+1}^{(m+1)B-1}$ where i and B are mode and block index respectively. The length of block is $L_B = N_f + B - 1 = 2^v$ which is an integer power of 2. A circular convolution is computed by taking FFT of the signal block, multiplying it with the equalizer block and then taking the IFFT. The last B samples of circular convolution are the same as the linear convolution and therefore are saved as equalized symbols.

For the adaptive FDE, error block can be computed in time domain as similar as TDE in equation (11) and then taken FFT. Frequency domain LMS method can be used to iteratively calculate equalizer coefficients as following

$$\overline{\overline{W^{(m)}}} = \overline{\overline{W^{(m-1)}}} + \mu \begin{bmatrix} \overline{E_{1,m}}(k) \otimes \overline{Y_{1,m}^{*}}(k) & \overline{E_{1,m}}(k) \otimes \overline{Y_{2,m}^{*}}(k) \\ \overline{E_{2,m}}(k) \otimes \overline{Y_{1,m}^{*}}(k) & \overline{E_{2,m}}(k) \otimes \overline{Y_{2,m}^{*}}(k) \end{bmatrix} \tag{13}$$

where $\overline{E_{i,m}}(k)$ represents mth error block for ith mode, $\overline{Y_{i,m}^{*}}(k)$ denotes conjugate of the signal block and $\otimes$ symbolizes element-wise multiplication. Both block values are in frequency domain.

Up until now, the FDE procedure addressed in Figure 6 is only suitable for 2 mode system. Additionally, it operates on only one sample per symbol basis while to cover the whole spectrum of signal over sampling rate of two is required. With the aim of addressing these issues, a more complete FDE is proposed in Figure 7 [30].

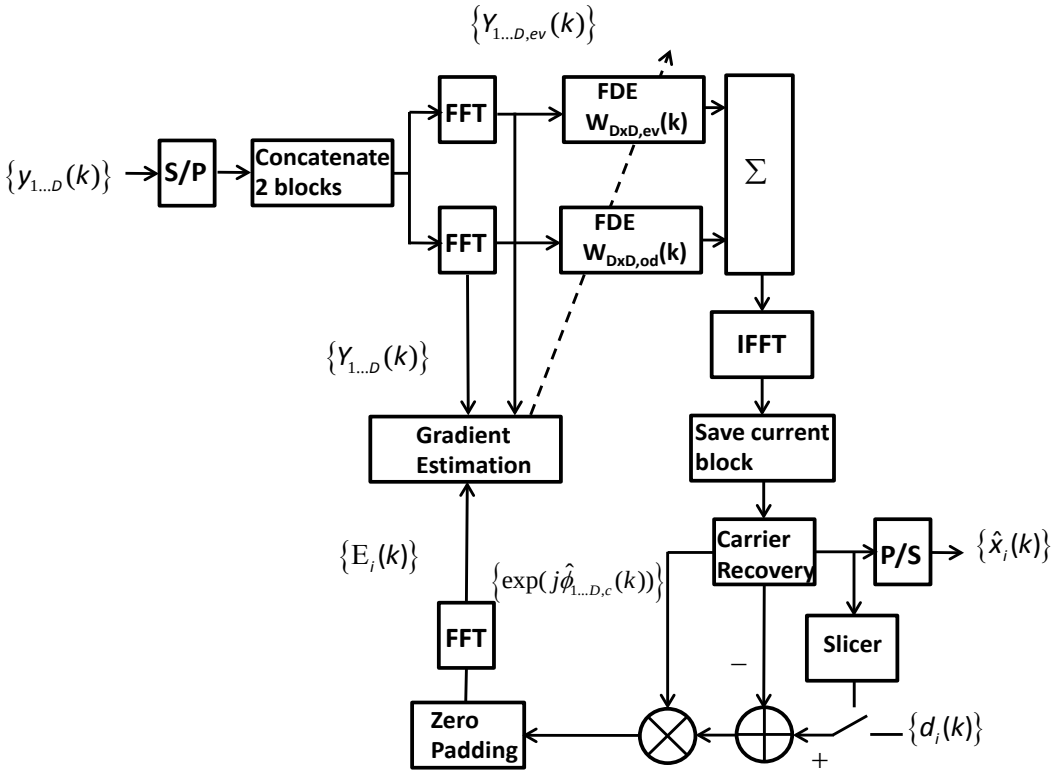

Figure 7 Block diagram of FDE for *D* modes system operating on two samples per symbol

$\{y_i(k)\}$ and $\{\hat{x}_i(k)\}$ represent the input signal and the output signal vectors of mode *i*, $1 \le i \le m$ .The overlap-and-save method is used to implement FDE. An overlap rate of 0.5 is chosen because it is simple to implement. After parallelization, two consecutive blocks are concatenated. To perform an equivalent half symbol spacing FIR filtering process, the input signal streams are divided into even and odd tributaries which are multiplied by sub-equalizers separately after fast Fourier transform (FFT) [31]. The filtered signal is the sum of outputs of the even and odd equalizers. $W_{i,ev/od}(k)$ is an inversed channel filter for the even or odd tributaries over ith mode.

To compensate MGD and mode crosstalk completely, the required tap length (RTL) of the equalizer should be larger than the impulse response spread. In order to mitigate laser phase noise, carrier recovery is applied in the time domain. The module calculates the estimated laser phase as well as the recovered signal. The error block then is generated by comparing the processed signal and the reference which could be a training sequence (data-aided mode) or the data after hard decision (decision-directed mode) in the time domain. The gradient for updating the filter for the qth input mode and the pth output mode is computed as following

$$\nabla_{pq}^{e,o}(k) = \mathrm{E}_p(k)\left(Y_q^{e,o}(k)\right)^* \tag{14}$$

where $\mathrm{E}_p(k)$ is the error block from the pth mode in the frequency domain and $\left(Y_q^{e,o}(k)\right)^*$ is the conjugated input signal block from the qth mode. Since $Y_q^{e,o}(k)$ is contaminated by the laser phase noise, to compute the gradient without the impact of the phase noise, the error block is multiplied by an estimated phase fluctuation $\exp\left(j\hat{\phi}_p(k)\right)$ in the time domain

$$e_p(k) = \left(d_p(k) - \hat{x}_p(k)\right)\exp\left(j\hat{\phi}_p(k)\right) \tag{15}$$

By doing so, the phase fluctuation factor in $\left(Y_q^{e,o}(k)\right)^*$ can be canceled in equation (14). The incremental adjustment $\Delta W_{pq}^{e,o}(k)$ then can be computed from the estimated gradient by

$$\Delta W_{pq}^{e,o}(k) = \mu \nabla_{pq}^{e,o}(k) \tag{16}$$

where μ is the convergence step size. The inverse channel filter weights converge to the optimum solution after a training process. Gradient constraint condition is applied to enforce an accurate calculation of linear convolution [32]. To track the temporal variation of the channel,

the algorithm is switched to the decision-directed mode after initial convergence. In contrast to TDE, calculations such as correlation and convolution can be simplified to be multiplication in FDE.

2.3.2 Complexity Requirement

For the adaptive FDE, it is most common to use block length equals to twice of the equalizer length. By using even and odd sub-equalizers, equivalent half symbol period delay spacing FIR filter can be realized in frequency domain [31]. To obtain $N_f / 2$ output symbols per mode per block, $2DN_f$ multiplications are needed. Updating both even and odd equalizers requires another $2DN_f$. The total number of FFT/IFFT per mode is $4+4D$ containing 2 FFT for the input, a pair of FFT/IFFT in the updating loop and 4*m* FFT/IFFT for executing gradient constraint in the gradient estimation block [32]. FFT is assumed to be implemented by the radix-2 algorithm requiring *N*log(*N*)/2 complex multiplications to execute FFT of *N* complex number. Thus the complexity for the proposed FDE can be expressed as

$$C_{FDE} = (4+4m)\log_2(2\Delta\tau LR_s) + 8m \qquad (17)$$

To compare algorithmic complexity of both FDE and TDE, Figure 8 shows the complexity as a function of filter tap length.

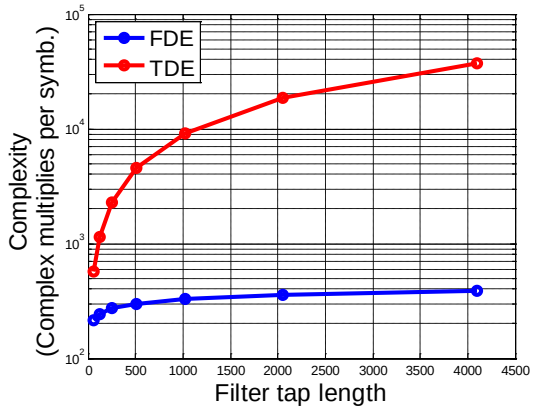

Figure 8 Complex multiplies per symbol vs. filter tap length

It can be concluded that FDE reduce the complexity significantly from TDE. For long-haul MDM transmission, the advantage of FDE is even more prominent since the required filter tap length is high.

2.4 FDE for mode-division multiplexed transmission in FMF

2.4.1 Simulation

To verify the effectiveness of the proposed FDE, a MDM system is simulated. Figure 9 shows the configuration of the simulated link. Without loss of generality, the transmission FMF supports only two modes, LP_{01} and LP_{11}. At the transmitter, two CW lasers with a 100 kHz line-width operating at 1550nm were separately modulated by two 28GBaud QPSK signals which were combined and coupled to the FMF by a mode-MUX. The fiber link included N spans of 100km FMF and N FM-EDFAs with noise figure of 5dB to compensate the span losses for both modes. At the receiver, a mode-DEMUX extracted two mode channels, which were fed into the coherent receivers. Digital signal processing was then applied on the received data to recover the signals.

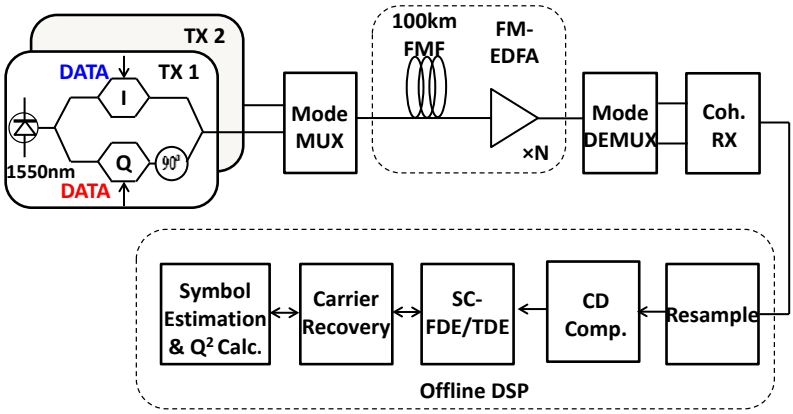

Figure 9 Configuration of simulated system

Multi-section field propagation model was used to simulate two-mode transmission in FMF [33].The random distributed mode coupling through FMF is taken into account in the model by multiplying a unitary rotation matrix at the end of every fiber section whose length equals to the coherent length L_c of the FMF ($L_c = 1km$ in the model). Mode scattering coefficient defined in [33] was set to be -30dB/km which is slightly higher than the fiber used in [34] (-34.4dB/km). Loss and dispersion coefficient were 0.2dB/km and 18ps/nm/km for both modes, the same as the FMF used in [12]. DMGD was set to be 27ps/km which was also aligned with [12]. At both ends of a single span of FMF, -22dB inter-mode crosstalk was assumed from mode MUX/DEMUX or splicing.

The received signal was resampled to 2 samples per symbol. The chromatic dispersion of the link was compensated by two static frequency domain equalizers. Two signal tributaries then enter the adaptive equalizer. To ensure the best performance, two carrier recovery stages were used. One was inside the adaptive loop applying DA-LMS phase estimation with training sequence and Viterbi-Viterbi phase estimation with transmitted data. The other stage located at

the output of the adaptive equalizer for decision directed-LMS phase estimation to further mitigate the laser phase noise. Although the two-stage phase estimation only provides 0.2dB improvement over single stage setup in terms of Q^2 factor for QPSK in the simulation, it is expected to deliver higher improvements for higher-order constellation or larger laser line-width. After carrier recovery, hard-decision symbols estimation is followed by Q^2 factor calculation.

To evaluate the performance of FDE, transmissions with different link distances from 100km to 2000km were simulated. To make a fair comparison, filter size, convergence step size and initial values of filter weights were chosen to be the same for both FDE and TDE. The filter length was larger than the total DMGD of the link. The amount of filter taps was selected to be an integer power of 2 to facilitate efficient FFT implementation. Before the coherent receivers, variable noise was loaded to ensure a fixed OSNR level of 16dB for different transmission distances. The first 10^5 symbols were used as training sequence followed by 9×10^5 test symbols. Figure 10 showed the Q^2 factor as a function of distance for both FDE and TDE.

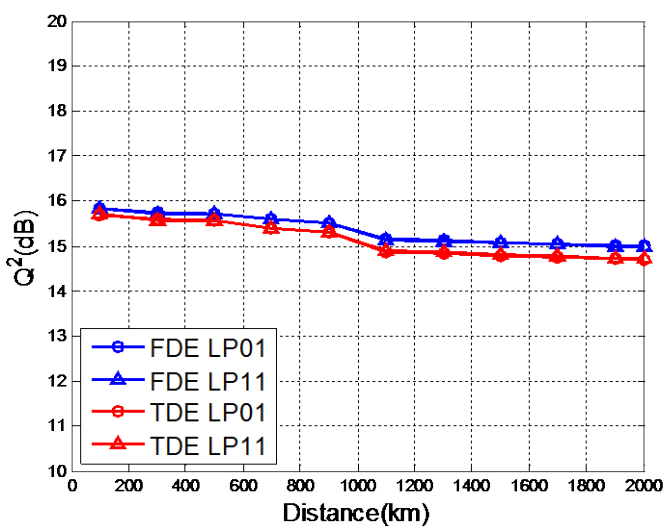

Figure 10 Q^2 factor Vs. Link distance (OSNR=16dB)

According to Figure 10, both FDE and TDE effectively mitigate the inter-mode cross talk and show similar performance. Based on equations (12,17), the computational complexity was also plotted in Figure 11.

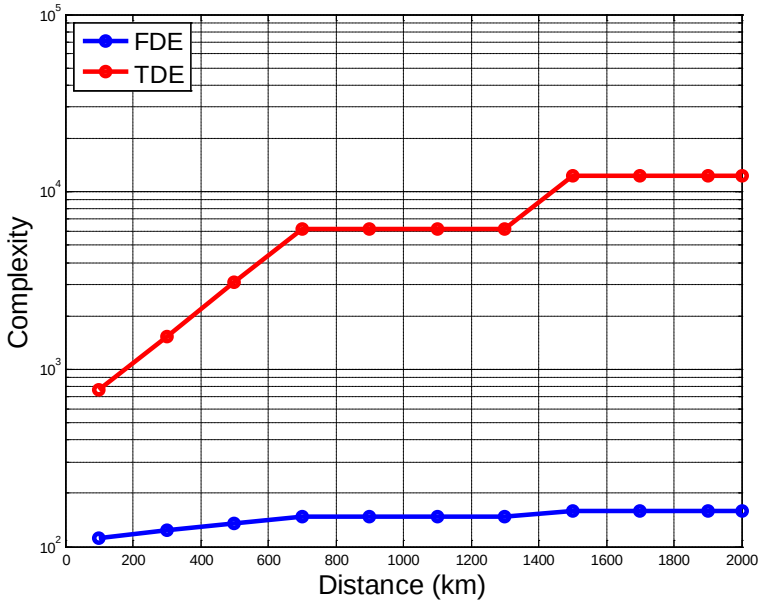

Figure 11 Complexity Vs. Distance

As the transmission distance grows, the accumulated DMGD increases leading to larger filter sizes. The complexity of FDE increases much slower than TDE due to the fact that the complexity of FDE scales logarithmically with the MGD instead of linearly. At a transmission distance of 2000km, FDE reduces complexity by a factor of as much as 77 compared to TDE.

The magnitude of FDE sub-filter coefficients for the even samples in the time domain after convergence was plotted in Figure 12 for 2×100km MDM transmission. The total DMGD is 5.4ns and the sub-filter contains 256 taps. The each diagonal filter element compensates multipath interference (MPI) for each mode while each off-diagonal filter element mitigates crosstalk between 2 mode channels. The dominant peaks in the diagonal filters correspond to

original signal. The relative delay between them coincides with the DMGD of 2 spans of FMF. The tap weights in the off-diagonal filter form a pedestal caused by distributed mode coupling through the fiber.

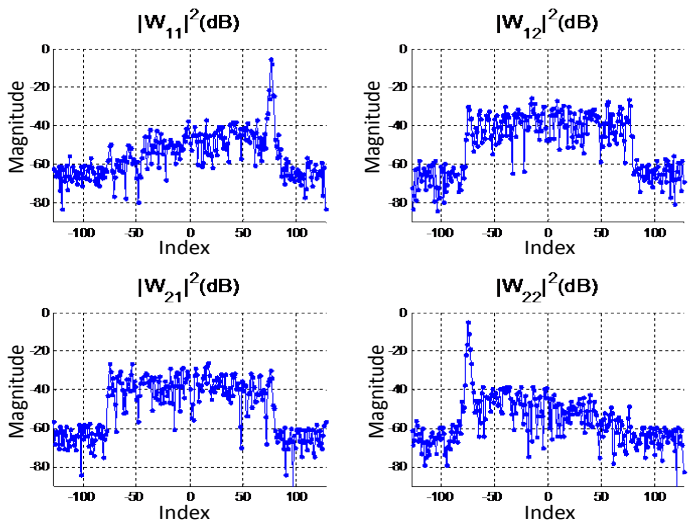

Figure 12 Magnitude of the even FDE sub-filter coefficients in the time-domain for a 2-span transmission

In the proposed FDE algorithm, a training process was used for initial convergence of the filter coefficients. In Figure 13, the Q^2 factor is plotted as a function of the training length when the tap length of the frequency domain sub-equalizer is 2048 and the total length of the data sequence is 1×10^6. According to Figure 13 when 2×10^4 training symbols are used, the Q penalty is about 0.9 dB. The minimum length of training symbols for the approach should be on that order.

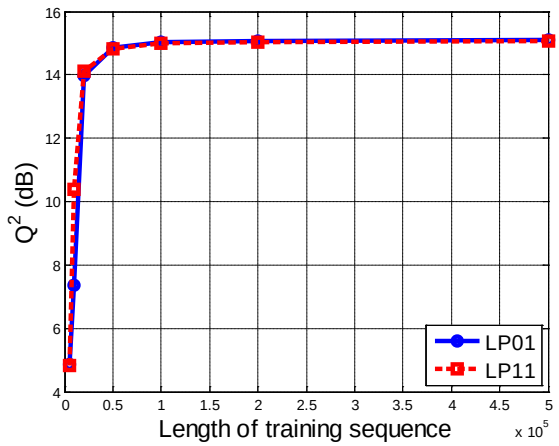

Figure 13 Q^2 factor vs training symbol length for the proposed FDE algorithm

In the proposed FDE algorithm, a training process was used for initial convergence of the filter coefficients. In Figure 13, the Q^2 factor is plotted as a function of the training length when the tap length of the frequency domain sub-equalizer is 2048 and the total length of the data sequence is 1×10^6. According to Figure 13, when 2×10^4 training symbols are used, the Q penalty is about 0.9 dB. The minimum length of training symbols for the approach should be on that order.

The simulation results above assumed that the mode coupling was static. However, in practice, especially for long-haul transmission, temporal variation of environmental conditions leads to time-variant mode coupling. One of the advantages of an adaptive equalizer is that it can continuously track the temporal variation of the system. To verify the dynamic response of FDE, a mode scrambler was inserted between the FMF and the mode DEMUX for the single-span transmission. The mode scrambler provided endless mode rotation with a time-dependent rotation matrix of angular frequency Ω.

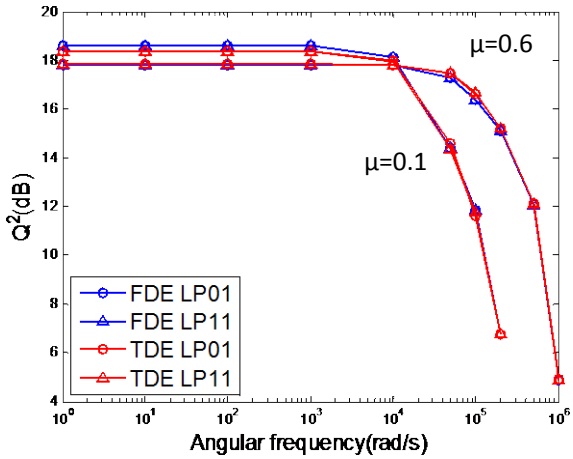

Figure 14 Q^2 Vs. rotational angular frequency (OSNR=19dB)

In Figure 14, Q^2 factor is shown as a function of the angular frequency of mode rotation for different convergence step sizes. The sub-filter size is 128 taps for the single span transmission. The Q^2 factor remains a constant until the variation is too fast to be tracked. The convergence property of the algorithm can be adjusted by tuning μ. The maximum Q^2 for $\mu = 0.1$ is slightly higher than $\mu = 0.6$ due to lower mis-adjustment. When $\mu = 0.6$, FDE only suffers a 0.4dB drop from the maximum in terms of Q^2 factor when the mode rotation is operated at 50krad/s. It should be noted that in a practical environment, the speed as well as the coupling strength is much smaller than in this simulation [35]. Besides, FDE shows the same tracking capability as TDE when μ is equal. Although FDE updates in the period of a block, the error signal is permitted to vary at the symbol rate which determines the effective updating rate. Therefore, FDE and TDE have the same convergence property [32]. It should be mentioned that the updating loop for FDE contains operations such as FFT and phase estimation which may slow down the tracking speed. In the simulation, the delay caused by those operations is not included.

2.4.2 Single Span Transmission Experiment

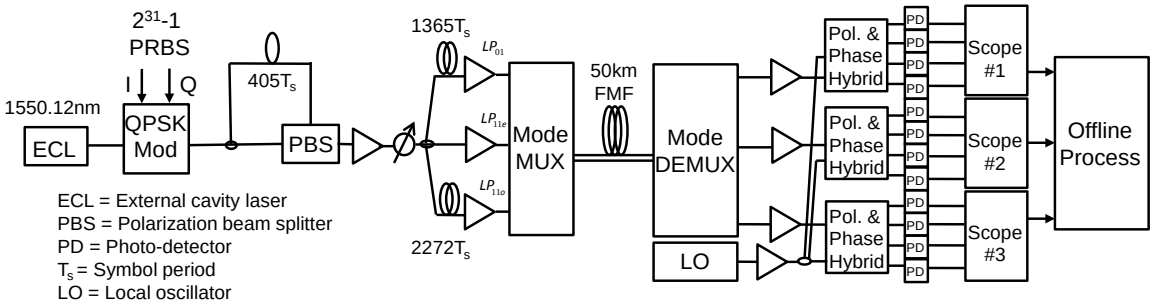

Figure 15 Experimental setup

The experimental setup is shown in Figure 15. At the transmitter, an external cavity laser at 1550.12 nm with a linewidth of 100 kHz is modulated by QPSK symbols at 28 Gbaud using a Mach Zehnder I/Q modulator. The I and Q symbols are chosen from pseudorandom binary sequences (PRBS) of duration $2^{31}-1$. Polarization-division multiplexing is performed by splitting the signal into two paths, delaying one path by 405 symbols, and re-combining the two de-correlated signals with a polarization beam splitter (PBS). After amplification, the signal is split into three tributaries with relative delays of 0, 1365 and 2272 symbols. The de-correlated signals are modulated onto the three orthogonal spatial modes (LP_{01}, LP_{11e}, and LP_{11o}) of a 50 km span of FMF using a free space mode multiplexer (M-MUX). Details of the M-MUX can be found in [36]. At the output of the FMF, a mode de-multiplexer (M-DEMUX) identical to the M-MUX is used to recover the signal's three spatial mode components on three parallel single-mode fibers. Following amplification by single-mode EDFAs, the recovered mode components are detected in three parallel coherent receivers where the signals are mixed with a common LO in polarization-and-phase diversity hybrids followed by photo-detectors. The baseband electrical signals are then

sampled and digitized using three synchronized sampling oscilloscopes with sampling rates of 40 GSa/s and 16 GHz bandwidth. The output symbols are recovered by offline processing.

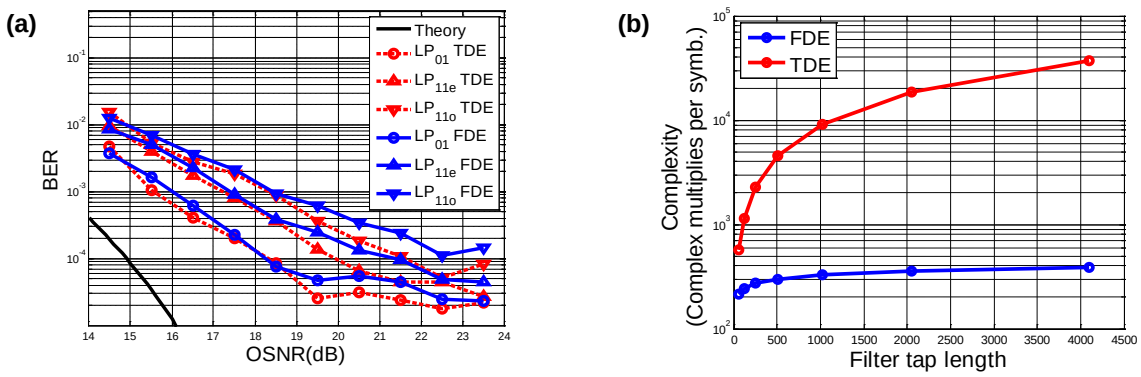

Figure 16 (a) BER vs. OSNR; (b) Complexity as a function of filter tap length

Figure 16(a) shows BER vs. OSNR using both the TDE and FDE. The BER shown for each spatial mode is the average of the two orthogonal polarizations. Independent phase estimation is performed on each spatial/polarization mode for both FDE and TDE. Similar BER performance is observed for both FDE and TDE. Figure 16(b) compares the algorithmic complexity of the FDE and TDE in complex multiplications per symbol as a function equalizer length. At an equalizer length of 256, the FDE approach reduces algorithmic complexity by a factor of 8.5 compared with the TDE. The computational savings become even larger at longer distances and larger MDG, due to the computational advantage of the FFT at longer filter lengths.

The performance of the FDE was also investigated as a function of the length of the training sequence. Figure 17(a) shows Q^2 factor vs. training length at an OSNR of 23.5 dB. A minimum of 5,000 training symbols are required to obtain initial convergence. The recovered constellations at a training length of 30,000 are shown in Figure 17(b).

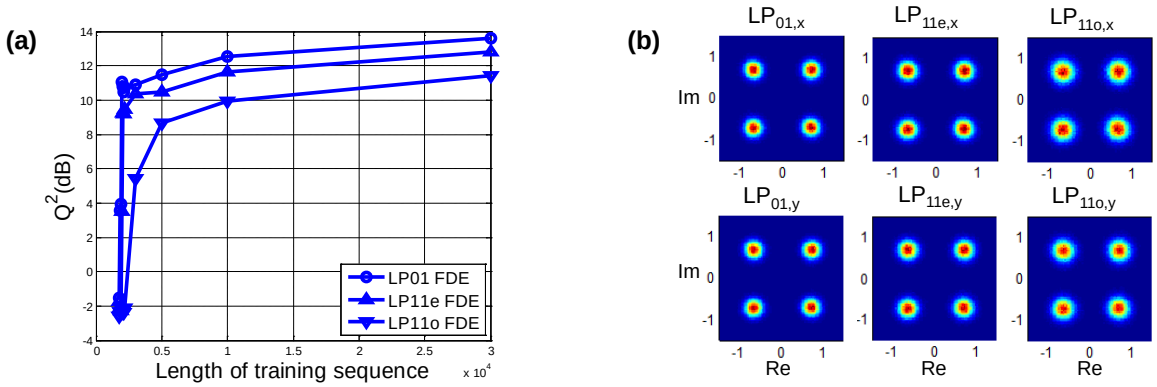

Figure 17 (a) Q^2 factor vs. training sequence length when using the FDE; (b) recovered signal constellations at a training length of 30,000

Thus far, independent frequency offset compensation and carrier phase recovery has been performed on each mode. During training, carrier phase is roughly estimated by comparing the phase of the equalizer output with the training symbols; during DD adaptation, the Viterbi-Viterbi algorithm is used. The one-shot phase estimates are then averaged over a window of length 64 to obtain a more accurate estimate of the carrier phase at that symbol. The carrier phases estimated for the six modes are shown in Figure 18.

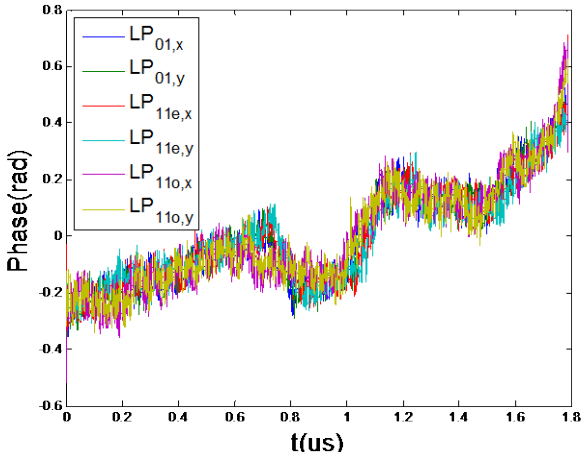

Figure 18 Phase traces independently estimated from six spatial channels

It can be seen that the phase estimates are strongly correlated. This phenomenon is due to the underlying phase noise process coming from the same transmitter laser and local oscillator (LO) source. To exploit the strong correlation, master-slave carrier recovery scheme can be applied by estimating frequency offset and carrier phase only once for a “master” mode channel; the estimated frequency offset and carrier phase is then shared with other mode channels (slaves). The DSP architecture for MIMO equalization with master-slave carrier recovery (MS-CR) is shown in Figure 19.

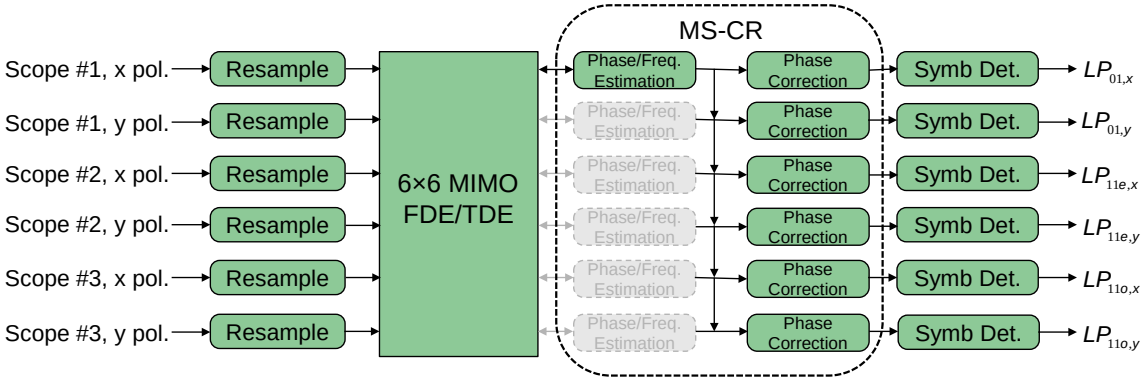

Figure 19 DSP architecture using master-slave carrier recovery scheme

MS-CR consists of two stages. The first stage uses the equalized symbols in the master mode channel to compute a carrier phase estimate. The second stage uses this estimate and de-rotates all the mode channels. MS-CR reduces the complexity of carrier recovery by the total number of modes. This complexity-reduction technique was first proposed for multi-core fiber (MCF) transmission [37]. The same concept was adapted for FMF transmission with MIMO equalization.

To verify the effectiveness of MS-CR, the BER performances of MS-CR versus conventional CR is compared in Figure 20. For the MS-CR scheme, $LP_{01,x}$ was selected as the

master channel as the fundamental mode was assumed to have the lowest BER enabling the most accurate phase estimation. The MS-CR scheme achieved similar BER as conventional CR. Small penalties are observed for LP_{11e} and LP_{11o} due to error between the actual and estimated carrier phases arising from tracking error and receiver noise.

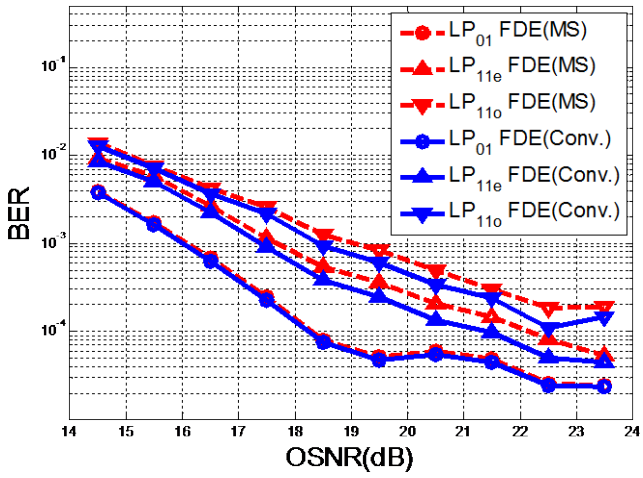

Figure 20 BER vs. OSNR compared between MS-CR and conventional CR

2.4.3 Long Distance Transmission Experiment

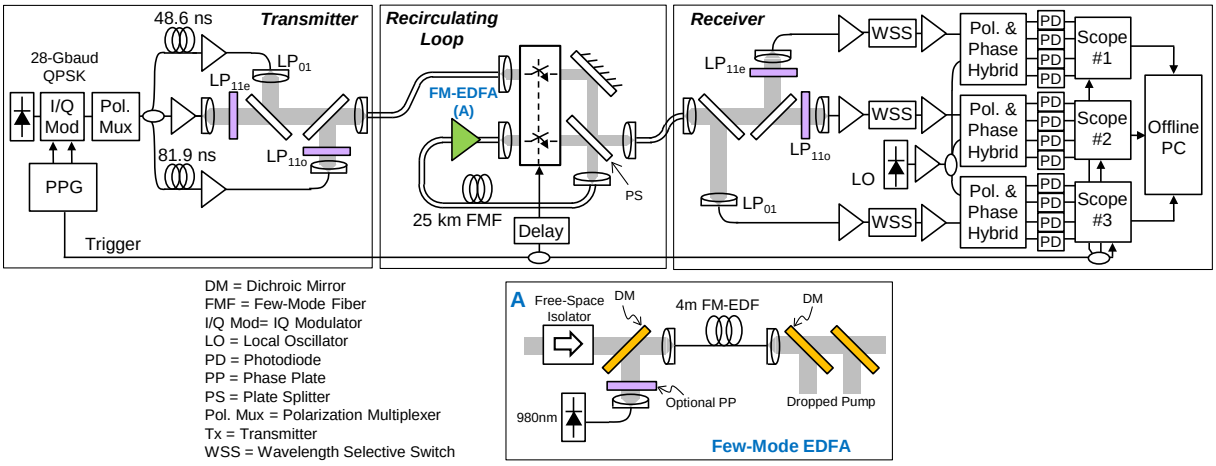

Figure 21 Experiment setup for a FMF loop experiment. Inset A: Few-mode erbium-doped fiber amplifier

The Figure 21 shows the experiment setup which is similar to [38]. At the transmitter, an external cavity laser (ECL) is used to generate CW light which is modulated by a 28GBaud QPSK signal using an I/Q modulator driven with a pseudorandom binary sequences (PRBS) of length 2^{23}-1. Polarization-division multiplexing is performed by splitting the signal into two paths, delaying one path by 605 symbols, and re-combining the two de-correlated signals with a polarization beam splitter (PBS). For mode multiplexing, phase plate based mode multiplexer (MMUX) was used as previously demonstrated in [39]. Then the combined signal light is launched into a recirculating loop [4] comprising a 25km spool of FMF with zero-DMGD wavelength at 1557.3nm.

A mechanical loop switch is used to control loading and circulation of the MDM signal. According to Figure 21, the launch beam from MMUX and the loop beam from the FM-EDFA are incident on the loop switch, which only allows one of the beams to pass at any given time. In the loading phase, the launch beam passes while the loop beam is blocked. In the circulating phase, the loop beam passes while the launch beam is blocked. The switch is controlled by the trigger signal generated by the pattern generator in transmitter. The control of the number of loops circulated is enabled by the variable electrical delay. The loss in the loop can be contributed by the 25km span of FMF (0.2dB/km), the loss of the plate splitter (4 dB insertion loss), the coupling loss from free-space beam to FMF (1.5dB for LP_{01} and 2.2dB for LP_{11}) and insertion loss of isolator and dichroic mirrors (0.5dB). The total loss per loop is 9.1dB for LP_{01} and 9.8dB for LP_{11}.

The transmission channel centered at this wavelength is selected to minimize the impulse response spread of the channel. To compensate losses of all the modes in the loop and facilitate

mode dependent gain (MDG) equalization, a few-mode EDFA with a ring shaped doping profile is used. At the receiver, mode components of MDM signals are extracted by a mode de-multiplexer (MDMUX). Following by 3 coherent receivers, finally, the intra-dyne electrical signals are sampled and digitized by three synchronized real time scopes. The captured data are then sent to offline DSP to do 6×6 MIMO equalization.

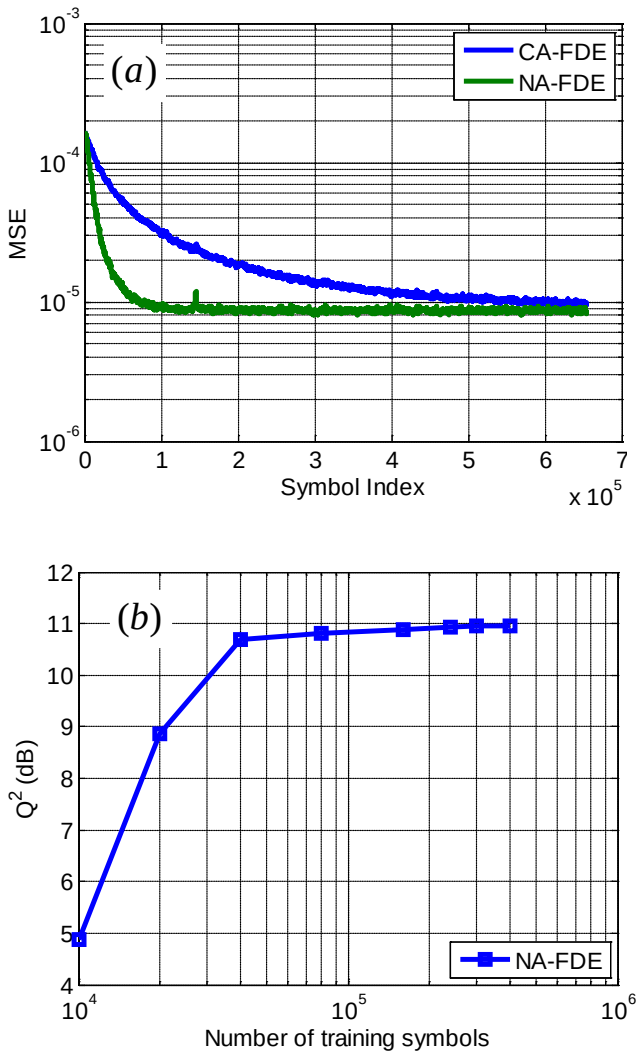

Figure 22 (a) MSE vs. symbol index for 600km FMF transmission (b) Q^2 Vs. length of training sequence for NA-FDE after 1,000-km FMF transmission

The convergence speed of conventional adaptive FDE (CA-FDE) is first compared with normalized adaptive FDE (NA-FDE). NA-FDE was first proposed for MDM transmission in [40]. Since the convergence speed of a given frequency bin of the FDE is determined by the step size $\mu(k)$ and the average signal power $P(k)$ in that bin, for signals with non-flat spectrum such as single-carrier modulation with non-return-to-zero (NRZ) pulses, different frequencies have different rates of convergence. In NA-FDE, a normalized step size $\mu(k) = \alpha / P(k)$ is used to ensure that the FDE converges uniformly across all frequencies, resulting in faster overall convergence. Figure 22(a) shows the learning curves of NA-FDE and CA-FDE after 600-km transmission. An equalizer length of 1,024 taps was used in both cases, while the step sizes for NA-FDE and CA-FDE were selected so they have the same steady-state performance after initial convergence. It is observed that NA-FDE converges six times faster compared with CA-FDE at a mean square error (MSE) of 10^{-5}. Figure 22(b) shows system performance versus the number of training symbols used for initial convergence of the NA-FDE. It is observed that a training sequence length of ~4×10^4 symbols is required after 1,000-km transmission.

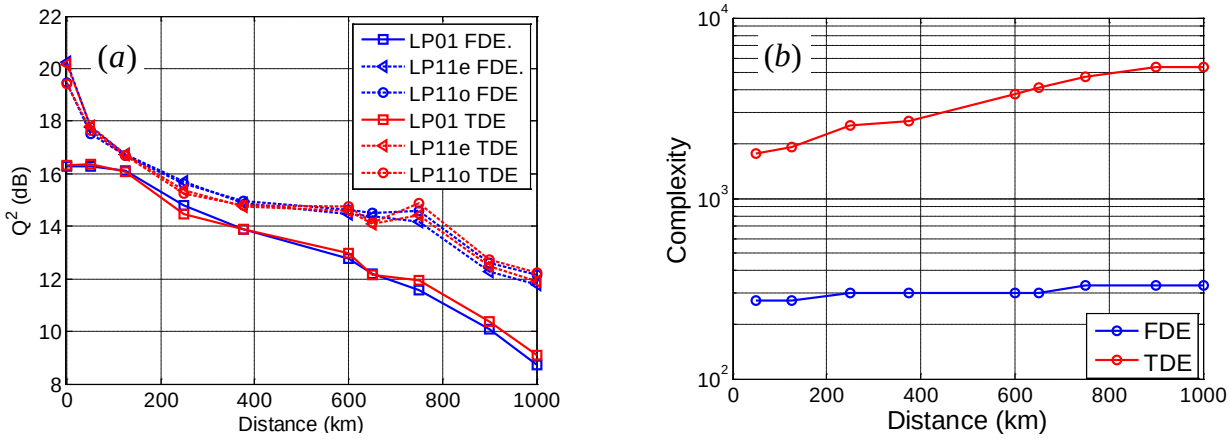

Figure 23 Comparison between FDE and TDE: (a) Q^2 vs. Distance (b) Complexity vs. Distance

Figure 23 compares the performances of FDE and TDE as the transmission distance was swept from 0 to 1,000 km. For fair comparison, the same equalizer length (1,024) and the same normalized step-size ware used for each scheme. A training sequence of 1.6×10^5 symbols was used for initial convergence of both the TDE and FDE, as according to Figure 22(b), the resulting Q^2-penalty is only 0.1 dB for the NA-FDE. Following initial convergence, the equalizers were switched to decision-directed adaptation. For Q^2 measurement, the last 4.95×10^5 symbols of each data set were used. It is observed that both TDE and FDE give similar performance. The algorithmic complexity of each scheme was computed as [41], and Figure 23(b) compares the complexity of the TDE and FDE vs. distance. The equalizer length required for TDE is defined as that needed to contain 95% of the power of the channel's impulse response [42]. Since FDE requires the use of overlap-and-save [32] as well as an FFT size equal to a power of two, the required TDE length was doubled and rounded to the next highest power of two to obtain the FDE block length. It is observed that after 1,000km, the use of FDE can reduce algorithmic complexity by a factor of 16.2.

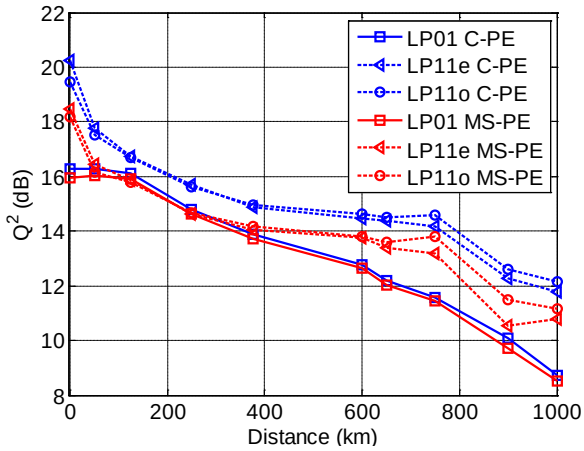

Figure 24 Comparison between C-PE and MS-PE: Q^2 vs. Distance

To further reduce the DSP complexity, master-slave phase estimation (MS-PE) can be used [22]. Figure 24 shows the system performances obtained using MS-PE and using conventional phase estimation (C-PE). For C-PE, the phase noises of each spatial channel are estimated independently, while for MS-PE, the $LP_{01,x}$ mode was selected as the master mode, and the phase noise estimated for $LP_{01,x}$ was used to compensate all the other modes [22]. The Q^2-penalty of using MS-PE is 0.7 dB after 1,000-km transmission, and is mainly caused by the de-correlation delays used at the transmitter's MMUX, which results in timing offset between the laser phase noises modulating each of the six spatial/polarization modes. It's expected that in a real MDM system, the penalty of MS-PE can be avoided.

2.5 FDE for fundamental mode transmission in FMF

While FDE is applied in the scenario of MDM system it can also be used in fundamental mode transmission (FMT) in FMF. Although FMT exploits only fundamental mode as the transmission channel in FMF, with a much larger effective area, nonlinear impairments in FMF transmission systems are reduced in comparison with SMF transmission, enabling higher-capacity for long-haul transmission. Moreover, FMT system don't need mode MUX/DEMUX and FM amplifier as MDM required. Therefore, FMT can be seen as a promising intermediate phase towards a final MDM system.

Due to the multimode nature of the FMF, one of the main impairments of FMT is multi-path interference (MPI) [43]. To reduce MPI, several optical solutions have been proposed and demonstrated. Center launch into the FMF has been shown to be able to selectively excite fundamental mode. Also, the FMF can be designed to support only two mode groups and provide

a large enough effective index difference between the two mode groups to suppress inter-mode coupling. However, those constraints on FMF design eventually limit the effective area of FMF.

In this section, instead of suppressing inter-mode coupling using pure optical techniques, MPI is compensated using DSP-based adaptive equalization in the electronic domain at the receiver. Instead of using equalizer matrix in MDM system, as a particular case, FMT only need to apply a single equalizer. This approach enables more flexibility in fiber design to allow a larger number of modes and thus larger effective areas. DSP can also track the temporal variation of the fiber and adaptively optimize its performance to improve system robustness. In this section, the results for FMT using both TDE and FDE are shown in simulation as well experiment.

2.5.1 Simulation

To evaluate the performance of the proposed FDE method in long-haul FMF transmission systems, long-distance FMF transmission with a span length of 100km was simulated using multi-section field propagation model. Mode scattering factor (MSC) defined in [33] represents the strength of inter-mode coupling. In the simulation, MSC was chosen to be -30dB/km, which is slightly higher than -34.4dB/km for the FMF used in [34], to demonstrate the capability of MPI cancelation using FDE. The loss and dispersion coefficient for both modes are 0.2dB/km and 18ps/nm/km respectively [12]. The DMGD is chosen to be 27ps/km which equals to that of the FMF used in [12]. The inline amplifier is assumed to compensate loss of the LP_{01} mode while LP_{11} mode receives no modal gain. The noise figure of the amplifier is set to be 5dB. No fundamental mode filter is applied either in the middle of each span or in front of the amplifier. Mode coupling is assumed to be only contributed by distributed mode coupling. Splicing induced

mode coupling or loss is neglected based on previous experimental results [7, 8]. A QPSK coherent transmission system with 28 Gbaud symbol rate is simulated.

For multi-span FMF transmission, the total DMGD of the link is multiple times of single span. In MDM transmission, the tap length of the equalizer has to exceed the total MGD requiring thousands of taps. In the context of FMT transmission, the relation between required length of equalizer and DMGD is first studied.

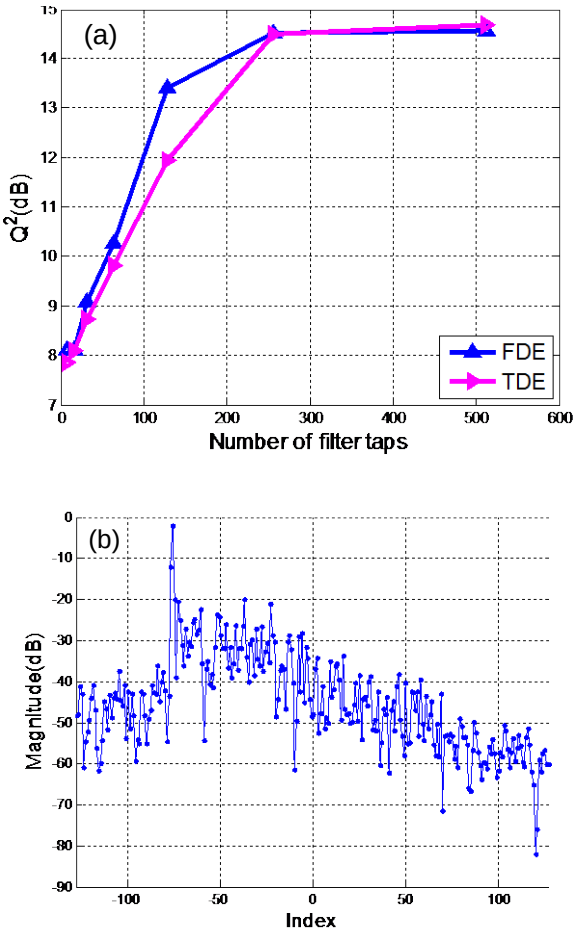

Figure 25 (a) Q^2 factor Vs. the number of total filter taps (b) Magnitude of sub-filter tap weights for 30×100km FMF transmission link at OSNR of 17dB

Figure 25(a) plots Q^2 factor as a function of equalizer tap length for a 30×100km transmission at OSNR=17dB. The tap number is chosen to be power of 2 for the sake of ease of FFT. The Q^2 factor starts to converge when the tap number increases to 256. This filter length in time (4.6ns) is just slightly larger than single span DMGD (2.7ns) but much smaller than the total DMGD of the link (81 ns). The result suggests that for FMT transmission, the minimum required filter length equals to single span DMGD but not the total DMGD of the link. It is straightforward to understand this phenomenon from the nature of MPI. For simplicity, the mode coupling process is assumed to be modeled as collection of discrete random coupling events with separation distance equal to the coherent length of the fiber. For a two mode fiber, the path of a MPI signal is of the form "$LP_{01} \rightarrow LP_{11} \rightarrow \ldots \rightarrow LP_{01}$," with an even number of coupling events. Since mode scattering factor normally is very small, the MPIs induced by more than 2 coupling events are negligible. If only the "$LP_{01} \rightarrow LP_{11} \rightarrow LP_{01}$" case is considered, the relative delay between MPI components and the main signal which stays in LP_{01} depends on the distance between 2 coupling locations. During the section between couplings, MPI component propagates in LP_{11} mode. If the coupling distance is larger than the span length, interference signal goes through an amplifier in the LP_{11} mode, which has zero modal gain. Therefore, only MPI components with a pair of couplings inside a single span could survive at the end of the link. Indeed, the assumption is verified also as shown in Figure 25(b), which plots filter weights of a sub-filter for the odd samples. Magnitude less than -30dB is observed for those taps with index larger than 0. It indicates that intensity of MPI with group delay larger than DMGD of a single span is infinitesimal.

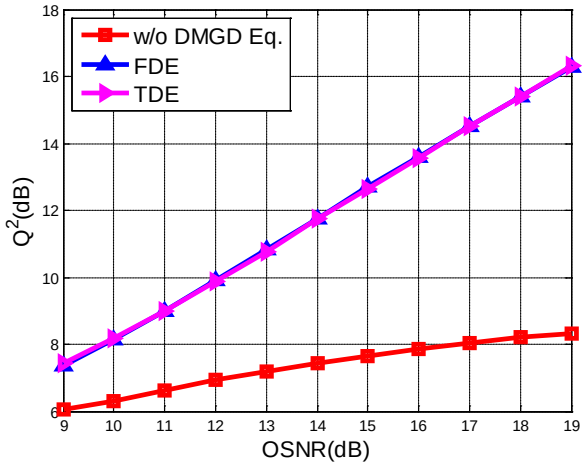

Figure 26 Q^2 factor Vs. OSNR for 30×100km transmission

Long-haul transmission simulation results are shown in Figure 26 and Figure 27. Simulations for 30×100km transmission at different OSNR levels were performed. Figure 26 illustrates the result curve. The performance improvement due to adaptive DMGD/MPI equalization grows as OSNR increases, as shown in Figure 26. Figure 27 demonstrates Q^2 factor as a function of distance ranging from 100km to 5000km. Noise loading at the receiver was used to fix the OSNR at 17dB. Without MGD equalization, system performance degrades rapidly as the transmission distance increases due to accumulated MPIs. With equalization, the performance increases as much as 7 dB in terms of Q^2 factor. For all distance, both TDE and FDE have total 256 taps. At the same performance, FDE saves 88.7% computational load compared to TDE.

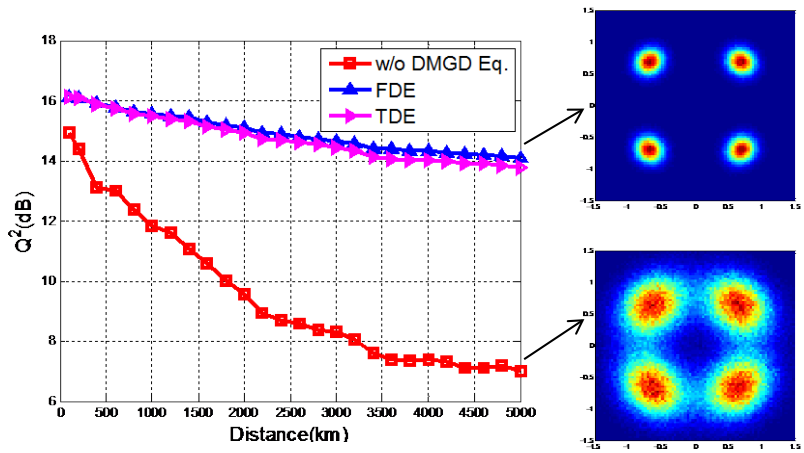

Figure 27 Q^2 factor Vs. distance and the constellation diagrams for two Q^2 values are also shown on the right hand side

2.5.2 Transmission Experiment

To experimentally demonstrate FDE, a 1 km step-index few-mode fiber with a core diameter of 13.1μm was used. The FMF effectively guides 2 spatial mode groups, LP_{01} and LP_{11} at 1550nm. The effective area of the fiber is 113μm^2. Although only single span transmission was performed, according to section 2.5.1, for FDE or TDE, multi-span transmission can be compensated using equalizer with the same filter length as that for a single span.

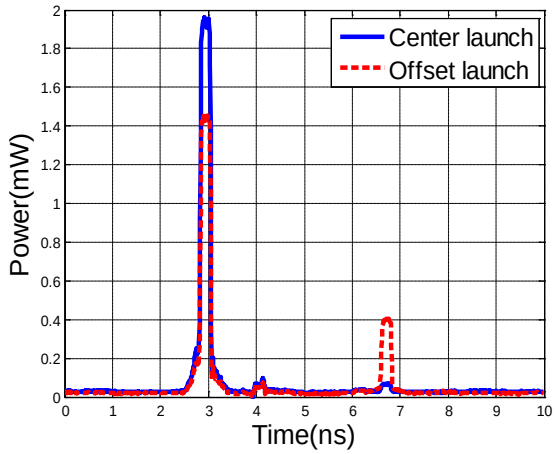

Figure 28 Pulse waveform measured at the output of the FMF at 1550nm

The fiber is first characterized by measuring the impulse response which is shown in Figure 28. A pulse train at a repetition period of 8 *ns* is generated by modulating the amplitude of the continuous wave (CW) light from an external cavity laser (ECL). The pulse width is 200ps. The pulsed light is then butt coupled from a single-mode fiber (SMF) into the FMF. After 1km transmission, the output light is coupled back into a SMF which is connected with a sampling oscilloscope. When the position of SMF at the excitation stage is aligned with the center of the FMF, only one pulse is found in the period. It confirms again that mode coupling at interconnection between SMF and FMF can be suppressed to a negligible level under center launching condition. Due to short distance, the temporal spread of the pulse from chromatic dispersion (CD) is fairly small. When the SMF was offset by a few microns from the center, a weak replicate pulse starts to grow due to the excitation of the LP_{11} mode. It should be noted that modal effective index difference between LP_{01} and LP_{11} is about $2x10^{-3}$ which is large enough to suppress mode coupling. The low mode coupling can be verified in the impulse response where the power level between two distinct pulses is very low. The weak hump between two pulses is caused by imperfect frequency response of the modulator driver. In addition, the DMGD can be estimated by measuring the temporal separation between the two pulses. At 1550nm, the DMGD is about 3780ps for 1km fiber which is approximately equal to a 140km span of FMF used in the mode-division multiplexing experiment of [12].

The transmission experimental setup is illustrated in Figure 29. A 10 Gbaud/s BPSK signal was generated by using an amplitude modulator and a pattern generator. Both ends of the FMF were butt-coupled with SMFs, in the same way as in the impulse response measurement. A high precision variable attenuator and a post-amplifier were used to adjust the optical signal-to-

noise ratio (OSNR) at the coherent receiver. The signal was then sent to a 90 degree hybrid followed by two photo-detectors measuring the real and imaginary parts of the complex signal. Finally, the electric waveforms were fed into a real-time oscilloscope with a 40GHz sampling rate. 5×10^5 samples were then recorded and processed offline.

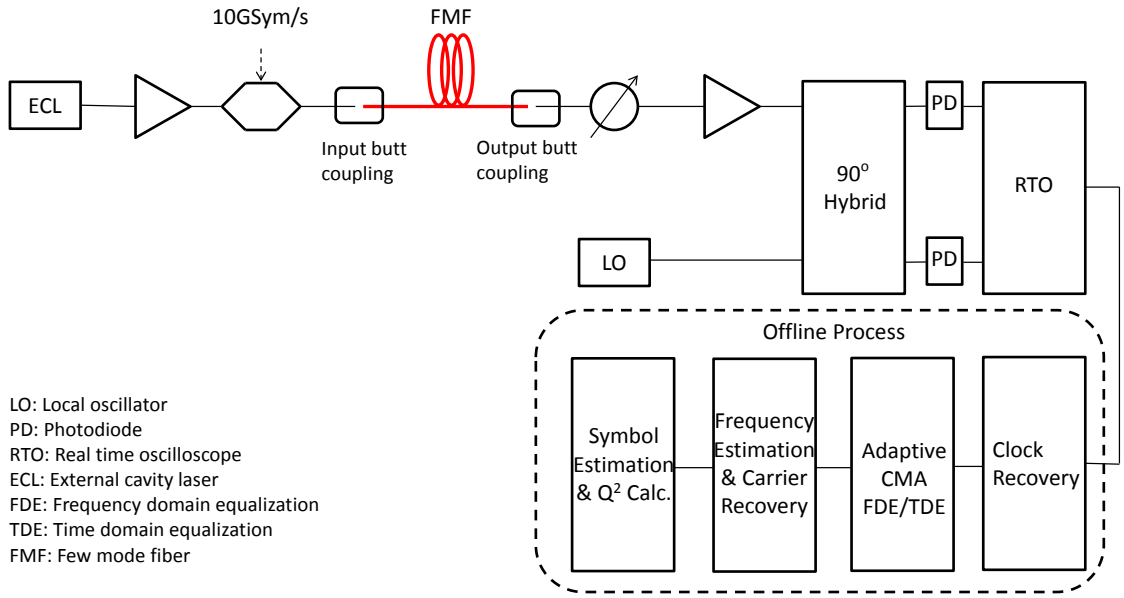

Figure 29 Transmission experiment setup

As in Figure 28, due to the relatively short transmission distance and low inter-mode coupling, distributed mode coupling are negligible in the fiber. To emulate multipath interference, the SMF was intentionally offset several microns to excite both LP_{01} and LP_{11} modes. The offset launch condition is equivalent to a discrete mode coupling at the beginning of the FMF. At the output end of FMF, the FMF-SMF butt coupling was also misaligned to receive powers from both the LP_{01} and LP_{11} modes. In offline DSP, both adaptive TDE and FDE were applied after clock recovery to compare the performance as well as efficiency of these two approaches. In order to compensate DMGD, the equalizers with a total tap length of 128 were used for both

TDE and FDE. Due to the fact that the symbol rate for experiment is lower than that in the simulation, the total tap length is half that in the simulation. Figure 30 shows Q^2 factor as a function of OSNR at the receiver. For back-to-back measurements, center launch and offset launch without DMGD equalization, only a 16 taps adaptive finite impulse response (FIR) filter was applied to equalize the CD or other impairments such as the frequency response of modulator driver and real time oscilloscope (RTO). Due to MPI, offset launch suffered high penalty compared to center launch case. At low OSNR, the performance of offset launching with equalization is approximately equal to center launching which verifies that both TDE and FDE effectively reduced the impact of MPI. Moreover, according to equation (12,17), the computational complexity of FDE is only 20% of TDE.

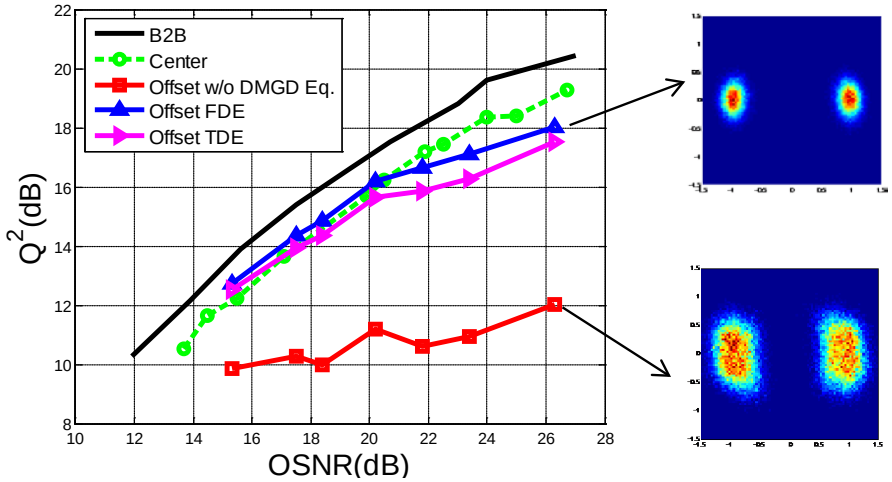

Figure 30 Q^2 Vs OSNR and the constellation diagrams for two Q^2 values are also shown on the right hand side

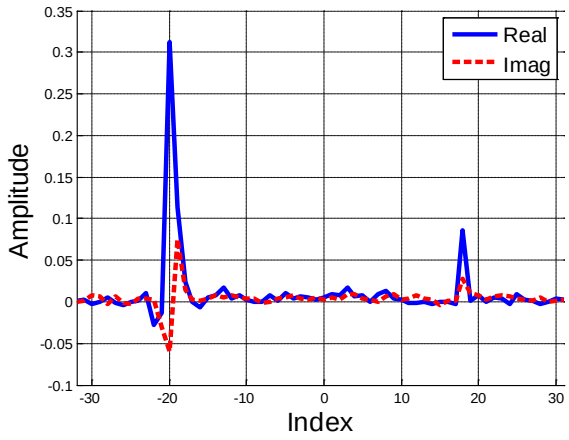

Figure 31 Typical sub-filter (odd) tap weights for FDE

In Figure 31, the complex values of a frequency domain sub-filter tap weights are plotted in the time domain. It can be observed that two distinct peaks which agree well with the impulse response measured in Figure 28 under offset launching condition. The left main peak corresponds to the signal launched into LP_{01} mode while the right weak peak relates to signal coupled to LP_{11} mode at the beginning of the fiber. Two signal components propagate at different group velocities. The temporal separation between two dominant peaks (~3800ps) is very close to the DMGD measured previously.

2.6 Conclusion

Adaptive FDE has been proposed and demonstrated to mitigate multimode interference in MDM as well as FMT system. FDE can reduce algorithmic complexity significantly compared to conventional TDE while maintaining similar performance. Master-slave carrier recovery scheme is also proposed to further simplify the algorithm.

CHAPTER 3 MODE-DIVISION MULTIPLEXED TRANSMISSION IN DIFFERENCIAL GROUP DELAY COMPENSATED FIBER LINK

3.1 Introduction

Due to mode coupling and differential mode group delay (DMGD), complicated multiple-input-multiple-output (MIMO) equalizer is required in the coherent receiver to cancel the multimode interference. To reduce the complexity of MIMO equalizer, four main approaches have been proposed. The first approach uses computational efficient algorithm, frequency domain equalization to save number of multiplications per symbol as described in chapter 2. By using FDE, the algorithmic complexity of the equalizer scales logarithmically with the mode group delay (MGD) instead of linearly using time domain equalization. However, for fiber link whose total MGD is large, FDE still requires long memory length therefore the hardware complexity of FDE could be high. The second approach is to design and fabricate a fiber with ultra-low DMGD. Although, low DMGD fiber which can guide two LP modes has been reported, for FMF which can guide 4 LP modes or more, ultra-low DMGD is difficult to be achieved so far. The third approach is to make the fiber in strong coupled regime. According to [44], strong mode coupling could help to reducing the channel impulse response spread (CIRS), or required tap length (RTL) of the equalizer. Due to effective index difference between different modes, FMFs are normally weakly coupled. To intentionally enhance mode coupling, artificial perturbations have to be applied on the fiber link. As in [42], off-center splicing was proposed to induce mode coupling. Nevertheless, the perturbed splicing introduces mode dependent loss which degrades the system performance. The fourth approach is using DMGD compensated (DMGDC) fiber [15, 45, 46]. In DMGDC fiber link, two types of fibers are spliced together.

They are: P-type whose DMGD is positive and N-type whose DMGD is negative. By center splicing pairs of two types of FMF, the aggregate MGD can be achieved to be very low. So far, DMGDC fiber which can guide 4 LP modes has been demonstrated [45]. If random mode coupling can be neglected, the CIRS equals to aggregate MGD which approaches to zero in DMGDC link. However, under weakly mode coupling, the CIRS could be much larger [47]. So far, no quantitative analyze on CIRS of DMGDC link is reported. In this chapter, the required equalizer length for DMGDC link with weak mode coupling is investigated analytically and numerically.

3.2 Theory

3.2.1 DMGD compensated fiber link

For a few-mode fiber which can guide N LP modes, different modes propagate in different group velocity resulting different group delays. The DMGD for ith mode can be defined as

$$\Delta\tau_i = \tau_i - \frac{1}{N}\sum_{j=1}^{N}\tau_j \qquad (18)$$

where τ_i is the mode group delay of i-th mode ($i = 1,2\ldots N$). Therefore, the DMGD $\Delta\tau_i$ is the difference between τ_i and the average MGD of all the modes.

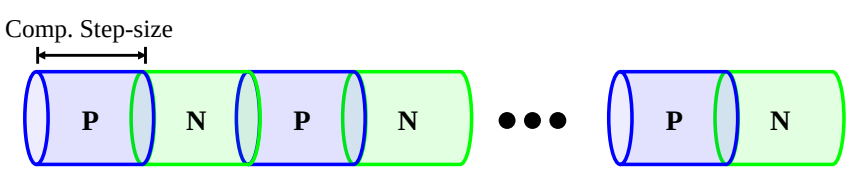

Figure 32 A single span of DMGDC fiber

A DMGDC link comprises 2 types of FMF: P-type and N-type. The DMGD of LP_{01} is positive for P-type fiber while negative for N-type fiber. In a single span of DMGDC link, two types of FMFs are spliced alternatively as shown in Figure 32. The adjacent two FMF sections are a compensation pair which is the building block of DMGDC span. In zero residual DMGD case, the accumulate DMGDs of these two sections satisfy following equation.

$$\Delta\tau_i^{(P)} L_P = -\Delta\tau_i^{(N)} L_N \tag{19}$$

where $\Delta\tau_i^{(P)}$ and $\Delta\tau_i^{(N)}$ are DMGDs of ith mode of P-type and N-type FMF respectively; L_P and L_N are the lengths of P-type and N-type fiber. If $\Delta\tau_i^{(P)} = -\Delta\tau_i^{(N)}$, L_P equals to L_N which can be defined as compensation step-size. The chapter considers only zero residual DMGD link.

3.2.2 Impulse Response of DMGD uncompensated link

A FMF link which has D spatial degrees of freedom can be characterized using a $D \times D$ matrix $\overline{\overline{H}}$. Each element of the matrix (h_{ij}) is an impulse response which lasts a certain period of time. The input-output relationship can be expressed as following:

$$y_j = \sum_{i=1}^{D} h_{ij} * x_i \tag{20}$$

where x_i and y_j are ith mode of input signal and jth mode of output signal. The CIRS equals to the longest duration of h_{ij}. In case of weakly coupled FMF, the CIRS corresponds to MGD of the FMF, which can be expressed as following:

$$\Delta\tau_{MGD} = \left(\Delta\tau_s - \Delta\tau_f\right) L \tag{21}$$

where $\Delta\tau_s$ is the DMGD of the slowest mode (S mode), $\Delta\tau_f$ is the DMGD of the fastest mode (F mode) and L is the fiber length of the link. The overall DMGD is noted by $\Delta\tau = \Delta\tau_s - \Delta\tau_f$. Since group delay difference between S and F modes determines the MGD of the link, these two modes are the most critical pair to determine the equalizer size. The impulse response h_{sf} describes the linear coupling from S to F mode along the link, which includes direct mode couplings between pairs and indirect mode couplings via other modes. Due to weakly coupling assumption, indirect mode coupling is negligible compared to the direct one. Additionally, the main mode channels are assumed to be un-depleted by mode coupling [48]. Therefore, the link can be simplified to be a two mode system which is illustrated in Figure 33.

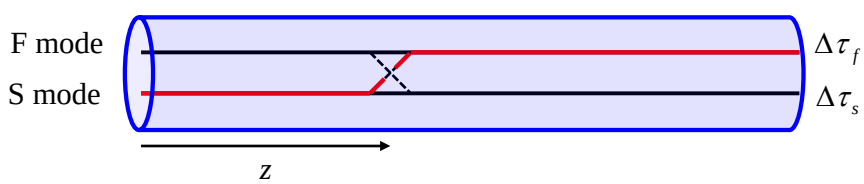

Figure 33 A single span of DMGD uncompensated fiber

Two straight lines symbolize F and S mode channels. At location z, signal of F mode is coupled to S mode with a coupling coefficient $\kappa_{sf}(z)$ where $z \in [0, L]$. The statistics of $\kappa_{sf}(z)$ is assumed to obey normal distribution with zero mean [48] and squared deviation of σ_κ^2 which equals to mode scattering coefficient (MSC) defined in [33]. The path delay of the coupling light via coupling location z can be calculated

$$\tau(z) = \Delta\tau z + \Delta\tau_f L \tag{22}$$

h_{sf} therefore can be calculated by integrating over all the coupling paths as following

$$h_{sf}(t) = \int_0^L \delta\left(t - \Delta\tau z - \Delta\tau_f L\right)\kappa_{sf}(z)\exp\left(j\Delta\beta_{sf} z + \beta_f L\right)dz$$
$$= \frac{1}{\Delta\tau}\kappa_{sf}\left(\frac{t - \Delta\tau_f L}{\Delta\tau}\right)\exp\left(j\frac{\Delta\beta_{sf}}{\Delta\tau}t - j\frac{\Delta\tau_f\beta_s - \Delta\tau_s\beta_f}{\Delta\tau}L\right) \quad (23)$$

where β_s and β_f are the propagation constants of S and F modes respectively; $\Delta\beta_{sf}$ is the β difference between them. According to the domain of $\kappa(z)$, $0 \le z \le L$, the range of t can be calculated as $\Delta\tau_f L \le t \le \Delta\tau_s L$. The required tap length (RTL) of DMGD uncompensated link, assuming oversampling rate of 2, can be expressed as following

$$N_{taps} = 2\Delta\tau L R_s \quad (24)$$

3.2.3 Impulse Response of single DMGD compensated pair

Fig. 3(a-b) shows a fiber span with one DMGD compensation pair.

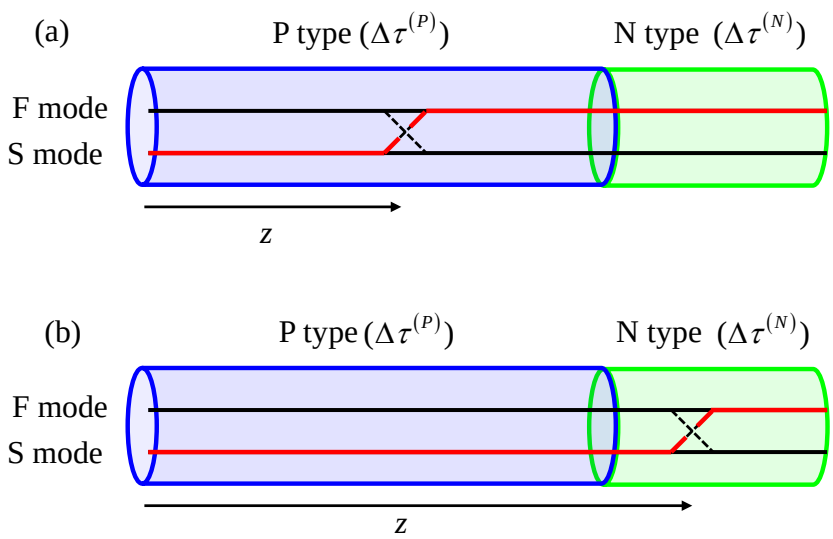

Figure 34 A single span with one DMGD compensation pair with mode coupling in (a) P type section (Case I), (b) N type section (Case II)

The impulse response h_{sf} can be calculated in two parts:

$$h_{sf}\left(t\right)=h_{sf}^{(I)}\left(t\right)+h_{sf}^{(II)}\left(t\right) \tag{25}$$

where $h_{sf}^{(I)}\left(t\right)$ and $h_{sf}^{(II)}\left(t\right)$ are the impulse responses due to mode coupling in P-type section and N-type section respectively. Following the similar procedure as the derivation of equation (23), $h_{sf}^{(I)}\left(t\right)$ and $h_{sf}^{(II)}\left(t\right)$ can be expressed as following integrals.

$$h_{hl}^{(I)}\left(t\right)=\int_{0}^{L_P}\delta\left(t-\Delta\tau^{(P)}z\right)\kappa_{sf}^{(P)}\left(z\right)\exp\left(j\Delta\beta_{sf}^{(P)}z+j\left(\beta_f^{(P)}L_p+\beta_s^{(N)}L_N\right)\right)dz \tag{26}$$

$$\begin{aligned}h_{sf}^{(II)}\left(t\right)=&\int_{L_P}^{L_P+L_N}\delta\left(t-\Delta\tau^{(N)}\left(z-L_N-L_P\right)\right)\kappa_{sf}^{(N)}\left(z\right)\\&\exp\left[j\Delta\beta_{hl}^{(N)}z+j\left(\left(\beta_h^{(P)}-\Delta\beta_{hl}^{(N)}\right)L_p+\beta_l^{(N)}L_N\right)\right]dz\end{aligned} \tag{27}$$

where $\Delta\tau^{(\bullet)}$ is overall DMGD for P-type or N-type FMF, $\beta_s^{(\bullet)}$ and $\beta_f^{(\bullet)}$ are propagation constants for slowest and fastest mode in P-type or N-type FMF respectively, $\Delta\beta_{sf}^{(\bullet)}$ is the difference between $\beta_s^{(\bullet)}$ and $\beta_f^{(\bullet)}$. h_{hl} can therefore be derived by substituting (26，27) to (25).

$$\begin{aligned}h_{sf}\left(t\right)=&\frac{1}{\Delta\tau^{(P)}}\kappa_{sf}^{(P)}\left(\frac{t}{\Delta\tau^{(P)}}\right)\exp\left(j\Delta\beta_{sf}^{(P)}\frac{t}{\Delta\tau^{(P)}}+j\left(\beta_s^{(P)}L_P+\beta_f^{(N)}L_N\right)\right)\\&+\frac{1}{\Delta\tau^{(N)}}\kappa_{sf}^{(N)}\left(L_P+L_N+\frac{t}{\Delta\tau^{(N)}}\right)\exp\left[\begin{array}{l}j\Delta\beta_{sf}^{(N)}\frac{t}{\Delta\tau^{(N)}}\cdots\\+j\left(\beta_s^{(P)}-\Delta\beta_{sf}^{(N)}L_P\right)+\beta_f^{(N)}L_N\end{array}\right]\end{aligned} \tag{28}$$

The non-zero temporal range of h_{sf} can be find to be $0\le t\le\Delta\tau^{(P)}L_P$. Thus the length of h_{hl} equals to MGD of P-type fiber section, $\Delta\tau_{MGD}^{(P)}$ which equals to $-\Delta\tau_{MGD}^{(N)}$. Similarly, h_{fs} can be derived and its non-zero temporal range is $-\Delta\tau^{(P)}L_P\le t\le 0$. Therefore, the overall lasting range of interaction between S and F modes is $\left[-\Delta\tau_{MGD}^{(P)},\Delta\tau_{MGD}^{(P)}\right]$. The CIRS thus equals to $2\Delta\tau_{MGD}^{(P)}$.

3.2.4 Impulse Response of DMGD compensated link

A DMGD compensation link contains multiple spans and each span comprises multiple compensation pairs as shown in Figure 32. Since h_{sf} can be calculated as a sum of the interference from all the direct coupling paths from S mode to F mode, h_{sf} can be divided into *K* components where *K* is the total number of compensation pairs in the link as in equation (29).

$$h_{sf}(t) = \sum_{k=1}^{K} h_{sf}^{(k)}(t) \tag{29}$$

Each component represents interference from all the couplings in one compensation pair. Due to weakly coupling assumption, only one coupling event counts in any possible paths from S mode at the transmitter to F mode at the receiver. Since the mode group delay is compensated periodically, the path delay of the coupling light via coupling location $z = (k-1)(L_P + L_N) + \Delta z$ $(k = 1, 2 \ldots K)$ can be calculated as

$$\tau\left((k-1)(L_P + L_N) + \Delta z\right) = \tau(\Delta z) \tag{30}$$

Therefore, the problem is simplified to the case of single DMGD compensation pair. The CIRS of the DMGD compensated link is the same as a single compensation pair. If oversampling rate 2 is assumed, the RTL for time domain equalization can be calculated as following

$$N_{taps} = 4\Delta\tau^{(P)} L_P R_s \tag{31}$$

According to equation (31), the RTL depends on MGD of a section of P-type fiber rather than the MGD of the whole link. It indicates that by using short compensation step-size, the RTL could be very low even with weakly random mode coupling.

3.3 Simulation

3.3.1 Fiber Design and Simulation Setup

For simplicity, P-type and N-type FMFs which can guide two LP modes are designed and simulated. In P-type fiber, LP_{01} mode which is the faster mode is noted as mode 1. LP_{11} is the slower mode numbered as mode 2. Trench assisted graded index profile is used as in [49]. By adjusting power index α, the DMGDs can be tuned to be 100 ps/km for P-type FMF and -100ps/km for N-type across the C-band. The index profile as well as design parameters are shown in Figure 35. The effective index differences between two LP modes are 2.9×10^{-3} and the chromatic dispersion coefficients are 21 ps/nm/km for both types of fiber.

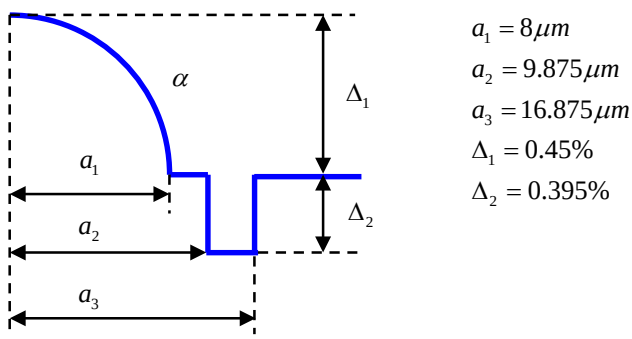

Figure 35 Trench assisted graded index profile of P type (α = 2.079) or N type (α = 2.196)

Multi-section field propagation model was used to simulate two-mode transmission in FMF [33]. The section length was set to be 200m as same as [49]. For other section lengths such as 100m or 500m, negligible difference was observed. MSC was set to be -35dB/km which is similar as the fiber used in [34](-34.4dB/km). Losses were 0.2dB/km for both modes. No crosstalk was assumed from mode MUX/DEMUX or splicing.

The simulation setup is similar to [41]. In the transmitter, two independent 28 Gbaud QPSK signal streams are generated and multiplexed into two LP modes of FMF link comprising 10 spans. Single span length is 128km. Each span is constructed by splicing multiple compensation fiber pairs. At the end of each span, an ideal multimode EDFA is used to compensate losses for both modes. At the receiver, two modes signals are detected after an ideal mode de-multiplexer and two coherent receivers. Chromatic dispersion compensation is done using static frequency domain equalizer before adaptive equalization. TDE is used to equalize the signal and estimate the impulse responses of the link due to its freedom to have arbitrary tap lengths.

3.3.2 Results

To verify the analytical solution, impulse responses were numerically analyzed for DMGD compensated and uncompensated link using least mean square (LMS) method. Some typical impulse responses are shown in Figure 36.

For DMGD uncompensated link, all the 10 spans are constructed by P-type fibers whose DMGD equals to 100ps/km. As shown in Figure 36(a), impulse response h_{21} confines in center rectangular region. The width of region is 7162 tap periods which matches with the estimated width by using equation (7), 7168 tap periods. Figure 36(b-c) shows h_{21} and h_{12} for DMGDC link. The compensation step-size is set to be 64km which is a half of the span length. It is observed that the length of h_{21} and h_{12} is about 20 times shorter than uncompensated link which agrees with theoretical analysis. Figure 36(d) illustrates the impulse response of h_{11}. The center peak corresponds to the signal from the uncoupled LP_{01} path. The pedestal is due to multipath

interference which covers both $t > 0$ and $t < 0$ sides. In the model discussed in section II, the multipath interference is much smaller compared to mode crosstalk due to weakly coupling. The simplification in the analytical model can introduce error to the estimation of CIRS, particularly when MSC is high.

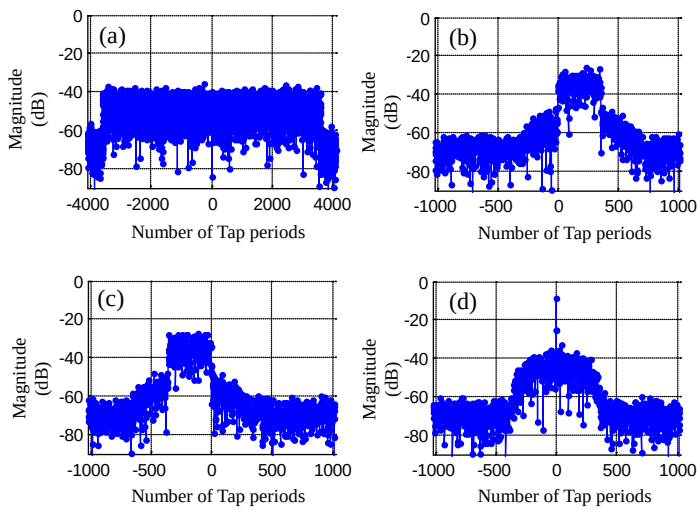

Figure 36 Magnitude of impulse response Vs. number of tap periods for (a) h_{21} of 10×128km P-type fiber link; (b) h_{21}, (c) h_{12} and (d) h_{11} of 10× (64km(P)+64km(N)) DMGDC fiber link

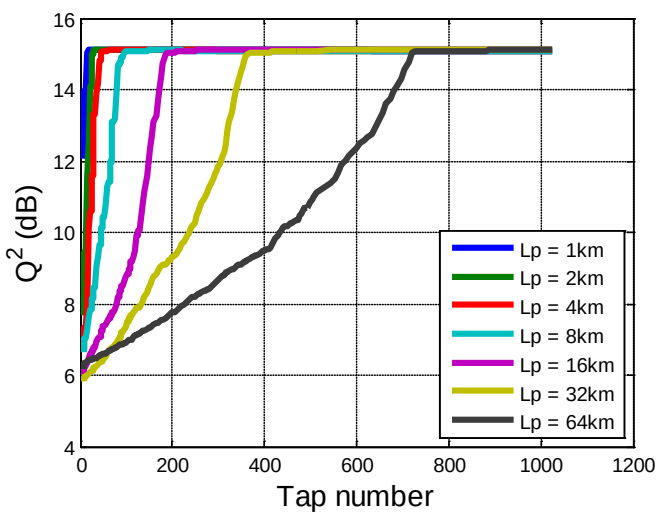

Figure 37 Q^2(dB) Vs. Tap number used in LMS equalizer when MSC equals to -35dB/km

To rigorously analyze the RTL for the link, the receiving data are processed by equalizers with various tap lengths. Thus the Q^2 factor as a function of tap length is plotted in Figure 37. As the tap length increases, more distributed mode couplings or interferences are canceled leading to higher Q^2. When the tap length exceeds the CIRS, Q^2 converges to the maximum value determined by the OSNR at the receiver. Figure 37 also shows Q^2 curves for various compensation step-size. For each curve, the RTL can be defined as the minimum tap length of the equalizer to achieve 0.1dB Q^2 penalty. Therefore, RTL as a function of compensation step-size can be plotted and shown in Figure 38 for different MSCs.

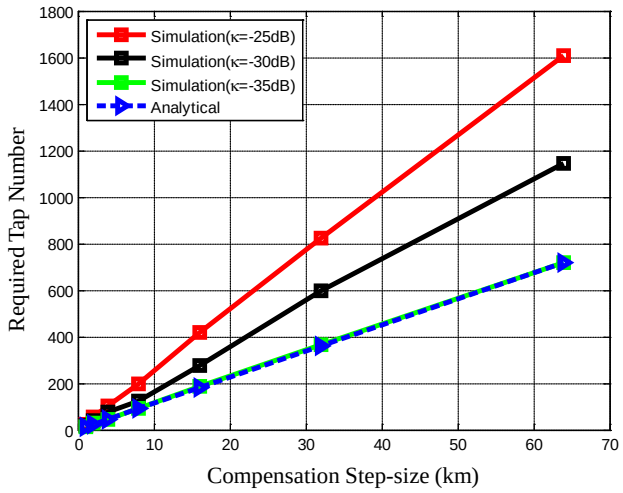

Figure 38 Required tap number Vs. compensation step-size for various MSCs

It is observed that for the case that MSC equals to -35dB/km, the numerical result agrees with analytical estimation well. According to Figure 38, RTL can be reduced by decreasing compensation step-size. When compensation step-size equals to 1km, the RTL is only 14 taps which is 1/512 of the one for uncompensated link when MSC equals to -35dB/km. As MSC increases, the analytical estimated RTL is below the actual one. Due to stronger random coupling, indirect coupling cannot be neglected any more. For MSC equals to -30dB/km or -25dB/km, the

numerical result shows that the RTL is still linear proportional to compensation step-size while slopes of the curves are larger when MSC is larger.

3.4 Conclusion

The equalizer size requirement is investigated analytically and numerically for DMGDC link with weakly random mode coupling. Differ from DMGD uncompensated counterpart, the RTL of DMGD compensated link depends only on the MGD of single P-type or N-type fiber section. Consequently, by using small compensation step-size, the RTL of DMGDC link can be two orders of magnitude shorter than the DMGD uncompensated one.

CHAPTER 4 MULTIMODE ERBIUM DOPED FIBER AMPLIFIER FOR MODE-DIVISION MULTIPLEXED TRANSMISSION

4.1 Introduction

To enable mode-division multiplexing (MDM) in MMF over long-haul distances, inline erbium-doped fiber amplifiers (EDFA) based on MMF are required [50]. The theory of multimode EDFAs (MM-EDFA) has been studied in [51]. Applications for MM-EDFAs have included high-powered lasers and free-space communications, where the multimode optical waveguide is essentially used in a "single-mode" manner, thus mode-dependent gain (MDG) is not critical [51, 52]. In MDM transmission however, careful control over MDG is necessary to overcome mode-dependent loss (MDL) in the transmission fiber, and to ensure all signal modes are launched with optimal power maximizing the total system capacity.

Mode dependent gain (MDG) is mainly determined by three factors: (a) the concentration profile of the active dopant ions, (b) the transverse intensity profile of the pump, and (c) the transverse intensity profile of the signal. In general, a signal mode whose profile is better matched to the pump intensity profile will experience higher gain. Hence, by controlling the mode content of the pump, it is possible to control MDG. The organization of this chapter is as follows. In Section 4.2, the theory of MM-EDFAs is reviewed. In Section 4.3, simulation results are presented for a step-index "two-mode fiber," demonstrating the feasibility of MDG control by tuning the mode content of the pump. The dependence of MDG on the excitation of unwanted modes and mode coupling within the EDF is also explored.

4.2 Theory and Model

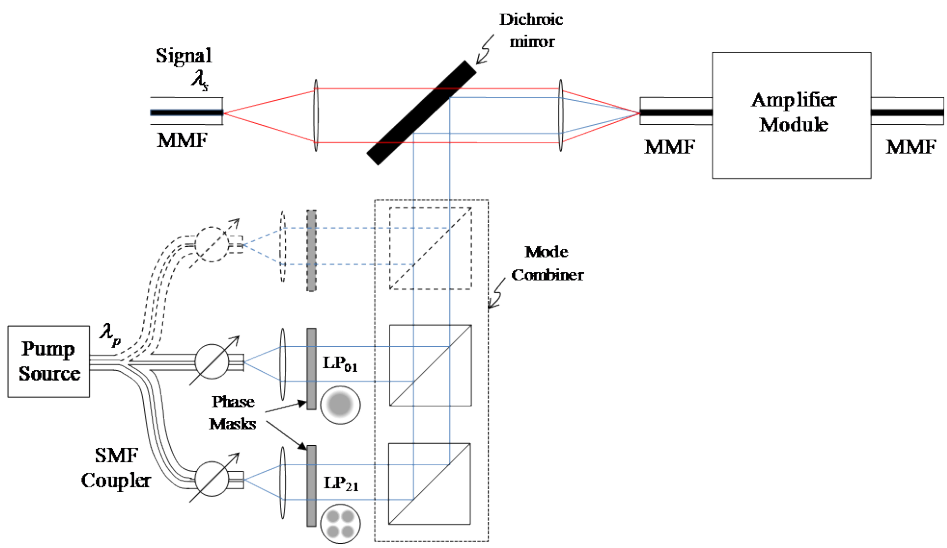

Figure 39: Schematic diagram of an MM-EDFA

A schematic diagram of a MM-EDFA is shown in Figure 39. To generate the desired pump intensity profile, the pump source is splitted into *N* paths, and use mode converters to transform the spatial mode of the pump source into the *N* spatial modes of the MMF. The variable attenuators enable *N*-degree control over the mode content of the pump, and thus the MDG of the device. The pump modes are spatially combined with the signal, which are injected into the erbium-doped MMF. In the paper, the erbium-doped MMF is assumed to have the profile shown in Figure 40, where the core has radius r_c, and a region of the core for which $r < a \le r_c$ is doped with Erbium atoms at a concentration of $N_0(r,\varphi)$.

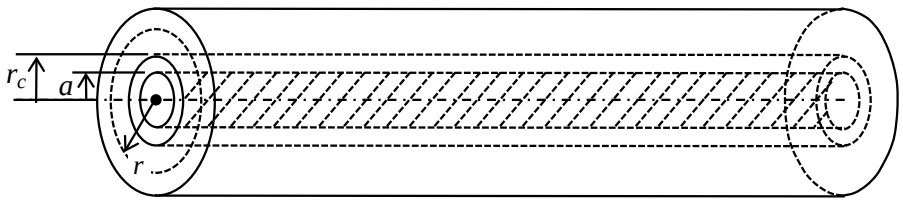

Figure 40: Multimode Erbium-doped fiber amplifier

The operation of a multimode fiber amplifier is described by coupled differential equations involving: (i) evolution of the intensities of the various signal and pump modes along the amplifying medium, and (ii) population inversion along the amplifying medium [51]. In contrast to a single-mode EDFA, the transverse intensity distributions have to be taken into account in a multimode EDFA. Both signal and pump are assumed to be co-propagating. Let $\Gamma_{s,i}(r,\varphi)$ and $\Gamma_{p,j}(r,\varphi)$ be the normalized intensity patterns of the *i*-th signal mode and *j*-th pump mode of the EDF, respectively; and let $P_{s,i}$ and $P_{p,j}$ be their respective power. The erbium-doped fiber (EDF) can be assumed as a quasi-three-level system at 980 nm pumping, and let $N_1(r,\varphi,z)$ and $N_2(r,\varphi,z)$ with $N_1(r,\varphi,z)+N_2(r,\varphi,z)=N_0(r,\varphi)$ be the population densities of Erbium atoms in the lower and upper levels at position (r,φ,z). Loss is assumed negligible in the EDF. It can be shown that the intensity evolution equations for signal and amplified spontaneous emission (ASE) in the *i*-th signal mode at the wavelength λ_s are given by:

$$\frac{dP_{s,i}}{dz}=P_{s,i}\int_0^{2\pi}\int_0^{a} r\,dr\,d\varphi\;\Gamma_{s,i}(r,\varphi)\left[N_2(r,\varphi,z)\sigma_{es,i}-N_1(r,\varphi,z)\sigma_{as,i}\right]$$
$$-\sum_{k=1}^{m_s} d_{s,i\leftrightarrow k}\left[P_{s,i}-P_{s,k}\right] \qquad (32)$$

$$\frac{dP_{ASE,i}}{dz} = P_{ASE,i}\int_0^{2\pi}\int_0^a r\,dr\,d\varphi\;\Gamma_{s,i}(r,\varphi)\left[N_2(r,\varphi,z)\sigma_{es,i} - N_1(r,\varphi,z)\sigma_{as,i}\right]$$
$$+\int_0^{2\pi}\int_0^a rdrd\phi 2\sigma_{es,i}h\nu_s\Delta\nu N_2(r,\varphi)\Gamma_{s,i}(r,\varphi) \tag{33}$$

where $\sigma_{as,i}$ and $\sigma_{es,i}$ are the absorption and emission cross-section areas at the *i*-th signal mode, $\Delta\nu$ is the equivalent amplifying bandwidth, and the $d_{s,i\leftrightarrow k}$ is coupling coefficient between signal modes [53]. In the signal propagation equation (32), the first term on the right hand side denotes net amplification due to stimulated emission, and the second term denotes power coupling between the signal modes. In the ASE propagation equation (33), the second term on the right hand side represents spontaneous emission of the excited Erbium ions; the coefficient of '2' preceding this term corresponds to two degenerate polarizations modes. The intensity evolution equation for the power in the jth pump mode at wavelength λ_p is:

$$\frac{dP_{p,j}}{dz} = -P_{p,j}\int_0^{2\pi}\int_0^a r\,dr\,d\varphi\;\Gamma_{p,j}(r,\varphi)N_1(r,\varphi,z)\sigma_{ap,j} - \sum_{k=1}^{m_p} d_{p,j\leftrightarrow k}\left[P_{p,j} - P_{p,k}\right] \tag{34}$$

Finally, the population density equations are:

$$N_1(r,\varphi,z) = \frac{\dfrac{1}{\tau} + \sum_{i=1}^{m_s}\dfrac{\left[P_{s,i} + P_{ASE,i}\right]\sigma_{es,i}\Gamma_{s,i}(r,\varphi)}{h\nu_s}}{\dfrac{1}{\tau} + \sum_{i=1}^{m_s}\dfrac{\left[P_{s,i} + P_{ASE,i}\right]\left(\sigma_{es,i} + \sigma_{as,i}\right)\Gamma_{s,i}(r,\varphi)}{h\nu_s} + \sum_{j=1}^{m_p}\dfrac{P_{p,j}\sigma_{ap,j}\Gamma_{p,j}(r,\varphi)}{h\nu_p}} N_0(r,\varphi) \tag{35}$$

$$N_2(r,\varphi,z) = \frac{\sum_{i=1}^{m_s}\dfrac{\left[P_{s,i} + P_{ASE,i}\right]\sigma_{as,i}\Gamma_{s,i}(r,\varphi)}{h\nu_s} + \sum_{j=1}^{m_p}\dfrac{P_{p,j}\sigma_{ap,j}\Gamma_{p,j}(r,\varphi)}{h\nu_p}}{\dfrac{1}{\tau} + \sum_{i=1}^{m_s}\dfrac{\left[P_{s,i} + P_{ASE,i}\right]\left(\sigma_{es,i} + \sigma_{as,i}\right)\Gamma_{s,i}(r,\varphi)}{h\nu_s} + \sum_{j=1}^{m_p}\dfrac{P_{p,j}\sigma_{ap,j}\Gamma_{p,j}(r,\varphi)}{h\nu_p}} N_0(r,\varphi) \tag{36}$$

where ν_s and ν_p are the signal and pump optical frequencies. Other symbols are listed in Table 1. Equations (32-36) can be solved by using the standard fourth-order Runge-Kutta method given initial conditions for pump and signal power [54]. Gains and noise figures for all signal modes may similarly be calculated.

Table 1: List of variables used in the coupled equations

Symbol	Definition	Symbol	Definition
$\Gamma_{s,i}(r,\varphi)$	Normalized intensity profile for *i*-th mode at λ_s	$\Gamma_{p,j}(r,\varphi)$	Normalized intensity profile for *j*-th mode at λ_p
$N_1(r,\varphi,z)$	Erbium ion population density of lower level	$N_2(r,\varphi,z)$	Erbium ion population density of upper level
$N_0(r,\varphi)$	Erbium ion doping density	h	Planck constant
$\sigma_{as,i}$	Absorption cross-section for *i*-th mode at λ_s	$\sigma_{ap,j}$	Absorption cross-section for *j*-th mode at λ_p
$\sigma_{es,i}$	Emission cross-section for *i*-th mode at λ_s	τ	Spontaneous emission lifetime for the excited state
m_s	Total number of guided modes at λ_s	m_p	Total number of guided modes at λ_p
ν_s	Optical frequency of the signal at λ_s	ν_p	Optical frequency of the pump at λ_p
$\Delta\nu$	Equivalent amplifying bandwidth	$P_{s,i}$	Power of the signal for *i*-th mode at λ_s
$P_{p,j}$	Power of the pump for *j*-th mode at λ_p	$P_{ASE,i}$	Power of ASE for *i*-th mode
$d_{s,i\leftrightarrow k}$	Mode coupling coefficient between *i*-th and *k*-th mode of the signal at λ_s	$d_{p,j\leftrightarrow k}$	Mode coupling coefficient between *j*-th and *k*-th mode of the pump at λ_p
r_c	Core radius of Erbium-doped fiber	a	Radius of uniform doping region
$\Delta G_{11s-01s}$	Mode-dependent gain (MDG): Gain of $LP_{11,s}$ minus gain of $LP_{01,s}$		

4.3 Simulation Setup

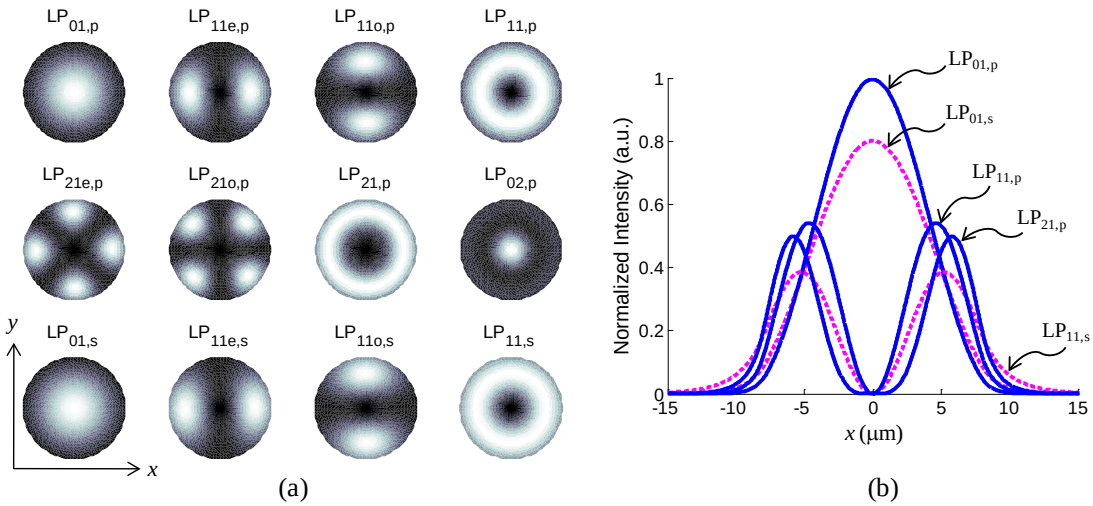

Figure 41: (a) Intensity profile of pump and signal modes, (b) normalized intensity profiles viewed along x-axis

A MM-EDFA where the EDF has step-index refractive profile is considered. The parameters of the MM-EDFA are shown in Table 2. The doped region is assumed as the same size as the core (i.e., $a = r_c$). As the normalized frequency at λ_s = 1.53 μm lies between 2.405 $< V_s <$ 3.832, the EDF supports two degenerate mode groups at this wavelength. A weakly guiding MMF is assumed where the modes are well approximated by linearly polarized (LP) modes [14]. For the remainder of this chapter, the notations $LP_{ij,s}$ and $LP_{xy,p}$ are used to denote the LP_{ij} mode at λ_s and LP_{xy} mode at λ_p, respectively. Figure 41 shows the intensity profiles of the modes, and their intensities viewed along the x-axis. For $m > 0$, the $LP_{mn,s}$ and $LP_{mn,p}$ have two spatially degenerate modes. In one of these modes, referred to as the "even" mode, intensity is maximized along the x-axis at (φ = 0); in the other mode, referred to as the "odd mode", intensity is minimized along the x-axis. All spatial modes, degenerate and non-degenerate, come with two degenerate polarization modes.

Table 2: Parameters of a MM-EDFA

Parameter	Value	Parameter	Value
$r_c\ (\mu m)$	8	$\sigma_{as,i}\ (m^2)$	5.64×10^{-25}
NA	0.1	$\sigma_{es,i}\ (m^2)$	5.71×10^{-25}
$N_0\ (m^{-3})$	1×10^{24}	$\sigma_{ap,i}\ (m^2)$	2.86×10^{-25}
$\tau\ (ms)$	10	$\sigma_{ep,i}\ (m^2)$	0
$\lambda_s\ (\mu m)$	1.53	$\lambda_P\ (\mu m)$	0.98
$L\ (m)$	30		

4.4 Modal Gain Control using Reconfigurable Multimode Pump

4.4.1 Modal gain control for non-degenerate mode

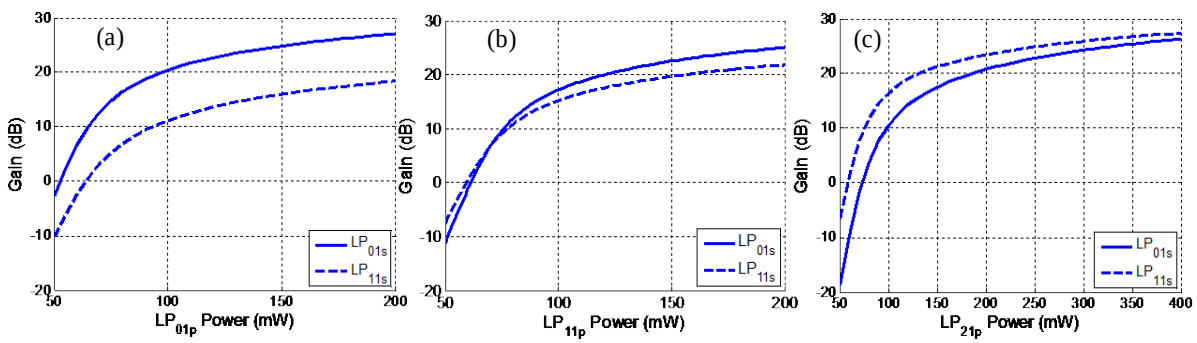

Figure 42: Modal gain of signal at 1530 nm assuming 0.05 mW power in each degenerate modes of $LP_{01,s}$ and $LP_{11,s}$, when 980-nm pump is entirely confined in (a) $LP_{01,p}$, (b) $LP_{11,p}$ and (c) $LP_{21,p}$

MDG is first considered to use a single-mode pump. For the spatially degenerate $LP_{11,p}$ and $LP_{21,p}$ modes, equal power is assumed in the even ($LP_{11e,p}$ or $LP_{21e,p}$) and odd modes ($LP_{11o,p}$ or $LP_{21o,p}$) so that the resulting intensity (power) patterns (e.g., $LP_{11,p} = \frac{1}{2}\left(LP_{11e,p} + LP_{11o,p}\right)$) have no azimuthal dependence as shown in Figure 41(a), and hence no MDG between spatially

degenerate signal modes. Figure 42 shows the gain experienced by each signal mode group when pumping in the $LP_{01,p}$, $LP_{11,p}$ and $LP_{21,p}$ modes. It is assumed that the input signal to the EDF has equal power (0.05 mW) in each of its six (two $LP_{01,s}$ and four $LP_{11,s}$) spatial and polarization degenerate modes , or 0.3 mW in total. Since the intensity profile of $LP_{01,p}$ is better matched to $LP_{01,s}$ than $LP_{11,s}$, Figure 42(a) shows higher gain for $LP_{01,s}$. Conversely, pumping in $LP_{21,p}$ results in higher gain for $LP_{11,s}$.

The quality of the match between signal and pump intensity profiles can be evaluated by the overlap integral:

$$\eta_{pj,si} = \int_0^{2\pi}\int_0^{a} r dr d\varphi \, \Gamma_{p,j}(r,\varphi)\Gamma_{s,i}(r,\varphi) \qquad (37)$$

Table 3 shows $\eta_{pj,si}$ for different pump and signal mode pairs.

Table 3：Overlap Integrals of normalized intensity profile

$\eta_{pj,si}$ (m^{-2})	$LP_{01,s}$	$LP_{11,s}$
$LP_{01,p}$	6.2449×10^{9}	3.2848×10^{9}
$LP_{11,p}$	4.4242×10^{9}	3.7472×10^{9}
$LP_{21,p}$	3.2498×10^{9}	3.4857×10^{9}

It is observed that $\eta_{p01,s01}$ and $\eta_{p11,s01}$ are both larger than $\eta_{p01,s11}$ and $\eta_{p11,s11}$. Hence, higher gain is observed for $LP_{01,s}$ when these pump modes are used. Conversely, as $\eta_{p21,s11}$ is larger than $\eta_{p21,s01}$, pumping in $LP_{21,p}$ gives higher gain for $LP_{11,s}$. It is possible to control MDG by varying the relative powers of $LP_{01,p}$ and $LP_{21,p}$. In transmission, the higher-order $LP_{11,s}$ mode is less confined by the core, and will experience higher bending loss than the fundamental $LP_{01,s}$

mode. Furthermore, the $LP_{11,s}$ mode has larger effective area, making the optimum power for this mode higher than the fundamental mode. Consequently, a practical MM-EDFA will pump primarily in the $LP_{21,p}$. The addition of a small amount of $LP_{01,p}$ enables adjustment of MDG. Figure 43(a) shows modal gain versus $LP_{21,p}$ pump power, where the power of $LP_{01,p}$ was continually adjusted to maintain a 1 dB difference between the gains of $LP_{01,s}$ and $LP_{11,s}$, which denotes as $\Delta G_{11s-01s}$. Figure 43(b) shows the same results for $\Delta G_{11s-01s}$ = 2 dB. It is observed that modal gain can be continually adjusted to values greater than 22 dB, which is sufficient to compensate the loss of a single fiber span at typical span distances. Figure 43(c) shows the sensitivity of modal gain to $LP_{01,p}$ power when $LP_{21,p}$ power is fixed at 150 mW. While the modal gain at $LP_{11,s}$ remain nearly constant, $\Delta G_{11s-01s}$ varies by more than 4 dB as $LP_{01,p}$ power is changed from only 0 to 20 mW, demonstrating wide tunability of MDG in dynamic range. Thus, to establish the desired modal gain in an MM-EDFA, the power of the $LP_{21,p}$ pump is first tuned to give the desired power for the $LP_{11,s}$ mode, after which, the power of $LP_{01,p}$ is adjusted to obtain the desired $\Delta G_{11s-01s}$.

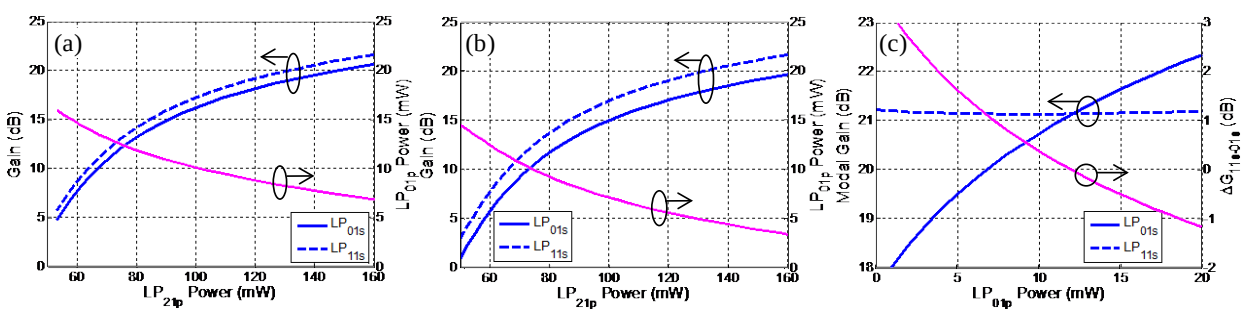

Figure 43: Modal gain and required $LP_{01,p}$ power vs. $LP_{21,p}$ power, to maintain MDG ($\Delta G_{11s-01s}$) at (a) 1 dB and (b) 2 dB; (c) Modal gain and MDG vs. $LP_{01,p}$ power for fixed $LP_{21,p}$ power at 150 mW

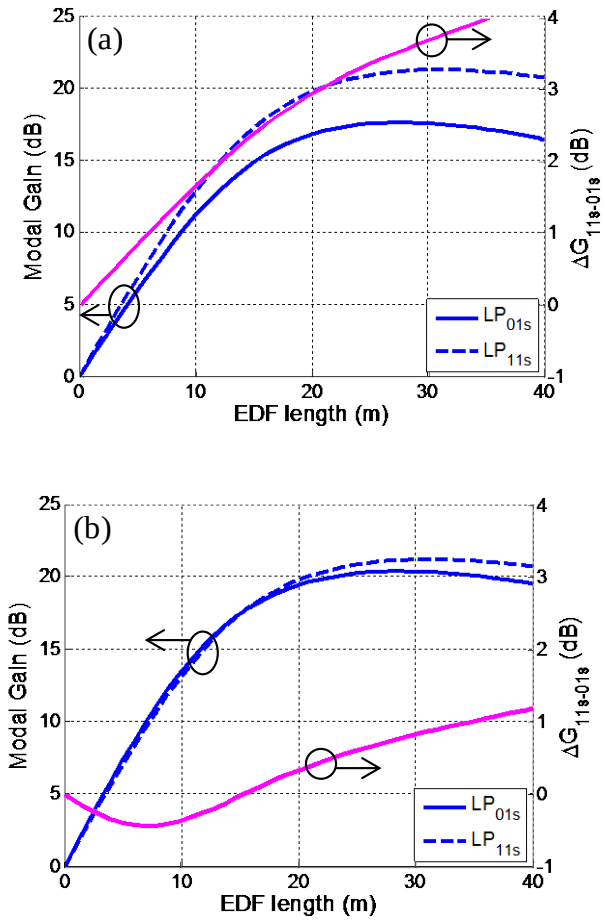

Figure 44: Modal gain and MDG difference vs. EDF length, when $LP_{01,p}$ and $LP_{21,p}$ have powers of: (a) $P_{p,21}$ = 150 mW, $P_{p,01}$ = 0 mW,and (b) $P_{p,21}$ = 150 mW, $P_{p,01}$ = 8 mW

MDG depends not only on pump power, but also the length of the EDF. Figure 44 shows modal gain vs. EDF length for two pump configurations. At short fiber lengths, modal gain increases with increasing EDF length. Eventually, pump depletion and high signal power depletes population inversion, so modal gain decreases for further increases in EDF length. For any given EDF length, $\Delta G_{11s-01s}$ is maximized when only the $LP_{21,p}$ mode is pumped. Figure 44(a) shows that a longer EDF gives larger $\Delta G_{11s-01s}$, and thus larger range of achievable MDG. An EDF length can be selected to approximately maximizes modal gain, while ensuring relatively

large difference between the gains of $LP_{11,s}$ and $LP_{01,s}$. In Figure 44(b), it is observed that adding only 8 mW of pump power in $LP_{01,p}$ enables flattening of the modal gains responses. Even as device length is swept from 20 to 40 meters, less than ±1 dB change in the modal gains of $LP_{11,s}$ and $LP_{01,s}$, and less than ±0.5 dB variation in MDG are observed.

4.4.2 Modal gain control for degenerate mode

In 4.4.1 section, it was assumed that odd and even modes of the spatially degenerate $LP_{11,p}$ and $LP_{21,p}$ modes are pumped with equal power, resulting in no MDG between spatially degenerate signal modes such as $LP_{11,s}$. In practical MDM systems, however, spatially degenerate signal modes may have different losses. One mechanism for MDL is fiber bending, where the loss experienced by each spatially degenerate mode depends on its orientation relative to the plane containing the bend [55]. For the MM-EDFA to overcome MDL, the gains for $LP_{11e,s}$ and $LP_{11o,s}$ need to be adjustable. It was previously observed in Figure 42 that modal gain is related to the intensity overlap between the pump mode and the signal mode. The assumption of equal pump power in even & odd modes for $LP_{11,p}$ or $LP_{21,p}$ caused the overlap integral to be independent of azimuthal angle. A pump with azimuthal intensity dependence is considered. Consider a rotated $LP_{11e,p}$ pump as shown in Figure 45, which was denoted as $LP_{11\theta,p}$.

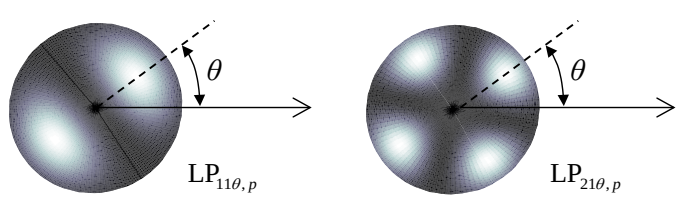

Figure 45: Rotated pump modes

It can be shown that the overlap intensity integral between a rotated pump mode $LP_{mk\theta,p}$ (with m azimuthal nulls in half circle) and an even signal mode $LP_{nje,s}$ with n azimuthal nulls is proportional to:

$$\eta_{p(mk),s(nj)} \propto \int_0^{2\pi} d\varphi \cos^2(m\varphi)\cos^2\left(n(\varphi+\theta)\right) = \frac{\pi}{2} + \cos(2n\theta)\delta(m-n) \qquad (38)$$

where φ is the azimuthal angle, $\delta(\cdot)$ is the Kronecker delta function, and θ is the angular offset. It is observed that if pump and signal has different azimuthal mode number (i.e., $m \neq n$), the overlap integral is independent of θ. Otherwise, the overlap integral – and hence MDG – will have θ dependence.

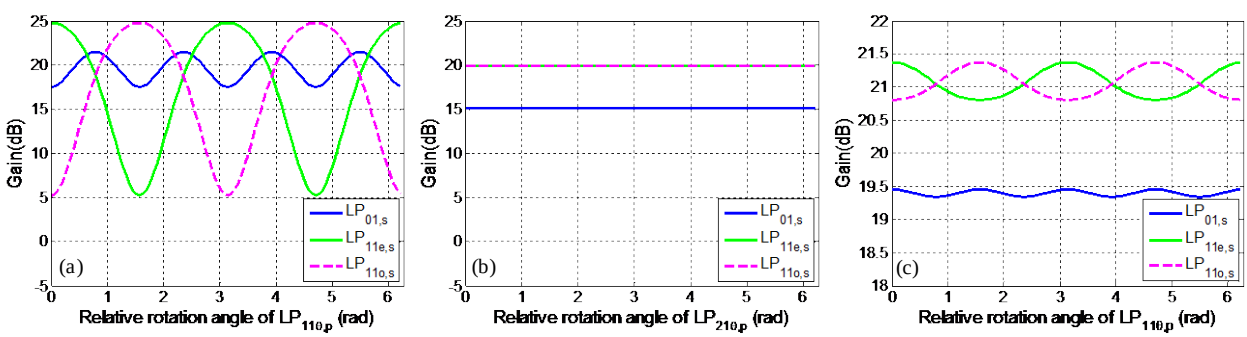

Figure 46: Modal gain vs. relative rotation angle (θ) of the pump mode when pump powers are: (a) $P_{p,11\theta}$ = 150 mW, (b) $P_{p,21\theta}$ = 150 mW, and (c) $P_{p,21}$ = 150 mW, $P_{p,01}$ = 2 mW, $P_{p,11\theta}$ = 15 mW

Figure 46(a) shows the θ dependence of modal gain assuming pump only in the $LP_{11\theta,p}$ mode. As the rotation angle θ is scanned from 0 to 2π, the modal gains for $LP_{11e,s}$ and $LP_{11o,s}$ oscillates with a period of π, reflecting the rotational symmetry of the $LP_{11\theta,p}$ mode. When the intensity peaks of the $LP_{11\theta,p}$ pump align with $LP_{11e,s}$, its gain is maximized while the gain of $LP_{11o,s}$ is minimized, and vice-versa. It is observed that MDG between these modes can be as much as 20 dB. Meanwhile, the fluctuation in gain for the $LP_{01,s}$ mode is a second order effect

caused by gain competition between the signal modes; when the pump is at 45° relative to both the $LP_{11e,s}$ and $LP_{11o,s}$ modes, maximum gain occurs for $LP_{01,s}$. In Figure 46(b), pump is assumed in only $LP_{21\theta,\mathrm{p}}$. In this pumping regime, the rotation angle θ has no impact on MDG, as expected from the overlap integral in (38), which is constant when $m \neq n$. Finally, Figure 46(c) shows MDG for a pump regime similar to one in a real implementation, where the pump is mostly in $LP_{21,p}$ (as defined in Figure 41(a)), with small amounts of $LP_{01,p}$ and $LP_{11e,p}$ added to adjust the MDG between the three modes. The results show that the gain difference between $LP_{11e,s}$ and $LP_{11o,s}$ can be tuned by proper rotation of the $LP_{11\theta,\mathrm{p}}$, while the variation in gain for $LP_{01,s}$ is as small as ±0.05dB.

4.4.3 Impact on performance due to inexact excitation and mode coupling

Previously, it was assumed that (i) the pump can be excited in particular modes of the EDF without leakage into undesired mode, and (ii) no mode-coupling between different pump modes during propagation inside the EDF. In practice, either of these assumptions may be difficult to satisfy. Firstly, to generate the desired pump mode, phase plates are likely to be used as was demonstrated in an MDM transmission experiment in [16]. A phase plate alone (without modulation of transverse amplitude) will result in excitation of other unwanted pump modes. Additionally, spatial misalignment between pump and signal at the beam combiner (shown as the dichroic mirror in Figure 39) will cause further energy leakage into unwanted modes and excess loss, leading to performance degradation.

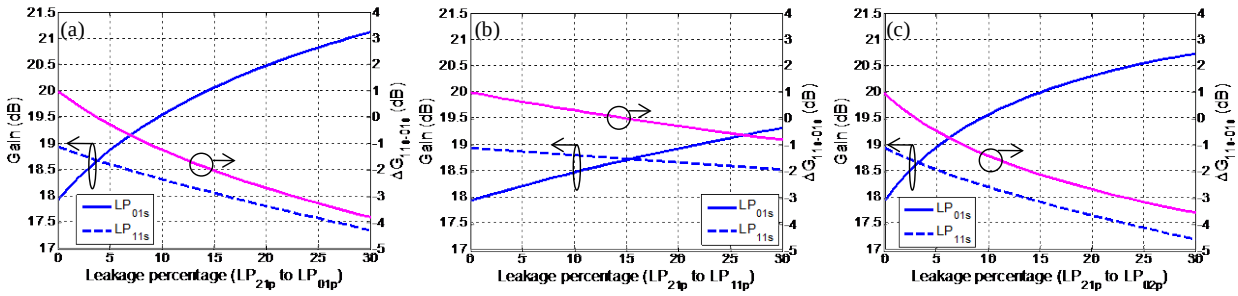

Figure 47: Modal gain vs. power leakage, (a) $LP_{21,p}$ to $LP_{01,p}$, (b) $LP_{21,p}$ to $LP_{11,p}$, (c) $LP_{21,p}$ to $LP_{02,p}$

Only leakage from $LP_{21,p}$ to the other modes is considered, as $LP_{21,p}$ has the most power. Figure 47 shows the modal gains in $LP_{01,s}$ and $LP_{11,s}$ versus the percentage of $LP_{21,p}$ power leaked into the unwanted modes. Note the power in $LP_{01,p}$ is chosen to give an MDG of $\Delta G_{11s-01s}$ = 2dB when 0% of $LP_{21,p}$ is coupled to unwanted modes. As previously shown in Figure 42, pumping in the other modes gives higher gain for $LP_{01,s}$ than $LP_{11,s}$. Hence a reduction in $\Delta G_{11s-01s}$ is observed as leakage increases. At sufficiently high leakage, $\Delta G_{11s-01s}$ becomes negative, indicating higher modal gain for $LP_{01,s}$. It is also observed that $\Delta G_{11s-01s}$ has greater sensitivity to leakage into $LP_{01,p}$ and $LP_{02,p}$, as these modes have larger overlap integrals with $LP_{01,s}$ than $LP_{11,p}$ (Table II). Hence, the pump generation mechanism should minimize leakage into these modes.

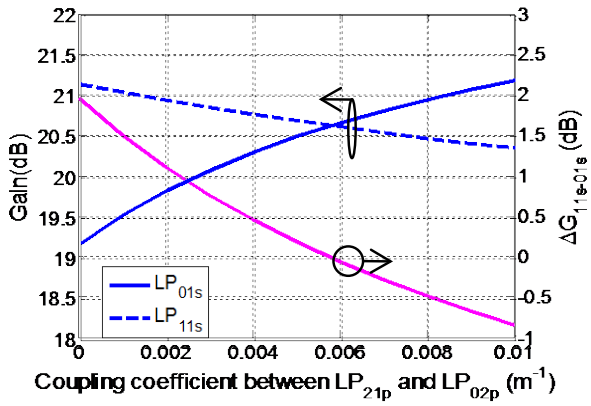

Figure 48 Modal gain vs. mode coupling strength from $LP_{21,p}$ to $LP_{01,p}$ ($d_{p,21\leftrightarrow 02}$)

Mode coupling during propagation inside the EDF will have similar impact as excitation of unwanted modes, since both result in power transferred into undesired modes. The strength of mode coupling is inversely proportional to the difference in effective refractive index between the modes (Δn_{eff}). Hence, the study focus on coupling between $LP_{21,p}$ and $LP_{02,p}$, as the effective refractive index difference $\Delta n_{eff,(21p-02p)}$ between this pair of modes is the smallest among all the mode pairs in the FMF-based EDF. Assuming the power coupling coefficient between $LP_{21,p}$ and $LP_{02,p}$, which was defined as $d_{p,21\leftrightarrow 02}$ in (32), is constant throughout the EDF, Figure 48 shows MDG as a function of $d_{p,21\leftrightarrow 02}$. The value of coupling coefficient refers to [53]. As expected, $\Delta G_{11s-01s}$ decreases with increasing strength of mode coupling. This favors using a shorter length EDF, and a refractive index profile that maximizes effective refractive index difference between the modes to reduce mode coupling。

4.4.4 Impact on performance due to macro-bending loss

In the results thus far, the loss of EDF is assumed to be negligible. In practice, however, the EDF has to be spooled to create a module, which may introduce macro-bending loss. As the

higher order $LP_{11,s}$ and $LP_{21,p}$ modes are less confined, they are more likely to couple into cladding modes when the fiber is bent, resulting in higher macro-bending loss than the fundamental modes $LP_{01,s}$ and $LP_{01,p}$. This must either be taken into account by increasing the power of the higher order pump, or the bending radius has to be large enough to render bending loss negligible. The theoretical macro-bending loss can be calculated using Marcuse's curvature loss formula [56]. Figure 49 shows the macro-bending losses for the various signal and pump modes as functions of bend radius.

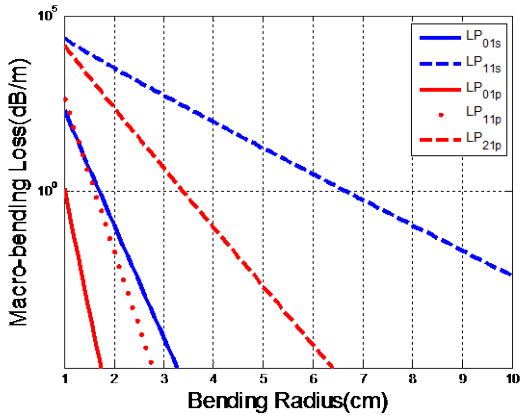

Figure 49: Macro-bending loss vs. bending radius

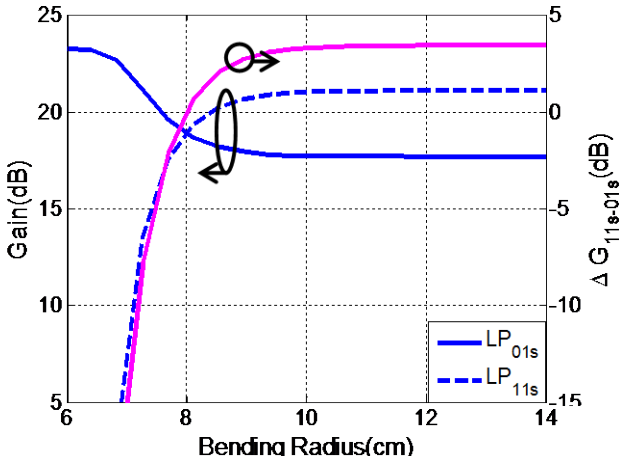

Figure 50: Modal gain vs. mode dependent loss of LP_{11s}

It is observed that macro-bending loss of all modes grows exponentially as bending radius decreases. In particular, the $LP_{11,s}$ mode is the least spatially confined. To reduce its macro-bending loss to less than 0.01 dB/m, the bending radius must be at least 9.46 cm. Figure 50 shows modal gain as a function of bend radius assuming only LP_{21p} is pumped at a power of 150 mW. It is observed that the gain of $LP_{11,s}$ is reduced significantly as bend radius falls below 9 cm. In particular, MDG between the modes is reduced to zero at a bend radius of 8 cm, making it impossible to equalize MDL in the transmission by pumping in LP_{01p} as outlined in Section 3.1. It is observed that at low bend radius, the gain of $LP_{01,s}$ is increased due to reduced mode competition. However, the increase in gain saturates when $LP_{11,s}$ is completely stripped out. At very small bend radius, macro-bending loss will again reduce the gain of $LP_{01,s}$. The results indicate that a practical EDF should be spooled with a bend radius greater than 9 cm for a step-index fiber design. If device size is an issue, it is also possible to create fibers more complex refractive index profiles, such as using refractive index trenches, to better confine all signal and pump modes.

4.5 Conclusion

A multimode EDFA with modal gain control is proposed. By adjusting relative amount of $LP_{01,p}$ and $LP_{21,p}$, the gains of the $LP_{01,s}$ and $LP_{11,s}$ signal modes can be tuned over a wide dynamic range. The relative gain between the two spatially degenerate $LP_{11,s}$ signal modes can also be adjusted by adding a small amount of $LP_{11\theta,p}$ which is the even $LP_{11e,p}$ mode rotated by angle θ. Performance impact due to excitation of unwanted pump modes at the input of the EDF, mode coupling and macro-bending loss in the fiber was also investigated. The proposed modal

gain control scheme can be generalized for an *N*-mode MM-EDFA by varying the powers of *N* well-chosen pump modes.

CHAPTER 5 WAVELENGTH-DIVISION MULTIPLEXED – MODE-DIVISION MULTIPLEXED TRANSMISSION USING ONLINE FEW-MODE EDFA

5.1 Introduction

By implementing digital signal processing and few-mode EDFA discussed in previous chapters, a WDM-MDM transmission experiment was demonstrated via 50km FMF. In this chapter, the characterization of two key components, namely FM-EDFA and phase plate will be shown, following by transmission experiment setup and results. At the end, with the aid of transmission data, the FMF is further characterized.

5.2 Few-mode EDFA

A few-mode erbium-doped fiber amplifier (FM-EDFA) was constructed out of 15 meters of few-mode erbium-doped fiber. Originally intended as a step-index profile fiber with a uniformly doped core, the actual refractive index profile measured in the radial direction is shown in Figure 51(a).

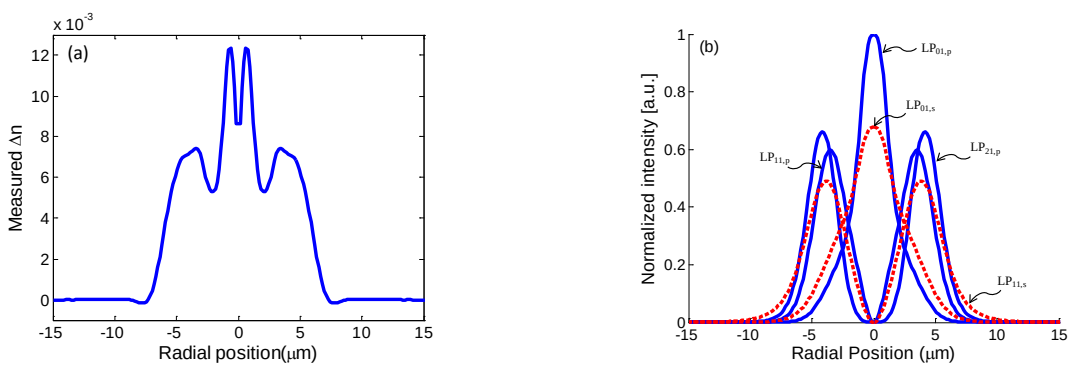

Figure 51 (a) Refractive index of MM-EDF, (b) Normalized radial intensity profiles of signal and pump modes

The FM-EDF supports two mode groups at the signal wavelength (around 1550 nm): $LP_{01,s}$ and $LP_{11,s}$, and four mode groups at the pump wavelength (around 980 nm): $LP_{01,p}$, $LP_{11,p}$, $LP_{21,p}$ and $LP_{02,p}$. Normalized intensity distributions for the signal and pump modes of interest are shown in Figure 51(b)[57].

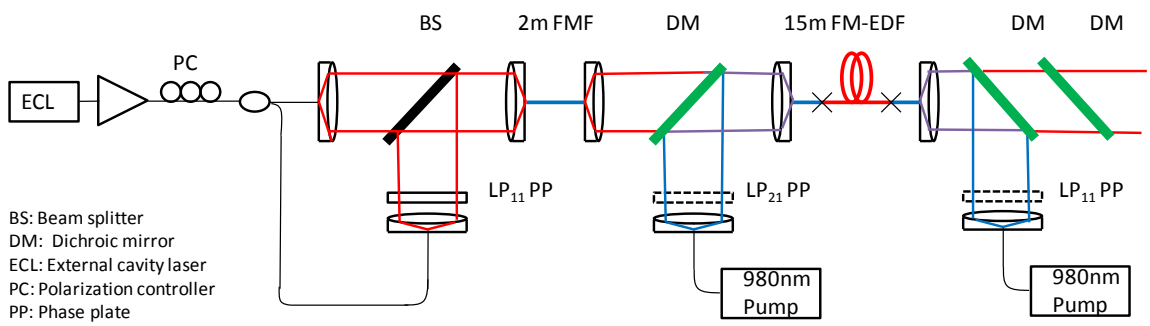

Figure 52 Experiment setup

To characterize the FM-EDFA, the experiment setup is used as shown in Figure 52. A tunable C-band external cavity laser (ECL) is amplified and passed through a polarization controller (PC), and is then spatially transformed by a mode multiplexer. The mode multiplexer splits the input signal into two paths. The single-mode fiber in each path is terminated by a beam collimator (BC) with focal length of 11 mm. At one of the paths, a phase plate (PP) converts the LP_{01} Gaussian beam into an LP_{11} mode. The two beams are passively combined by a passive beam splitter (BS) and launched into two meters of un-doped FMF of the same type as the 50-km FMF used in the transmission experiment which supports the propagation of LP_{01} and LP_{11} modes at the signal wavelength. At the FM-EDFA, the FMF is terminated at another 11-mm BC. A dichoric mirror (DM) spatially combines the signal beam with a 980 nm forward pump beam, which is collimated by an 8-mm BC followed by an optional PP. The spatially overlapping signal

and pump are launched into the FM-EDF whose ends were spliced with short sections of un-doped FMF. At the output of the FM-EDFA, another 980nm pump beam is collimated by an 8-mm BC and spatially transformed by an optional PP. After reflection by a DM, the beam is launched into the output of FM-EDF as a counter propagating pump. The output facet of the FM-EDF is angle-cleaved to minimize reflections back into the amplifying medium, and terminated the fiber at an 11-mm BC. Two DMs are used to filter the unused pump, allowing the signal power and beam profile to be measured.

Coupling losses of the setup are measured to be: 1.8 dB and 3.9 dB for coupling between single-mode fiber and the LP_{01} and LP_{11} modes at the signal wavelength; and 5dB, 7.2 dB and 9.6 dB for coupling between single-mode fiber and the LP_{01}, LP_{11} and LP_{21} modes at the pump wavelength. The higher losses for the pump are due to chromatic dispersion of the lens, which causes the BC to have different focal lengths at the signal and pump wavelengths. Since the position of the terminated fiber is optimized for the signal wavelength in the BC, the pump beam is not well focused.

Figure 53(a) and (b) show the modal gain measured for $LP_{01,s}$ and $LP_{11,s}$ when forward pumping in $LP_{01,p}^{(f)}$ and $LP_{21,p}^{(f)}$, after account for all coupling losses. As Figure 53(c-d) show, the modal gain were also measured when backward pumping in $LP_{01,p}^{(b)}$ and $LP_{11,p}^{(b)}$. The wavelength of the input signal was set to the peak gain wavelength of 1537 nm, while the signal power was −10 dBm per mode. Since the pump laser produces a maximum output power of 26.5 dBm, the highest powers displayed in the horizontal axes of Figure 53 for $LP_{21,p}^{(f)}$ and $LP_{11,p}^{(b)}$ pumping are 16.9 dBm and 19.3 dBm, respectively. The measured gains are shown as triangles for $LP_{01,s}$, and

crosses for $LP_{11,s}$. The gain characteristic shown in Figure 53 matches the expectation that pumping in $LP_{01,p}$, in either forward or backward direction, leads to higher gain for $LP_{01,s}$, while pumping in higher order modes, significantly reduces this mode-dependent gain (MDG). In the case of forward $LP_{21,p}^{(f)}$ pumping scheme, modal gain for $LP_{01,s}$ and $LP_{11,s}$ are approximately equalized.

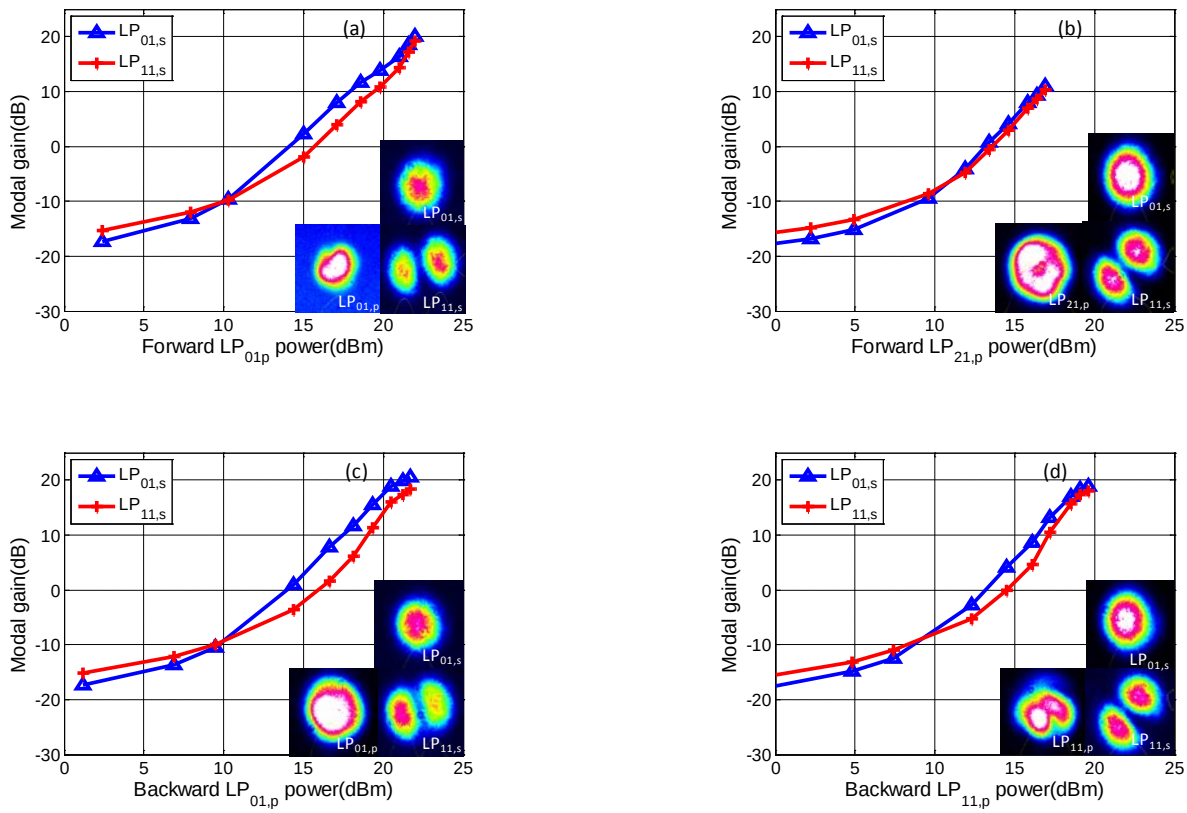

Figure 53 Modal gain vs. Pump power when pumping forward in: (a) $LP_{01,p}$, (b) $LP_{21,p}$, and backward in(c) $LP_{01,p}$ (d) $LP_{11,p}$

Figure 54 (a) shows signal gain for $LP_{01,s}$ and $LP_{11,s}$ as a function of wavelength when pumped with 16.9 dBm of $LP_{21,p}^{(f)}$ or $LP_{11,p}^{(b)}$, at an input signal power of −10dBm. The shapes of the

gain spectra match the typical emission spectrum of EDF. Figure 54(b) shows MDG vs. wavelength. As a reference, MDGs for pumping in $LP_{01,p}$ for both forward and backward direction are also shown as blue lines. Although the $LP_{11,s}$ mode has less gain than $LP_{01,s}$ for both pumping method, pumping in $LP_{11,p}^{(b)}$ reduces MDG by ~ 1.3 dB at the peak gain wavelength of 1537 nm compared with pumping in $LP_{01,p}^{(b)}$. Moreover, pumping in $LP_{21,p}^{(f)}$ introduces even more MDG reduction which is 3.5dB. The total excursion of MDG across the C-band is also reduced from more than 3.5 dB to 2.5dB and 1 dB for $LP_{11,p}^{(b)}$ and $LP_{21,p}^{(f)}$ respectively.

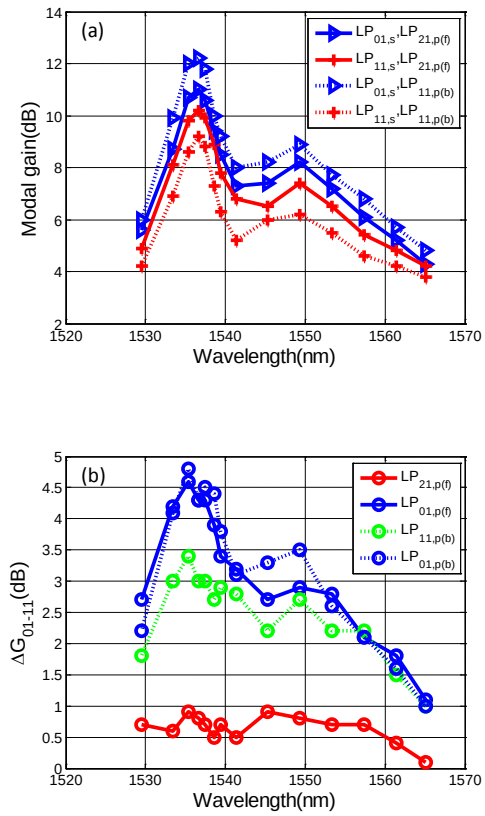

Figure 54 (a) Modal gain vs. signal wavelength, using $LP_{21,p}$ (forward) and $LP_{11,p}$ (backward) and (b) MDG vs. signal wavelength using forward pumps in $LP_{01,p}$, $LP_{21,p}$ and backward pumps in $LP_{01,p}$, $LP_{11,p}$

5.3 Phase Plate

In order to achieve high-efficiency crosstalk-free modal transformation, high optical quality phase plates with accurate optical transfer function are required. The fabrication process needs to provide an accurate, stable and steep phase transition between regions. For this purpose, fabricated and characterized monolithic binary phase plates using a highly uniform Ag+/Na+ ion-exchange (IE) in glass, which provides important advantages compared to methods based on changing the thickness of the material. IE in glass is a well-established technique for material processing, integrated optics and other applications [58]. High precision and versatility are achieved through control of fabrication parameters such as diffusion time, temperature, diffusion coefficient, and the salt melt concentration. By using a Gaussian model together with the Inverse Wentzel-Kramer-Brillouin Method (IWKB) method, the desired phase-shift can be predicted by optimizing the refractive index variation of the Ion exchanged region. Phase plates designed for 1550 nm and 980 nm operation were fabricated with 5% $AgNO_3/NaNO_3$ salt melt at 340 °C. Multi-region binary plates were fabricated by using multi-region masks made by high-precision photolithographic techniques [59].

Phase plates were characterized by interferometry together with a modified Carré algorithm for the phase recovery. After phase is determined, an approximation technique for the diffusion time is used to improve the value of the required phase if necessary. The final phase value was set at 98% of the desired value (π radians) so tilting the phase plate by a small angle enables modal conversion be optimized.

5.4 WDM-MDM Transmission Experiment

5.4.1 Experiment Setup

The experimental setup is shown in Figure 55. At the transmitter, 88 lasers (87 distributed-feedback (DFB) laser and one external cavity laser (ECL) for the channel measured) are divided into odd and even groups. Each group is separately modulated with 28 Gbaud QPSK, where the in-phase (I) and quadrature (Q) drive voltages are generated from pseudorandom binary sequence (PRBS) of length 2^{31}–1. Polarization-multiplexed signals are generated by splitting the modulator outputs, delaying one path by 405 symbols (14.46 ns), rotating it to the orthogonal polarization before polarization recombining. Odd and even channels are combined using an optical interleaver. The signal spectrum at the output of the single-mode transmitter is shown as an inset of Figure 55.

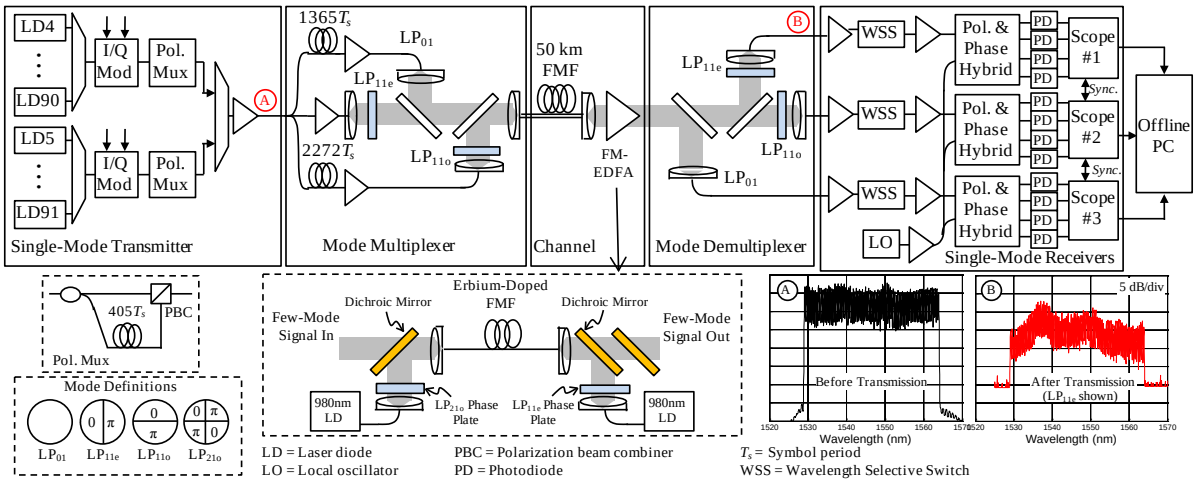

Figure 55 Experimental Setup

In the mode multiplexing circuit, the signal is split into three tributaries. Following de-correlation delays and amplification, the single-mode fibers are terminated at beam collimators

(BC) with focal lengths of 11 mm. The beams propagating in free-space have 1/*e* radii of ~2 mm. For the LP_{11o} and LP_{11e} tributaries, phase plates with dual partitions having relative path delays of 0 and π radians at 1550 nm are used to spatially modulate the signal beam. Figure 56(a) shows the intensity patterns measured by a beam profiler placed in the far field. The three spatially orthogonal beams are combined using passive beam splitters (BS), and the mode-division multiplexed (MDM) signal is launched into 50 km of FMF via an 11-mm BC. In this experiment, the relative difference in path lengths seen by the LP_{11o}, LP_{01}, and LP_{11e} tributaries (from the 1-by-3 splitter to the FMF input) are 0, 48.75 ns and 81.14 ns, respectively (corresponding to 0, 1365 and 2272 symbols). Thus, the minimum de-correlation delay between the six spatial-polarization modes is 405 symbols arising from the polarization multiplexer. This value is much greater than the modal group delay (MGD) of the FMF or the length of the time-domain equalizer used for MIMO de-multiplexing, thus ensuring no spurious convergence where an equalizer output tributary obtains degenerate information from two different launched modes.

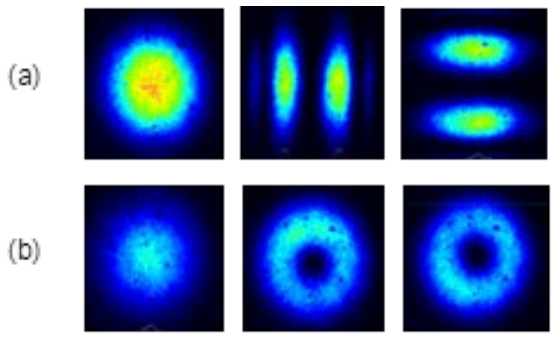

Figure 56 (a) Intensity patterns at transmitter, (b) intensity patterns after 50-km FMF

The intensity patterns measured for the three spatial modes after 50-km transmission are shown in Figure 56(b). Note that the LP_{11} patterns depend on the instantaneous coupling condition between odd and even modes, and is time-varying. The MDM signal is amplified using

the FM-EDF considered in Section 5.2, with two 980 nm lasers pumps in forward and reverse directions. Pump and signal wavelengths are combined using free-space dichroic mirrors with insertion loss ~0.5 dB. Phase plates (designed for 980 nm) are used to spatially modulate the pumps. The forward-propagating pump is in the LP_{21} mode, while the backward-propagating pump is in the LP_{11} mode [60]

At the receiver, the mode de-multiplexer is a mirror image of the transmitter's mode multiplexer: the FMF is terminated at an 11-mm BC and use BSs to split the signal into three tributaries. In the LP_{11o} and LP_{11e} tributaries, the signal is spatially demodulated using phase plates. All three tributaries are then coupled back into single-mode fibers using 11-mm BC. These signals are amplified and then filtered by wavelength selective switches (WSS). The channel of interest is down-converted to electrical baseband by mixing the signals with a common local oscillator (LO) laser using three polarization-and-phase diversity hybrids and twelve photo-detectors, recovering the in-phase (I) and quadrature (Q) components of the six spatial-polarization modes. The electrical signals are sampled using three quad-channel sampling oscilloscopes with sampling rates and electrical bandwidths of 40 GSa/s and 16 GHz.

For data recovery, the digital signal processing algorithm described in chapter 2 is used. In the experimental results presented in sections 5.4.2 and 5.4.3, twenty data sets of 32,768 symbols were captured. For each data set, bit-error rate (BER) and Q-factor were computed from the second-half of the data after convergence of the TDE, (i.e., 655,360 bits per spatial-polarization modes were evaluated).

In this experiment, the coupling loss between single-mode fiber and the LP_{01} mode of the FMF is 1.8 dB, while the coupling loss between single-mode fiber and the LP_{11} of the FMF (the

loss due to the phase plate is negligible) is 3.5 dB. The losses of the beam splitter are 2.8 dB (through) and 4.0 dB (reflected). The attenuation of the FMF are ~0.22 dB/km for the LP_{01} mode and ~0.25 dB/km for the LP_{11} mode. Summing these losses, the LP_{11o} and LP_{11e} modes have the highest total end-to-end loss of ~29.1 dB. The gains of the transmitter's single-mode fiber amplifiers were set so that all three spatial modes have the same power at the output of the FMF (i.e., before the FM-EDFA).

5.4.2 Results

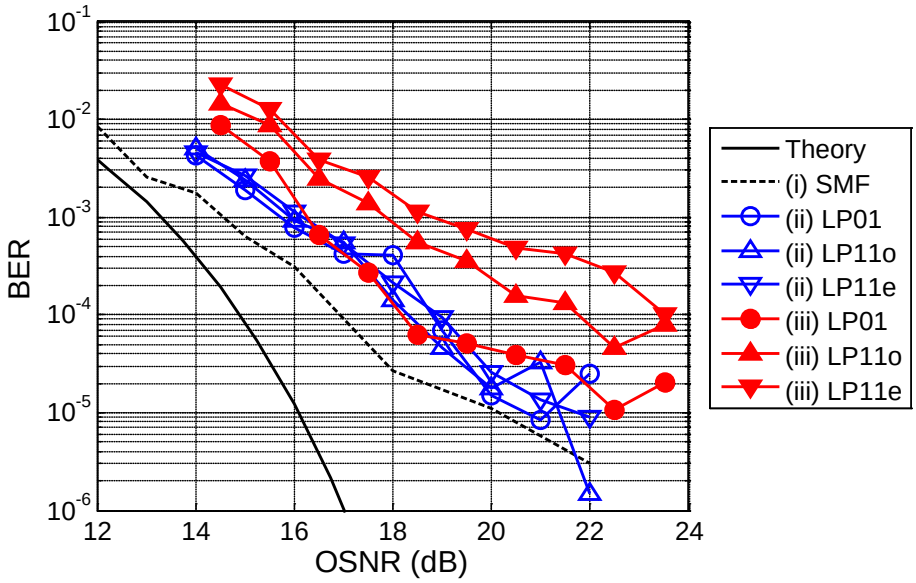

Figure 57 BER vs. OSNR

Figure 57 shows BER vs. OSNR curves for: (i) single-mode fiber back-to-back (BTB), (ii) MDM transmission BTB (via 1 meter of FMF), and (iii) after transmission for channel 38 at 1550.12 nm. It is observed that at a target BER of 10^{-3}, the OSNR penalty for cases (i) and (ii) with respect to the theoretical additive white Gaussian noise-limited BER vs. OSNR curve for QPSK are 1.2 dB and 2.8 dB, respectively. The similar penalties experienced by all three spatial

modes in case (ii) indicate the channel matrix is approximately unitary. For case (iii), an equalizer of 301 taps per tributary was used to compensate MGD and CD. The length of the equalizer was sufficient to overcome the MGD of the channel. The larger OSNR penalties for the higher-order LP_{11o} and LP_{11e} modes are caused by a combination of mode coupling at the MM-EDFA and mode-dependent gain in the amplifying medium causing the channel matrix to be non-unitary.

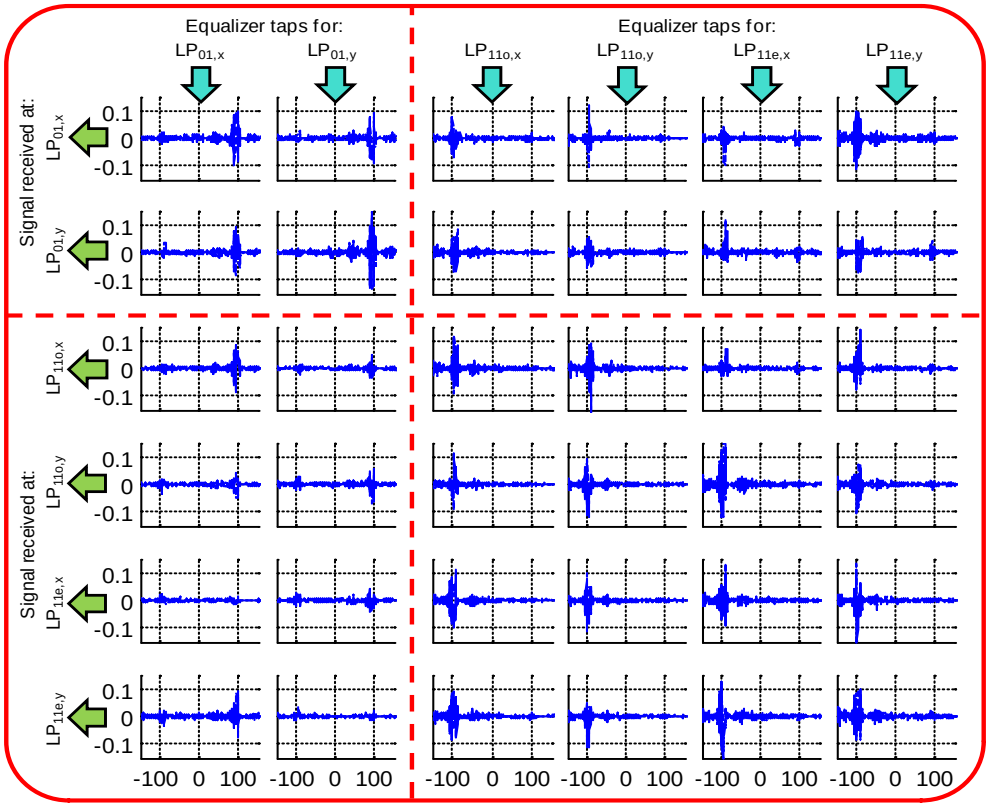

Figure 58 Time-domain equalizer taps after convergence

Figure 58 shows an example of the TDE obtained after convergence. The subplot at the intersection of the ith row and j^{th} column is the element filter W_{ij}. In this experiment, $M = 2$ times oversampling and $N = 301$ taps for the TDE are used. The tap length corresponds to a

time span of 151 symbols sufficient to overcome the channel's MGD. The vertical axis in each subplot is the value (real and imaginary components shown) of the filter coefficient, and the horizontal axis is the time index $-L \le l \le L$. The training symbols are aligned with the received signal in such manner that the coefficient at $l = 0$ is about halfway between the arrival times of the LP_{01} and LP_{11} modes. The coefficients $l > 0$ are the causal coefficients, and the coefficients $l < 0$ are anti-causal coefficients.

The columns of Figure 58 (left to right) are the TDE coefficients used to recover the symbols transmitted in the $LP_{01,x}$, $LP_{01,y}$, $LP_{11o,x}$, $LP_{11o,y}$, $LP_{11e,x}$ and $LP_{11e,y}$ modes; while the rows denote the TDE coefficients operating on the outputs recovered at the $LP_{01,x}$, $LP_{01,y}$, $LP_{11o,x}$, $LP_{11o,y}$, $LP_{11e,x}$ and $LP_{11e,y}$ ports of the coherent receiver. The principle sub-matrices of the TDE are the 2×2 sub-matrix at the top-left quadrant and the 4×4 sub-matrix at the bottom-right quadrant, which denote energy transmitted in one mode group being received at the ports of that mode group. Most of the energy in these sub-matrice is concentrated around a single peak corresponding to the expected arrival time for a signal propagating in that mode group in the FMF. The lack of spurious peaks indicates negligible multipath interference (MPI), where energy launched into one mode group is coupled to another mode group and then back again. By contrast, the off-diagonal sub-matrices denote energy transmitted in one mode group being received at the ports of the other mode group. This arises from mode mixing either at the transmitter, the FM-EDFA or the receiver. Considering the 4×2 sub-matrix in the bottom-left quadrant, the right-most peak denotes the signal propagating in the LP_{01} mode in the FMF, but is received at an LP_{11} port, while the left-most peak denotes the LP_{01} signal is coupled to LP_{11} at

the transmitter, which propagates in the LP_{11} mode in the FMF and is received at an LP_{11} port. The temporal separation between the two peaks is the modal group delay in the 50-km FMF, which in this instance is around 91 symbols (3.25 ns), corresponding to a MGD of 65 ps/km. The dispersed peaks of the LP_{01} and LP_{11} modes arise from CD. Figure 59 shows a typical training characteristic, where it is observed the TDE taps converged after ~10,000 symbols.

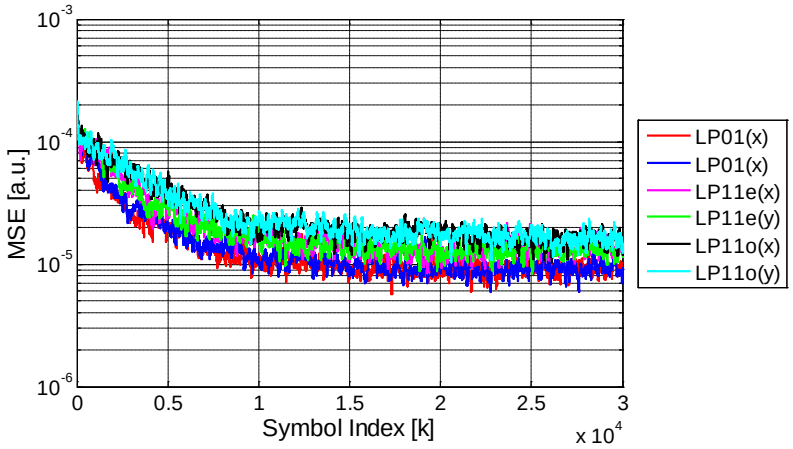

Figure 59 Training characteristic: Mean square error vs. adaptation period

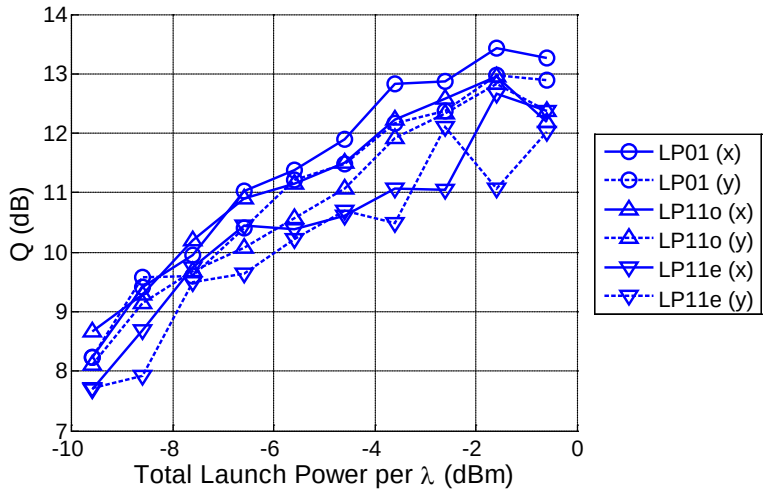

Figure 60 Q vs. Launch Power after transmission

Figure 60 shows Q vs. launch power after transmission. It is observed that the Q-factor is still increasing at the highest power, indicating that the system remains in the linear regime even when the transmitter's EDFAs are set to their maximum output powers. System performance is therefore limited by the combined amplified spontaneous emission (ASE) of the FM-EDFA and single-mode EDFAs. In Figure 61, the BERs after transmission is shown for all the channels at the optimal launch power of −0.5 dBm/λ. It is observed that the BER of all modes of all the WDM channels are below the threshold of 3.8×10^{-3} for 7% hard-decision forward-error correction (HD-FEC) code. The BERs at the short wavelengths (right-hand side) are slightly higher due to the gain vs. wavelength characteristic of the MM-EDFA. The constellations of the best (Ch. 48) and worst (Ch. 88) channels are shown in the insets.

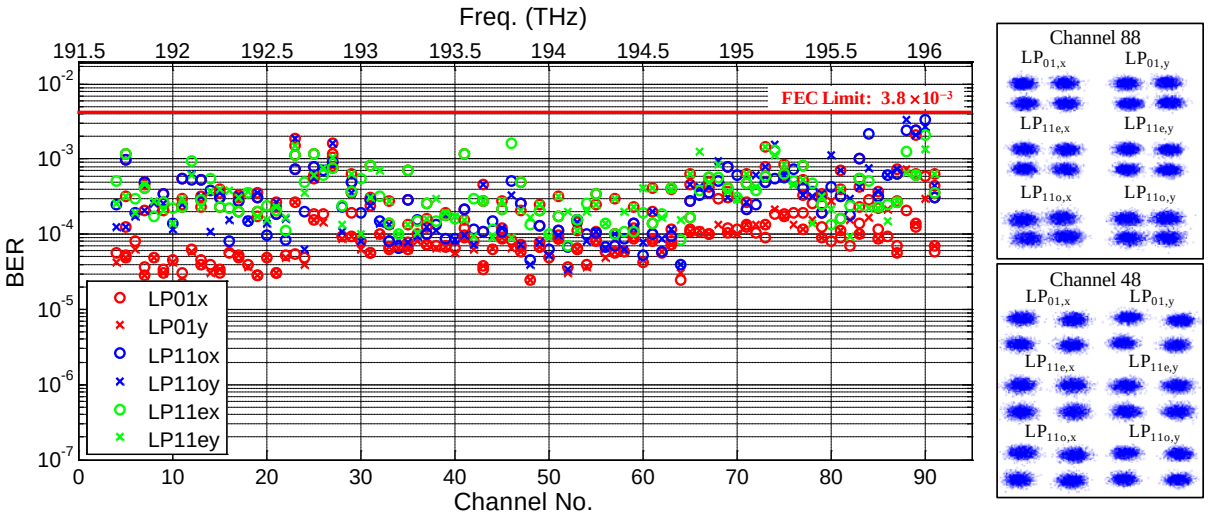

Figure 61 Measured BER for all WDM channels after transmission. Insets: Constellation diagrams of best and worst modes

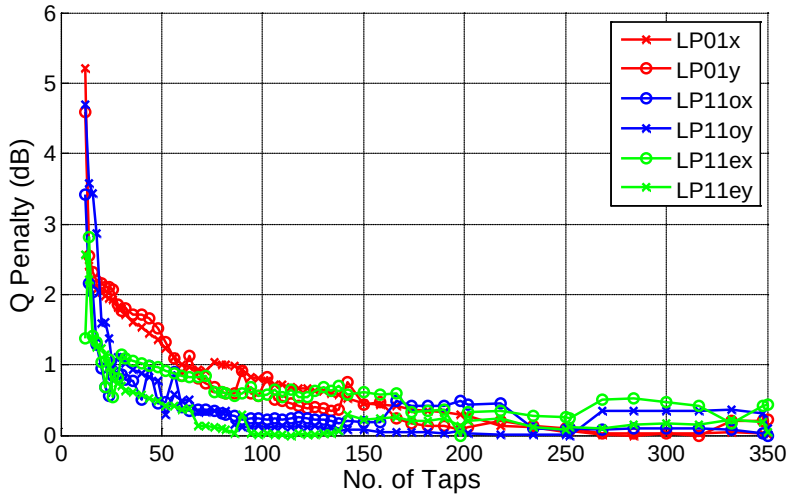

Figure 62 Q penalty vs. No. of taps per tributary of 6×6 equalizer

From the TDE taps observed in Figure 58, it is possible to achieve significant reduction in algorithmic complexity by keeping only those equalizer taps with significant energy around each peak. Additionally, the number of significant taps at each peak can be reduced by compensating known CD using the FDE. Figure 62 shows Q penalty vs. number of taps (N_{taps}) per TDE tributary, where half of the taps are allocated around each peak centered at the LP_{01} and LP_{11} arrival times. It is observed that to achieve Q penalty less than 1 dB, around 80 taps per tributary are required.

5.4.3 Fiber Characterization

The FMF has a graded index core that was optimized to simultaneously achieve large effective area, low MGD and low coupling between the LP_{01} and LP_{11} modes. The calculated effective areas of the LP_{01} and LP_{11} modes are 137 and 183 μm^2, respectively, and the calculated MGD and chromatic dispersion are plotted in Figure 63.

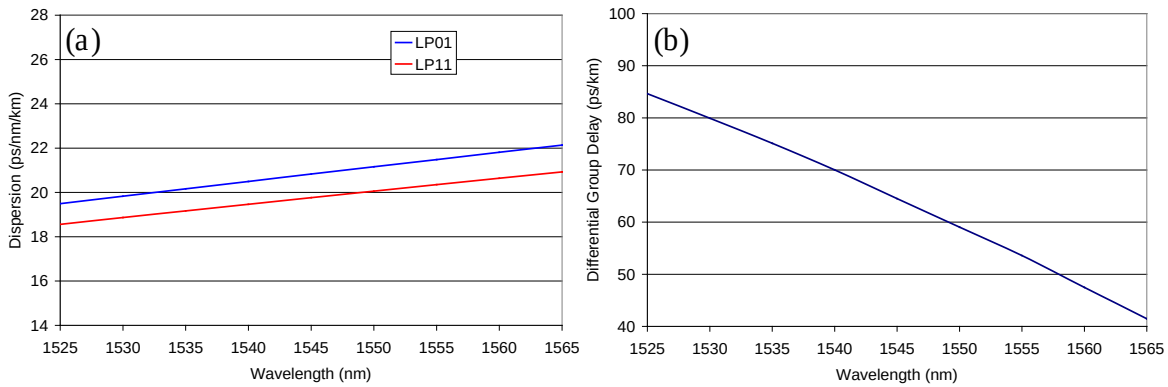

Figure 63 Predicted (a) differential mode group delay and (b) chromatic dispersion

The MGD of all the channels can be estimated experimentally from the equalizer coefficients after convergence. Figure 64(a) shows the results, where it is observed that MGD varies from 50 to 80 ps/km across the C-band. In addition, the use of training symbols enables measurement of the change in group delay with channel wavelength, and hence the CD of each mode of the FMF. The results are shown in Figure 64(b). It is observed that the CD of the LP_{01} and LP_{11} modes at 1550 nm are around 20.5 and 19.8 ps/nm/km, respectively. The fluctuations of the data points from the regressive lines are due to measurement "noise" which arises from temperature drift as the channels are swept – i.e., small changes in either refractive index and fiber length will cause a change in the arrival time of the signal (group delay) independent of chromatic dispersion. To reduce measurement noise, the channel is swept in ascending order of channel number as rapidly as possible to reduce thermal fluctuations. The measured differential MGD and chromatic dispersion agree well with the calculated values.

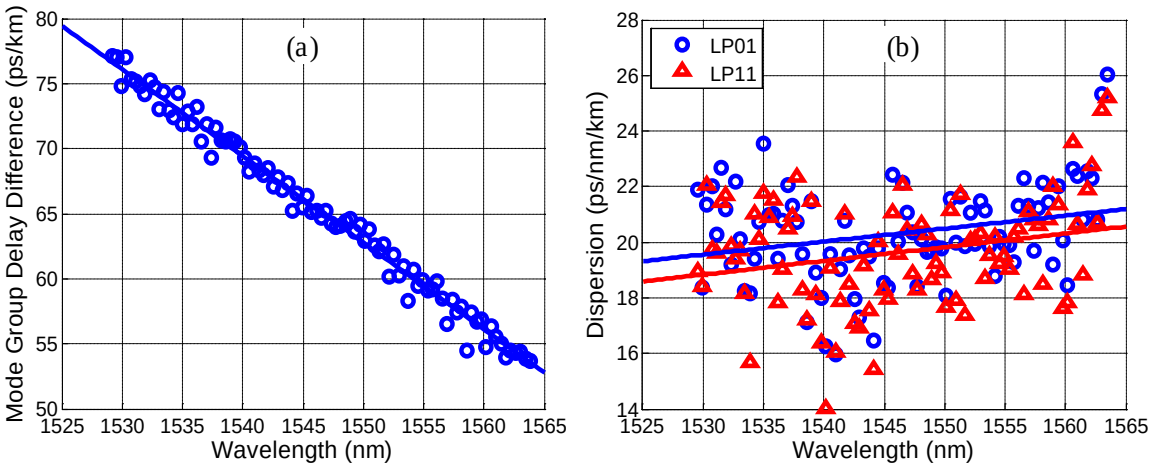

Figure 64 Measured (a) differential MGD and (b) dispersion characteristic for experimental FMF

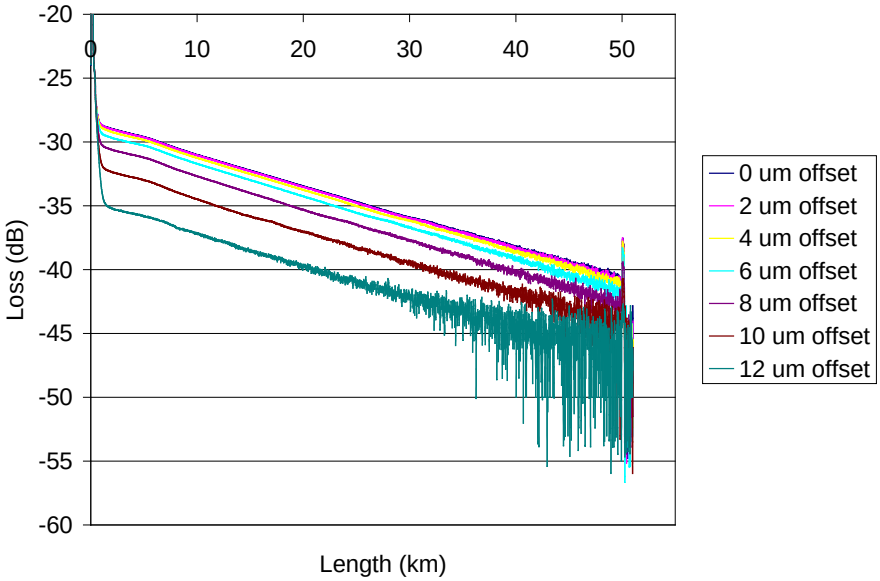

Figure 65 Measured OTDR traces at different offset launch positions

To characterize the fiber attenuation, OTDR traces are measured with different offset launch positions with a standard single-mode fiber. When there is no offset, it is expected that most light is launched into the LP_{01} mode. When the offset increases, more and more light will be launched into the LP_{11} mode. Figure 65 shows OTDR traces for seven different launch

positions. The attenuation increases slightly from 0.243 dB/km to 0.252 dB/km from center to 12 μm offset, indicating a very small attenuation difference between the LP_{01} and LP_{11} mode

5.5 Conclusion

A 26.4 Tb/s mode-division multiplexed DWDM signal was successfully transmitted over 50-km of few-mode fiber with an inline few-mode EDFA before the receiver. Phase plates and free-space optics were used for spatial mode multiplexing and de-multiplexing. The received signal was detected using three synchronized coherent receivers. Mode coupling, modal group delay and chromatic dispersion were compensated using a digital 6×6×301 MIMO equalizer. The mode-dependent gain of the few-mode EDFA, as well as the differential modal group delay and dispersion characteristics of the transmission few-mode fiber was also characterized.

The experiment was ultimately limited by ASE noise of the receiver's single-mode EDFAs. We attribute this to the high loss of the receiver's spatial de-multiplexer. To enable longer transmission distance, it is possible to (i) use a multi-spot coupler [20] to de-multiplex the MDM signal without the high losses incurred by the current spatial de-multiplexer, and (ii) use a higher-gain FM-EDFA to boost the MDM signal power above sensitivity. In particular, it is necessary for the gain of the FM-EDFA to be at least equal to the span loss in both mode groups of the FMF in order to enable multi-span transmission using a recirculating loop.

CHAPTER 6 SUMMARY AND FUTURE RESEARCH DIRECTION

The dissertation focused on overcoming two fundamental challenges of mode-division multiplexed transmission in few-mode fibers, namely, multimode interference and modal loss. Theoretical, numerical and experimental results were obtained and discussed to verify the effectiveness of the approaches.

As a first effort in mode-division multiplexing, adaptive frequency-domain equalization for MIMO processing was presented. Traditional time-domain equalization algorithm is directly generalized from polarization-division multiplexing system whose channel impulse response spread is much shorter that in FMF. In MDM systems, the algorithmic complexity of FDE scales logarithmically with CIRS instead of linearly as for TDE. For long-haul MDM transmission systems, FDE can potentially reduce the algorithmic complexity by 2 orders of magnitude. The algorithm was first simulated and then demonstrated in a 50km single-span as well as a 1000km loop MDM transmission experiment. FDE shows similar performance as traditional TDE.

To further improve the performance and efficiency of the algorithm, two improvements were made. First, normalized adaptive FDE was introduced to increase the convergence speed of the equalizer thus reducing the training symbol length and achieving fast adaptation. Experiment results for a 600km MDM transmission showed that NA-FDE can converge 6 times faster than conventional FDE. Second, master-slave carrier recovery was proposed to simplify the computational load for frequency offset and phase estimation. Less than 1dB Q penalty using MS-CR scheme was observed in 1000km MDM transmission experiment while the algorithmic complexity of phase estimation was reduced to 1/6 of conventional scheme.

Although FDE significantly reduces computational complexity of MIMO processing, the required memory length is still relatively large due to large CIRS in FMF. Consequently, the required circuit size of DSP chip is large. To reduce the hardware complexity, DMGD compensated fiber has been introduced and demonstrated. It was well known that DMGDC link can effectively simplify the MIMO processing given that distributed mode coupling is negligible. However, as far as the author knows, no investigation has been conducted for DMGDC link with weakly mode coupling which is the practical case. In chapter 3, theoretical as well as numerical analysis about equalizer tap length requirement were presented for the system. Under the weak random mode coupling assumption, the CIRS of DMGDC link linearly depends on the MGD of a single DMGDC fiber section instead of overall MGD in DMGD uncompensated link. Consequently, by using small compensation step-size, the required tap length can be compressed by 2 orders of magnitude compared to DMGDUC link.

Apart from multimode interference, differential loss for different mode channels is the other fundamental challenge for long-haul MDM transmission. Few-mode EDFA using multimode reconfigurable pump was proposed and designed to compensate modal losses. By adjusting mode contents of the pump, modal gain can be tuned in a large dynamic range. The modal gain control properties of the proposed FM-EDFA were first investigated using numerical analysis for both non-degenerate as well as degenerate modes. A proto-type FM-EDFA was also constructed. The experimental results show that by using high-order pump mode, the modal gain difference can be reduced.

With the help of FM-EDFA and efficient FDE MIMO processing, a WDM-MDM transmission experiment was demonstrated. Eighty eight wavelength channels in 6

spatial/polarization modes were successfully transmitted through 50km FMF with inline FM-EDFA. The aggregate capacity was 26.4 Tb/s.

The aforementioned techniques are important steps towards practical implementation of MDM transmission. However, many new challenges and research directions emerge to be explored in the future. Some of the challenges facing academia and industry in this context are discussed henceforth.

For real-time implementation of MIMO DSP, application-specific integrated circuits (ASIC) are expected to be used. Therefore, a theoretical estimation of hardware complexity in terms of circuit size or gate numbers is important to be investigated to provide guidelines for system design. The circuit size is related to memory length of the block as well as the number of used mode. Although adaptive FDE is much more efficient compared to time-domain approach in terms of algorithmic complexity, it requires block processing and FFT operation. For long-haul transmission, the CIRS can be thousands of symbol periods leading to large memory length. On the other hand, MIMO equalizer is more complicated for more mode channels. The number of elements of filter matrix in MIMO equalizer equals to square of number of used mode channels. As a result, it is critical to design an energy efficient ASIC in the future for MDM systems transmitting large number of modes over long distance.

Although current FM-EDFA has been demonstrated to be able to amplify 2 LP modes, several challenges still exist. i)How to improve the coupling efficiency of pump and signal beams which is low for current free space setup leading to low overall energy efficiency. ii) How to control the modal gain for large number of modes. One possible solution for the first challenge is to use mode selective coupler [61] or structured direction coupler [19] which were proposed

for mode multiplexer/de-multiplexer whose combining loss is much lower than beam splitter/dichroic mirror based free-space coupler. For pump/signal combining and coupling purpose, the coupler needs to be redesigned. All signal mode channels across C+L band can entirely pass while narrow band pump beam can be coupled to preferred mode in FM-EDF. The solution for the second challenge requires more sophisticated design of FM-EDFA. In [62], multimode pump control in conjugation with doping profile optimization is used to equalize 6 LP modes. However, the optimized doping profile is too complicated to be fabricated. In the future, all the degrees of freedom of FM-EDFA design (index profile, doping profile, mode contents of pump) must be explored and optimized to deliver a FM-EDFA which is energy efficient, can control gain over large number of modes and also easy to be fabricated.

In the aforementioned study on FMF, only linear properties such as mode coupling, modal loss and DMGD were extensively investigated. However, as in the case of transmission in single-mode fibers, nonlinear effects are important particularly in long-haul MDM system as nonlinear impairments set the fundamental capacity limit. Recently, the nonlinear transmission performance of MDM system has been investigated in [63, 64]. Nevertheless, in both simulation studies, either no mode coupling or constant mode coupling is considered in the numerical model. In practice, mode couplings are due to non-ideal fabrication and bends due to cabling process which randomly distributed along the FMF. Hence, the strength and location of mode coupling in FMF are random in nature. The random mode coupling results in power transfer and fluctuations over different modes. Since Kerr nonlinearity is intensity dependent, the power fluctuations further affect the nonlinear impairments on individual mode channels. In the future, the impact of random mode coupling on the nonlinear transmission performance needs to be investigated.

In single-mode fiber system, nonlinear impairment can be partially mitigated by using DSP [65, 66]. The corresponding approach for MDM system is important to be studied to further improve the performance of the transmission system in the future. It is well known that digital backward propagation (DBP) is an effective nonlinearity compensation method in single mode system. It requires full information of the link to invert the nonlinear Schrödinger equation (NLSE) in the digital domain. However, in multimode system, random, distributed and time varying mode couplings impact the whole fiber link. It is difficult to acquire full channel state information at every locations of the link. Additionally, inversion of full multimode nonlinear Schrödinger equation requires enormous computational complexity. Nevertheless, in strong coupled multimode system, full NLSE can be simplified to Monakov equations [67, 68] where the effect of local mode rotations is averaged across the link. A generalized multimode DBP thus can be implemented at a relative low computational complexity for the strong coupled MDM system.

The topics presented above are only several aspects regarding challenges associated with MDM transmission techniques. Although there is still a long way to go towards real implementation, mode-division multiplexed transmission has shown its great potential to be a promising technology for the next generation optical network.

REFERENCE

[1] D. J. Richardson, "Filling the Light Pipe," *Science*, vol. 330, pp. 327-328, 2010.

[2] J. P. Turkiewicz, A. M. J. Koonen, G. D. Khoe, and H. De Waardt, "Do we need 1310 nm transmission in modern networks?," in *Optical Communication (ECOC), European Conference and Exhibition on*, 2006, pp. 1-2.

[3] G. Li, "Recent advances in coherent optical communication," *Adv. Opt. Photon.*, vol. 1, pp. 279-307, 2009.

[4] Y. Han and G. Li, "Coherent optical communication using polarization multiple-input-multiple-output," *Opt. Express*, vol. 13, pp. 7527-7534, 09/19 2005.

[5] Q. Dayou, H. Ming-Fang, E. Ip, H. Yue-Kai, S. Yin, H. Junqiang, *et al.*, "101.7-Tb/s (370x294-Gb/s) PDM-128QAM-OFDM transmission over 3x55-km SSMF using pilot-based phase noise mitigation," in *Optical Fiber Communication Conference and Exposition (OFC/NFOEC), 2011 and the National Fiber Optic Engineers Conference*, 2011, p. PDPB5.

[6] H. T. Hattori and A. Safaai-Jazi, "Fiber Designs with Significantly Reduced Nonlinearity for Very Long Distance Transmission," *Appl. Opt.*, vol. 37, pp. 3190-3197, 1998.

[7] F. Yaman, N. Bai, Y. K. Huang, M. F. Huang, B. Zhu, T. Wang, *et al.*, "10 x 112Gb/s PDM-QPSK transmission over 5032 km in few-mode fibers," *Opt. Express*, vol. 18, pp. 21342-21349, 2010.

[8] F. Yaman, N. Bai, B. Zhu, T. Wang, and G. Li, "Long distance transmission in few-mode fibers," *Opt. Express*, vol. 18, pp. 13250-13257, 2010.

[9] G. J. Foschini, "Layered space-time architecture for wireless communication in a fading environment when using multi-element antennas," *Bell Labs Technical Journal*, vol. 1, pp. 41-59, 1996.

[10] J. Sakaguchi, Y. Awaji, N. Wada, A. Kanno, T. Kawanishi, T. Hayashi, *et al.*, "109-Tb/s (7x97x172-Gb/s SDM/WDM/PDM) QPSK transmission through 16.8-km homogeneous

multi-core fiber," in *Optical Fiber Communication Conference/National Fiber Optic Engineers Conference*, 2011, p. PDPB6.

[11] B. Zhu, T. Taunay, M. Fishteyn, X. Liu, S. Chandrasekhar, M. Yan, *et al.*, "Space-, Wavelength-, Polarization-Division Multiplexed Transmission of 56-Tb/s over a 76.8-km Seven-Core Fiber," in *Optical Fiber Communication Conference/National Fiber Optic Engineers Conference*, 2011, p. PDPB7.

[12] R. Ryf, S. Randel, A. H. Gnauck, C. Bolle, A. Sierra, S. Mumtaz, *et al.*, "Mode-Division Multiplexing Over 96 km of Few-Mode Fiber Using Coherent 6x6 MIMO Processing," *Lightwave Technology, Journal of*, vol. 30, pp. 521-531, 2012.

[13] X. Cen, R. Amezcua-Correa, B. Neng, E. Antonio-Lopez, D. M. Arrioja, A. Schulzgen, *et al.*, "Hole-Assisted Few-Mode Multicore Fiber for High-Density Space-Division Multiplexing," *Photonics Technology Letters, IEEE*, vol. 24, pp. 1914-1917, 2012.

[14] D. Gloge, "Weakly Guiding Fibers," *Appl. Opt.*, vol. 10, pp. 2252-2258, 1971.

[15] L. Ming-Jun, B. Hoover, L. Shenping, S. Bickham, S. Ten, E. Ip, *et al.*, "Low delay and large effective area few-mode fibers for mode-division multiplexing," in *Opto-Electronics and Communications Conference (OECC)*, 2012, pp. 495-496.

[16] R. Ryf, S. Randel, A. H. Gnauck, C. Bolle, R.-J. Essiambre, P. Winzer, *et al.*, "Space-division multiplexing over 10 km of three-mode fiber using coherent 6 × 6 MIMO processing," in *Optical Fiber Communication Conference/National Fiber Optic Engineers Conference*, 2011, p. PDPB10.

[17] C. Koebele, M. Salsi, D. Sperti, P. Tran, P. Brindel, H. Mardoyan, *et al.*, "Two mode transmission at 2x100Gb/s, over 40km-long prototype few-mode fiber, using LCOS-based programmable mode multiplexer and demultiplexer," *Opt. Express*, vol. 19, pp. 16593-16600, 2011.

[18] A. Li, A. Al Amin, X. Chen, and W. Shieh, "Reception of Mode and Polarization Multiplexed 107-Gb/s CO-OFDM Signal over a Two-Mode Fiber," in *Optical Fiber Communication Conference/National Fiber Optic Engineers Conference*, 2011, p. PDPB8.

[19] B. Huang, C. Xia, G. Matz, N. Bai, and G. Li, "Structured Directional Coupler Pair for Multiplexing of Degenerate Modes," in *Optical Fiber Communication Conference/National Fiber Optic Engineers Conference*, 2013, p. JW2A.25.

[20] R. Ryf, M. A. Mestre, A. Gnauck, S. Randel, C. Schmidt, R. Essiambre, *et al.*, "Low-Loss Mode Coupler for Mode-Multiplexed transmission in Few-Mode Fiber," in *Optical Fiber Communication Conference/National Fiber Optic Engineers Conference*, 2012, p. PDP5B.5.

[21] N. K. Fontaine, R. Ryf, S. G. Leon-Saval, and J. Bland-Hawthorn, "Evaluation of Photonic Lanterns for Lossless Mode-Multiplexing," in *Optical Communication (ECOC), European Conference and Exhibition on*, 2012, p. Th.2.D.6.

[22] N. Bai, E. Ip, M.-j. Li, T. Wang, and G. Li, "Experimental demonstration of adaptive frequency-domain equalization for mode-division multiplexed transmission," in *Optical Fiber Communication Conference/National Fiber Optic Engineers Conference 2013*, 2013, p. OM2C.5.

[23] N. Bai, E. Ip, M.-j. Li, T. Wang, and G. Li, "Long-Distance Mode-Division Multiplexed Transmission using Normalized Adaptive Frequency Domain Equalization," presented at the Photonics Society Summer Topical Meeting Series, 2013 IEEE Hawaii, USA, 2013.

[24] N. Bai, C. Xia, and G. Li, "Adaptive frequency-domain equalization for the transmission of the fundamental mode in a few-mode fiber," *Opt. Express*, vol. 20, pp. 24010-24017, 2012.

[25] J. M. K. Keang-Po Ho, "Mode Coupling and its Impact on Spatially Multiplexed Systems," in *Optical Fiber Telecommunications Volume VIB: Systems and Networks*, T. L. Ivan Kaminow, Alan Willner, Ed., ed: Elsevier Science, 2013, pp. 491-568.

[26] S. Randel, R. Ryf, A. Sierra, P. J. Winzer, A. H. Gnauck, C. A. Bolle, *et al.*, "6×56-Gb/s mode-division multiplexed transmission over 33-km few-mode fiber enabled by 6×6 MIMO equalization," *Opt. Express*, vol. 19, pp. 16697-16707, 2011.

[27] A. Viterbi, "Nonlinear estimation of PSK-modulated carrier phase with application to burst digital transmission," *Information Theory, IEEE Transactions on*, vol. 29, pp. 543-551, 1983.

[28] S. Zhang, P. Y. Kam, J. Chen, and C. Yu, "Decision-aided maximum likelihood detection in coherent optical phase-shift-keying system," *Opt. Express*, vol. 17, pp. 703-715, 01/19 2009.

[29] M. Kuschnerov, M. Chouayakh, K. Piyawanno, B. Spinnler, E. De Man, P. Kainzmaier, *et al.*, "Data-Aided Versus Blind Single-Carrier Coherent Receivers," *Photonics Journal, IEEE*, vol. 2, pp. 387-403, 2010.

[30] N. Bai and G. Li, "Adaptive Frequency-Domain Equalization for Mode-Division Multiplexed Transmission," *Photonics Technology Letters, IEEE*, vol. 24, pp. 1918-1921, 2012.

[31] M. S. Faruk and K. Kikuchi, "Adaptive frequency-domain equalization in digital coherent optical receivers," *Opt. Express*, vol. 19, pp. 12789-12798, 06/20 2011.

[32] S. Haykin, *Adaptive Filter Theory* 4ed.: Prentice Hall, 2001.

[33] F. Yaman, E. Mateo, and T. Wang, "Impact of Modal Crosstalk and Multi-Path Interference on Few-Mode Fiber Transmission," in *Optical Fiber Communication Conference/National Fiber Optic Engineers Conference*, 2012, p. OTu1D.2.

[34] C. Koebele, M. Salsi, L. Milord, R. Ryf, C. A. Bolle, P. Sillard, *et al.*, "40km Transmission of Five Mode Division Multiplexed Data Streams at 100Gb/s with low MIMO-DSP Complexity," in *Optical Communication (ECOC), European Conference and Exhibition on*, 2011, p. Th.13.C.3.

[35] X. Chen, J. He, A. Li, J. Ye, and W. Shieh, "Characterization of Dynamic Evolution of Channel Matrix in Two-mode Fibers," in *Optical Fiber Communication Conference/National Fiber Optic Engineers Conference 2013*, 2013, p. OM2C.3.

[36] N. Bai, E. Ip, Y.-K. Huang, E. Mateo, F. Yaman, M.-J. Li, *et al.*, "Mode-division multiplexed transmission with inline few-mode fiber amplifier," *Opt. Express*, vol. 20, pp. 2668-2680, 2012.

[37] M. D. Feuer, L. E. Nelson, X. Zhou, S. L. Woodward, R. Isaac, B. Zhu, *et al.*, "Demonstration of joint DSP receivers for spatial superchannels," in *Photonics Society Summer Topical Meeting Series, IEEE*, 2012, pp. 183-184.

[38] E. Ip, M.-J. Li, K. Bennett, S. Bickham, Y.-K. Huang, A. Tanaka, *et al.*, "Few-mode fiber transmission with in-line few-mode erbium-doped fiber amplifier," in *Proc. SPIE 8647, Next-Generation Optical Communication: Components, Sub-Systems, and Systems II*, 2013, p. 864709.

[39] E. Ip, N. Bai, Y.-K. Huang, E. Mateo, F. Yaman, S. Bickham, *et al.*, "88x3x112-Gb/s WDM Transmission over 50-km of Three-Mode Fiber with Inline Multimode Fiber Amplifier," in *37th European Conference and Exposition on Optical Communications*, 2011, p. Th.13.C.2.

[40] X. He, X. Zhou, J. Wang, Y. Weng, and Z. Pan, "A Fast Convergence Frequency Domain Least Mean Square Algorithm for Compensation of Differential Mode Group Delay in Few Mode Fibers," in *Optical Fiber Communication Conference/National Fiber Optic Engineers Conference 2013*, 2013, p. OM2C.4.

[41] N. Bai and L. Guifang, "Adaptive frequency domain equalization for mode-division multiplexed transmission," in *Photonics Society Summer Topical Meeting Series, IEEE*, 2012, pp. 185-186.

[42] F. Ferreira, D. Fonseca, A. Lobato, B. Inan, and H. Silva, "Reach Improvement of Mode Division Multiplexed Systems Using Fiber Splices," *Photonics Technology Letters, IEEE*, vol. 25, pp. 1091-1094, 2013.

[43] J. D. Downie, J. E. Hurley, D. V. Kuksenkov, C. M. Lynn, A. E. Korolev, and V. N. Nazarov, "Transmission of 112 Gb/s PM-QPSK signals over up to 635 km of multimode optical fiber," *Opt. Express*, vol. 19, pp. B363-B369, 12/12 2011.

[44] H. Keang-Po and J. M. Kahn, "Statistics of Group Delays in Multimode Fiber With Strong Mode Coupling," *Lightwave Technology, Journal of*, vol. 29, pp. 3119-3128, 2011.

[45] T. Mori, T. Sakamoto, M. Wada, T. Yamamoto, and F. Yamamoto, "Low DMD Four LP Mode Transmission Fiber for Wide-band WDM-MIMO System," in *Optical Fiber Communication Conference/National Fiber Optic Engineers Conference 2013*, 2013, p. OTh3K.1.

[46] T. Sakamoto, T. Mori, T. Yamamoto, N. Hanzawa, S. Tomita, F. Yamamoto, *et al.*, "Mode-Division Multiplexing Transmission System With DMD-Independent Low

Complexity MIMO Processing," *Lightwave Technology, Journal of,* vol. 31, pp. 2192-2199, 2013.

[47] R. Ryf, M. A. Mestre, S. Randel, C. Schmidt, A. H. Gnauck, R. Essiambre, *et al.*, "Mode-Multiplexed Transmission Over a 209-km DGD-Compensated Hybrid Few-Mode Fiber Span," *Photonics Technology Letters, IEEE,* vol. 24, pp. 1965-1968, 2012.

[48] C. Antonelli, A. Mecozzi, M. Shtaif, and P. J. Winzer, "Random coupling between groups of degenerate fiber modes in mode multiplexed transmission," *Opt. Express,* vol. 21, pp. 9484-9490, 2013.

[49] F. Ferreira, D. Fonseca, and H. Silva, "Design of Few-Mode Fibers With Arbitrary and Flattened Differential Mode Delay," *Photonics Technology Letters, IEEE,* vol. 25, pp. 438-441, 2013.

[50] P. Krummrich and K. Petermann, "Evaluation of Potential Optical Amplifier Concepts for Coherent Mode Multiplexing," in *Optical Fiber Communication Conference/National Fiber Optic Engineers Conference*, 2011, p. OMH5.

[51] E. Desurvire, *Erbium-doped Fiber Amplifiers-Principles and Applications*: Wiley-Interscience, 1994.

[52] C. Stacey and J. Jenkins, "Demonstration of fundamental mode propagation in highly multimode fibre for high power EDFAs," in *Lasers and Electro-Optics Europe, 2005. CLEO/Europe. 2005 Conference on*, 2005, pp. 558-558.

[53] A. Galvanauskas, "Mode-scalable fiber-based chirped pulse amplification systems," *Selected Topics in Quantum Electronics, IEEE Journal of,* vol. 7, pp. 504-517, 2001.

[54] M. Gong, Y. Yuan, C. Li, P. Yan, H. Zhang, and S. Liao, "Numerical modeling of transverse mode competition in strongly pumped multimode fiber lasers and amplifiers," *Opt. Express,* vol. 15, pp. 3236-3246, 2007.

[55] C. D. Poole and S. C. Wang, "Bend-induced loss for the higher-order spatial mode in a dual-mode fiber," *Opt. Lett.,* vol. 18, pp. 1712-1714, 1993.

[56] D. Marcuse, "Curvature loss formula for optical fibers," *J. Opt. Soc. Am.*, vol. 66, pp. 216-220, 1976.

[57] N. Bai, E. Ip, Y. Luo, G.-D. Peng, T. Wang, and G. Li, "Experimental Study on Multimode Fiber Amplifier Using Modal Reconfigurable Pump," in *Optical Fiber Communication Conference*, 2012, p. OW1D.3.

[58] J. Linares, C. Montero, V. Moreno, M. C. Nistal, X. Prieto, J. R. Salgueiro, *et al.*, "Glass processing by ion exchange to fabricate integrated optical planar components: applications," in *Proc. SPIE 3936, Integrated Optics Devices IV*, 2000, pp. 227-238.

[59] J. R. Salgueiro, V. Moreno, and J. Liñares, "Model of Linewidth for Laser Writing on a Photoresist," *Appl. Opt.*, vol. 41, pp. 895-901, 2002.

[60] N. Bai, E. Ip, T. Wang, and G. Li, "Multimode fiber amplifier with tunable modal gain using a reconfigurable multimode pump," *Opt. Express*, vol. 19, pp. 16601-16611, 2011.

[61] J. D. Love and N. Riesen, "Mode-selective couplers for few-mode optical fiber networks," *Opt. Lett.*, vol. 37, pp. 3990-3992, 2012.

[62] E. Ip, "Gain Equalization for Few-Mode Fiber Amplifiers Beyond Two Propagating Mode Groups," *Photonics Technology Letters, IEEE*, vol. 24, pp. 1933-1936, 2012.

[63] C. Koebele, M. Salsi, G. Charlet, and S. Bigo, "Nonlinear effects in long-haul transmission over bimodal optical fibre," in *Optical Communication (ECOC), 2010 36th European Conference and Exhibition on*, 2010, pp. 1-3.

[64] A. Li, J. Ye, X. Chen, and W. Shieh, "Impact of Linear Mode Coupling on the Nonlinear Transmission Performance of Few-mode Fibers," in *Asia Communications and Photonics Conference*, 2012, p. AS2C.4.

[65] X. Li, X. Chen, G. Goldfarb, E. Mateo, I. Kim, F. Yaman, *et al.*, "Electronic post-compensation of WDM transmission impairments using coherent detection and digital signal processing," *Opt. Express*, vol. 16, pp. 880-888, 2008.

[66] E. Ip and J. M. Kahn, "Compensation of Dispersion and Nonlinear Impairments Using Digital Backpropagation," *Lightwave Technology, Journal of,* vol. 26, pp. 3416-3425, 2008.

[67] A. Mecozzi, C. Antonelli, and M. Shtaif, "Nonlinear propagation in multi-mode fibers in the strong coupling regime," *Opt. Express,* vol. 20, pp. 11673-11678, 2012.

[68] S. Mumtaz, R.-J. Essiambre, and G. P. Agrawal, "Nonlinear Propagation in Multimode and Multicore Fibers: Generalization of the Manakov Equations," *J. Lightwave Technol.,* vol. 31, pp. 398-406, 2013.